



**UNIVERSITÀ DEGLI STUDI DI CATANIA**  
DIPARTIMENTO DI INGEGNERIA ELETTRICA, ELETTRONICA E INFORMATICA  
CORSO DI DOTTORATO IN INGEGNERIA DEI SISTEMI, ENERGETICA,  
INFORMATICA E DELLE TELECOMUNICAZIONI

**INNOVATIVE CHARACTERIZATION AND  
ELASTOPLASTIC MODELLING OF METALS  
UNDER STATIC AND DYNAMIC CONDITIONS**

Raffaele Barbagallo

Supervisor: Prof. Giuseppe Mirone

Coordinator of Ph.D Program: Prof. Paolo Arena

XXX CICLO – 2014/2017

# Abstract

Material characterization and modelling are fundamental in both Industry and Research worlds in order to have reliable FEM simulations. In this research, such procedures are investigated regarding quasistatic and dynamic tests on metals. According to several experiments reported in the literature, the static elastoplastic behaviour of such materials depends not only on the first stress invariant (triaxiality) for the ductile damage and on the second stress invariant (equivalent von Mises stress) for the yield, but also on the third stress invariant (normalized Lode angle  $X$ ) which may affect at the same time the yielding and the ductile failure. In this research, a new accurate and easy-to-calibrate yield model is presented, in which the yield surface depends on the Lode Angle and, eventually, also on the triaxiality ratio. The proposed model has been tested and validated against experimental data from the literature on the Titanium alloy Ti6Al4V. Moreover, in this research, a new methodology is proposed and experimentally validated for translating the engineering curves, coming from tensile tests, into the true curves via material-independent mathematical tools named MVB functions, which only depend on the necking initiation strain and on the aspect ratio of the undeformed cross section. Regarding the dynamic behaviour of metals, this research is aimed at the quantitative evaluation of the error levels in the characterization via Hopkinson bar tensile tests, ran according to the classical strain-gauge-based experimental procedure and to the enhanced high-speed-camera-assisted procedure. In addition, the effect of the specimen slenderness is investigated for checking the sensitivity of both the above techniques to different specimen geometries. Lastly, this work analyses the necking-induced freezing of the strain rate effect via experimental data and numerical simulations, with reference to materials exhibiting both early and late necking initiation and the consequences of this phenomenon in the characterization process via Hopkinson bar tensile tests.



# Sommario

La caratterizzazione e la modellazione dei materiali sono fondamentali per avere simulazioni agli elementi finiti attendibili, sia in campo industriale che nella ricerca. Nella presente tesi, tali procedure sono indagate nell'ottica dei test sperimentali quasistatici e dinamici sui materiali metallici. Secondo molteplici dati sperimentali presenti in letteratura, il comportamento quasistatico elastoplastico di tali materiali dipende non solamente dal primo invariante dello stress (triassialità) per il danno duttile e dal secondo invariante dello stress (tensione equivalente di von Mises) per lo snervamento, ma anche dal terzo invariante dello stress (espresso dall'angolo di Lode normalizzato  $X$ ) che può influenzare allo stesso tempo lo snervamento e la frattura duttile. Nella presente ricerca, viene presentato un nuovo modello di snervamento accurato e facile da calibrare, nel quale la relativa superficie dipende dall'angolo di Lode ed, eventualmente, anche dalla triassialità. Il modello proposto è stato testato e validato con dati sperimentali da letteratura sulla lega di titanio Ti6Al4V. In questa ricerca, si propone e si valida inoltre una nuova metodologia per trasformare curve ingegneristiche, ottenute tramite test di trazione, in curve true, attraverso degli strumenti matematici indipendenti dal materiale denominati MVB, funzioni solamente della deformazione di innesco necking e della geometria della sezione resistente indeformata del provino. Nel campo del comportamento dinamico dei materiali metallici, la presente tesi ha come obiettivo la valutazione quantitativa degli errori commessi nella caratterizzazione attraverso barra di Hopkinson, utilizzando il classico approccio basato solamente sulla lettura dei segnali degli strain gauge ed il più accurato approccio basato sull'utilizzo di camera rapida. In tale valutazione, si è considerato anche l'effetto della snellezza del provino e come tale caratteristica influisca sui risultati dell'una e dell'altra metodologia. Infine, nel presente lavoro, è stato analizzato il fenomeno del congelamento dell'effetto dello strain rate indotto dall'insorgere della strizione, attraverso prove sperimentali e simulazioni numeriche, considerando materiali caratterizzati da insorgenza precoce o tardiva del necking, e le conseguenze che tale fenomeno induce sulla caratterizzazione attraverso prove di trazione con barra di Hopkinson.



# Acknowledgements

There were ups and downs, but I will certainly remember these doctoral years as a happy period of my life in which I learned a lot, I met and worked with wonderful people and my life and myself have undergone great changes.

First of all, I would like to thank Prof. Oliveri and his research team, in particular Gaetano Sequenzia and Gabriele Fatuzzo, for accompanying and guiding me throughout the graduation course and for introducing me to the much criticized and complicated world of research. You have always treated me as a part of your group, your family, and I will be grateful forever for that. It is your fault if I am here to write these acknowledgements!

Likewise, the greatest thank-you goes to my supervisor, Prof. Mirone, who afterwards took the intellectual lead of my growth in the research world and has guided me during these three years of work. I learned a lot from him and I have come to appreciate his preparation, dedication to work, kindness, respect and availability to anyone, despite the endless commitments. Working together has been a great pleasure and I hope we will continue for a very long time. With him, I have to thank also Domenico Corallo for his precious guide, especially at the beginning of my doctoral journey. The researcher who I am today, with strengths and weaknesses, is the son of your teachings.

The mobility period that I spent in Ghent was fundamental for my intellectual and personal growth. My supervisor there was Prof. Verleysen, a wonderful person and researcher who immediately made me feel at home and with whom a strong mutual esteem was born and still continues today. Many thanks for allowing me to live this priceless experience and to improve myself as a man and as a Researcher.

Thanks also to Giancarlo Costa (Signor Costa for everyone), for his incredible availability and dedication, and to all researchers and university technicians with whom I had the pleasure to work or just have a snack at the bar. The university has become my second home thanks to you.

Turning to the people closer to my heart, I have to thank Ciccio, Giulio and Matteo who are not just friends but the family I chose. They have made these years precious, always proving to be true safe harbours when everything else was uncertain.

Not all relationships are meant to last forever, but this does not mean they cannot leave an important mark. A big thank-you goes to Lella, who was next to me well before the beginning of this doctorate and who supported me in facing this challenge.

As well as making me grow intellectually, research has done something a lot more important: it has given me my beloved Federica. Thank you for what you are, for

what we are and for what you have done for me, supporting me and making me always feel up to the challenges to be faced. Thank you Ing.

Last but not the least, it could seem obvious to thank my family but much less obvious is the luck I had in having a family like mine: my father, who gave me his scientific thought and who in devotion to the sons is second to none; my mother, always present and attentive but never cumbersome; my brother, who, even from far away, has managed to never be distant; my sister, simply the most sensitive person in the world. Thanks for everything.

# Contents

1	Introduction .....	1
1.1	Motivation.....	1
1.2	Static Characterization Literature Review .....	3
1.3	Dynamic Characterization Literature Review .....	6
1.4	Objective of the Study and Thesis Overview .....	8
2	Static Characterization and Modelling of Metals .....	11
2.1	Overview.....	11
2.2	Yielding, Anisotropy and Lode Angle Dependence.....	12
2.2.1	Static Response of Titanium Alloy Produced by Electron Beam Melting	12
2.2.2	New Yield Model .....	19
2.3	Novel Experimental Characterization Method .....	30
2.3.1	Engineering Curve vs True Curve Vs Flow Curve .....	30
2.3.2	Relationship between True Curve and Macroscopic Experimental Data: the MVB Functions.....	32
2.3.3	Application to Experimental Data.....	42
2.4	Static Characterization and Modelling Summary.....	49
3	Dynamic Characterization and Modelling of Metals .....	53
3.1	Overview.....	53
3.2	Experimental Issues in Tensile Hopkinson Bar Testing.....	53
3.2.1	Specimen Geometry, Necking and Engineering vs. True Curves Approximations .....	53
3.2.2	Specimen Shape Effect and Engineering vs. True Approach in SHTB Experiments.....	58
3.3	Necking-Induced Freezing of the strain rate effect .....	69
3.3.1	Dynamic Response of Titanium Alloy Produced by Electron Beam Melting	69
3.3.2	FE370 Steel: Dynamic Stress Amplification and Modelling of the Strain Rate Effect .....	74



3.3.3	Testability Limits Due to the Freezing Effect.....	89
3.4	Dynamic Characterization and Modelling Summary.....	92
4	Conclusions.....	95
	References.....	97

# List of Figures

Figure 1.1 Simulation of a sheet forming process .....	1
Figure 1.2 Simulation of an airplane component .....	2
Figure 1.3 Simulation of a Car Crash Test .....	3
Figure 2.1 Specimen geometry .....	13
Figure 2.2 Static tensile test.....	14
Figure 2.3 Fast camera image of a dynamic tensile test.....	14
Figure 2.4 Static Tensile tests, Force-Displacement results.....	15
Figure 2.5 Static Tensile tests, corrected Force-Displacement results.....	15
Figure 2.6 Torsion tests, Moment-Rotation results .....	16
Figure 2.7 Torsion tests, corrected Moment-Rotation results .....	16
Figure 2.8 Constitutive torsion curves, Nadai EXP vs Nadai FIT EXP.....	17
Figure 2.9 True curves, Static Tensile vs Static Torsion.....	17
Figure 2.10 True tensile curves – Comparison with literature data. *Obtained from engineering curves until neck + linear extension .....	19
Figure 2.11 Cylindrical, stress invariants-based coordinates .....	20
Figure 2.12 Yield surface edge definition .....	21
Figure 2.13 Four different Yield surfaces corresponding to a given uniaxial stress and two couples of shear stress / quadratic amplification. ....	23
Figure 2.14 Specimens shapes and load modes.....	24
Figure 2.15 Material hardening functions in tension and torsion.....	25
Figure 2.16 The m function for the considered material .....	25
Figure 2.17 Deformed meshes of tension-torsion and flat shear specimens .....	26
Figure 2.18 Evolving yield surface of the Ti-6Al-4V alloy at different strain levels .....	26
Figure 2.19 Finite elements modelling of experiments by quadratic yield and by von Mises yield.....	27
Figure 2.20 Stress histories of A20 and A40 tests at critical material points (mid-thickness and outer surface at the neck section).....	29
Figure 2.21 Material flow curves .....	36
Figure 2.22 Post-necking area reduction VS engineering strain referred to the necking for round (left) and rectangular t = 20 (right) specimens .....	38
Figure 2.23 Post-necking true strain VS post-necking engineering strain for round (left) and rectangular t = 20 (right) specimens .....	39
Figure 2.24 Modified post-necking true strain VS post-necking engineering strain for round (top left), square (top right), rectangular t = 2 (middle left), rectangular t = 2.65 (middle right), rectangular t = 5 (bottom left) and rectangular t = 20 (bottom right) specimens.....	40
Figure 2.25 Specimen gage lengths evolution during a test.....	41
Figure 2.26 Alloy 185 specimen geometry .....	43

Figure 2.27 Scheme of the global/intermediate/local DIC acquisition scales .....	43
Figure 2.28 Experimental data for specimens of Al alloy with $t=20$ .....	44
Figure 2.29 Comparison between the true curves by DIC, MVB and FEM (left); comparison between the engineering curves by experiments and by FEM (right): material modelled via experimental engineering curve processed by the MVB and by the MLR correction. ....	45
Figure 2.30 Scheme of the Joun specimen.....	46
Figure 2.31 True and flow curves obtained with MVB and MLR.....	46
Figure 2.32 Comparison between the experimental, simulation MVB+MLR and simulation Flow Line engineering curves .....	47
Figure 2.33 True and flow curves obtained with MVB and MLR.....	48
Figure 2.34 Comparison between the experimental, simulation MVB+MLR Interrupted, simulation MVB+MLR Complete and simulation Flow Line engineering curves .....	49
Figure 3.1 Effect of shoulders elongation on two different gage lengths subjected to the same $\epsilon_{eng}$ .....	54
Figure 3.2 Effect of the same post-necking strain on two different gage lengths. ....	55
Figure 3.3 : Specimens shape for multi-length, conventional SHTB tests .....	58
Figure 3.4: SHTB setup.....	60
Figure 3.5: Equilibrium check for slower long specimens (left) and faster short specimens (right) dynamic tests .....	60
Figure 3.6: Engineering stress-strain and strain rate-time curves for AL 2011 ....	62
Figure 3.7: Neck-affected zone in short and long specimens .....	63
Figure 3.8: Check of engineering strains from reflected wave and from camera elongation readings .....	64
Figure 3.9: Engineering curves of FEN specimens with different L/d tested at similar strain rates .....	65
Figure 3.10: Engineering curves of FEN specimens with identical L/d = 2.5, tested at different strain rates.....	65
Figure 3.11: Necking and failure location of longer specimens .....	66
Figure 3.12: Frame extracted from the high-speed camera acquisition for diameter and elongation measurements .....	66
Figure 3.13: True curves and true strain rate data from FEN experiments.....	67
Figure 3.14 True Curves, Static Tensile vs Dynamic Tensile.....	69
Figure 3.15 Static Tensile true curve calibration .....	70
Figure 3.16 True curve vs Equivalent curve vs FEM true curve .....	71
Figure 3.17 Tensile Test axisymmetric FE model .....	71
Figure 3.18 Static tensile tests – Exp vs FEM .....	71
Figure 3.19 Dynamic true EXP vs Dynamic true fitting vs Static true fitting.....	72
Figure 3.20 $R_{true}$ and R vs true strain rate .....	72
Figure 3.21 Dynamic true curves – EXP vs FIT EXP vs FEM.....	73

Figure 3.22 True curves – Comparison with literature data. *Obtained from engineering curves, therefore after necking they are not reliable due to non-uniform strain .....	74
Figure 3.23 Engineering and true Strain rates vs. strains from experiments.....	75
Figure 3.24 Static and dynamics true curves.....	77
Figure 3.25 Dynamic amplification from the extreme experimental tests 08 (Fast) e 12(Slow) .....	80
Figure 3.26 Static true stress and equivalent stress by MLR correction (left), Ludwik and MLR flow curves (right) .....	81
Figure 3.27 Validation of the static hardening: static true stress from experiments and from FEM .....	82
Figure 3.28: Tentative functions for modelling the strain rate effect.....	84
Figure 3.29 Deformed FEM specimen with bar interfaces .....	85
Figure 3.30 Comparison of Exp. vs. FEM true curves (left), Mises stress from FEM (right).....	86
Figure 3.31 Comparison of Exp. vs. FEM true strain rates.....	87
Figure 3.32 Evolving flow stress/true stress ratio during SHTB tests .....	89
Figure 3.33 Limit strain rate as function of $tR$ and $\epsilon_N$ .....	91

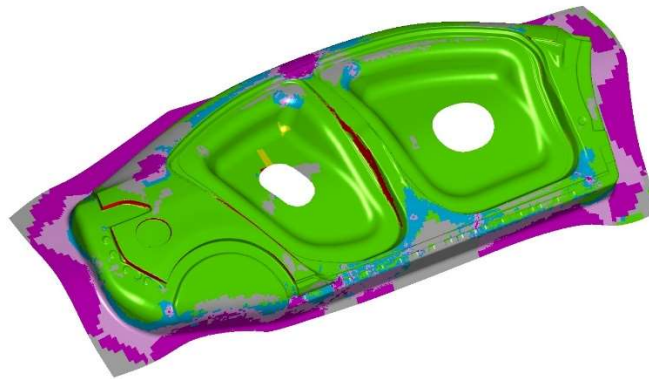
# List of Tables

Table 2.1 Chemical composition of the powder used for the Ti6Al4V alloy .....	13
Table 2.2 Experimental tests by Allahverdizadeh et al.....	23
Table 2.3 Material hardening functions in tension and torsion.....	24
Table 2.4 Specimens FEM Models .....	35
Table 2.5 Materials characteristics.....	36
Table 3.1 Specimens data for SHTB tests.....	59
Table 3.2 EBM Ti6Al4V parameters .....	69
Table 3.3 FEN370 Test grid combining different Bar preloads, specimen lengths and nominal strain rates .....	75

# 1 Introduction

## 1.1 Motivation

This thesis fits into the framework of the static and dynamic characterization of metals. The static characterization is of great importance for the design of a component in both elastic and plastic fields. Modern materials are very ductile so they can be subjected to large deformations before failure. In contrast to the past, mechanical design in the plastic field, knowing accurately the plastic behaviour of the material, is getting more and more importance in all the high end applications in which it is necessary to reduce weight, size and costs and, at the same time, ensure high levels of structural safety. The safety factors can be seen as ignorance factors; knowing better the material behaviour, it is possible to diminish such safety/ignorance factors and reduce the consequent overdimensioning. In practice, if it is possible to know the maximum load to which a structure could be exceptionally subjected and if it is known the behaviour of the material from its yield to fracture, it is possible and useful, for the reasons explained before, to design the structure in order to have that it will deform, in such extreme case, until a stress-strain state not so far from a critical one. Very often in fact, it is more expensive to overdimension a structure than properly dimension it and then to substitute part or all of it when it is known that it is close to fracture. In some applications in which the weight is fundamental, for example in aeronautics, it is mandatory to use low safety factors to guarantee a certain level of performance. Therefore, in some cases the weight reduction consequent to the material plastic behaviour knowledge is useful for an economic reason, in others for purely technical reasons.



*Figure 1.1 Simulation of a sheet forming process*

Another aspect is related to applications, for example in the automotive industry, in which some components are designed to behave like energy absorber and, therefore, their role is totally depending on the plastic phase of the material. Moreover, the large plastic deformations of modern materials are very helpful in the manufacturing design of many components involving, for example, forming processes (Figure 1.1). All these applications and processes are simulated by means of FEM analysis but, without a correct representation of the material plastic behaviour and failure, this tool is inefficient. The work that will be shown in Chapter 2 aims at the development of a new yield model and a new experimental procedure, useful to improve the static characterization and modelling of metals.

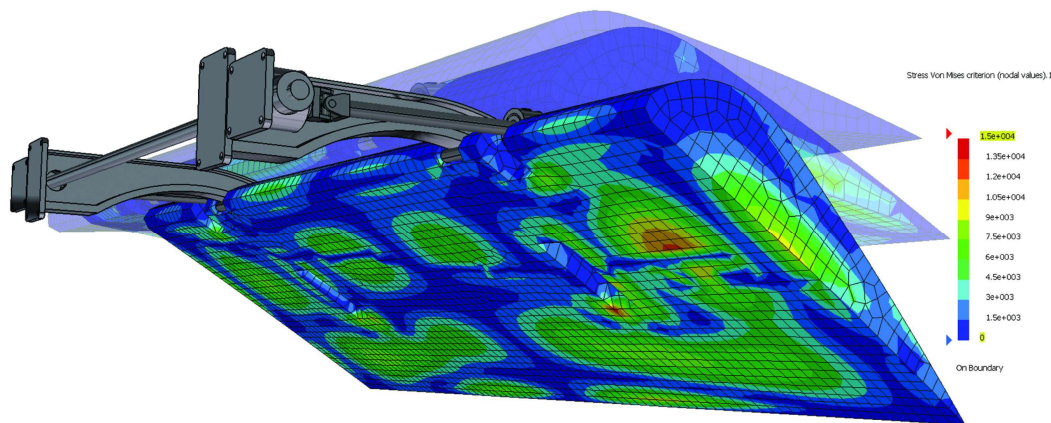


Figure 1.2 Simulation of an airplane component

On the other hand, considering the dynamic behaviour of metals, the strain rate has a great influence on their critical properties such as elastic modulus, yield stress, failure stress, and failure strain. There are many applications where materials are expected to perform under high strain rate conditions. Talking about aerospace industry, spacecraft and other orbital bodies are exposed to foreign debris that may be traveling at high relative velocities (Figure 1.2). Moreover, jet engines have extremely high operating speeds so they can be hit by foreign object with very high shock loads. Containment of debris in the event of catastrophic engine failure is another issue in jet engine design that involves highly transient loading. In some cases, fragments could pierce the engine casing and severely damaged hydraulic components that are vital for aircraft control. Automotive industry is another example, in particular considering crash test behaviour of the cars (Figure 1.3); in fact, many parts of the vehicle are designed to behave like energy absorbers during an impact, causing smaller accelerations to the bodies of the driver and of the occupants. Further examples are defence applications, turbine blade design and

ballistic devices. To simulate and design components involved in all these applications and in many others, it is fundamental to know the high strain rate behaviour of the material and the work that will be shown in Chapter 3 aims precisely at the improvement of the knowledge about the dynamic characterization and modelling of metals by means of Split Hopkinson Tensile Bar tests.

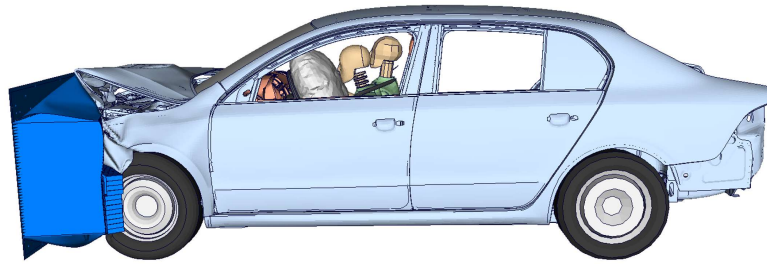


Figure 1.3 Simulation of a Car Crash Test

## 1.2 Static Characterization Literature Review

For completely describing the local stress state at single material points of a loaded structure, three parameters are necessary, namely, the principal stresses or the invariants of the stress tensor. In the classical plasticity framework, the second deviatoric stress invariant is assumed to be sufficient for describing the elastoplastic response of structural materials via the von Mises criteria and the hardening functions. The first expresses the yield condition through a yield surface in the stress space, the second regards the evolving size of such a surface to the equivalent plastic strain. Frequently, the response of structural metals does not comply with such idealization because also the stress triaxiality  $TF$  (first stress invariant normalized to the Mises stress) and the normalized Lode angle  $X$  (based on the third stress invariant normalized by the Mises stress) play a significant role on the elastoplastic response and on the ductile fracture. Since the sixties of the past century, the stress triaxiality is known to accelerate the failure of ductile materials by decreasing their failure strain (Chaboche, 1988; Lemaitre, 1985; Mackenzie et al., 1988; McClintock, 1968; Rice and Tracey, 1969; Gurson, 1977; Tvergaard and Needleman, 1984; Barsoum and Faleskog, 2007; Mashayekhi and Ziaei-Rad, 2006; Bai and Wierzbicki, 2010; Xue and Wierzbicki, 2009). This aspect is completely ascertained and many models are available in the literature (Bao and Wierzbicki, 2004; Brunig et al., 2008; Wierzbicki et al., 2005), although no triaxiality-related failure criteria is still universally accepted. Similar considerations apply to the third invariant expressed by normalized Lode angle, whose role in the embrittlement of materials is gaining stronger evidence in the recent years (Xue, 2009; Xue et al.,



2010; Mae et al., 2007; Ghajar et al., 2013; Mirone & Corallo, 2010a; Graham et al., 2012; Barsoum et al., 2012; Faleskog et al., 2013; Xue et al., 2013; Papisidero et al., 2014; Rodríguez-Millán, 2015; Cortese et al., 2014) but is not yet fully recognized. In addition, also the elastoplastic response of structural materials is potentially affected by the triaxiality factor  $TF$  and by the deviatoric parameter  $X$ . The triaxiality is known to directly influence the plastic yield of granular materials, ceramics etc., but at the same time, it seems to have a negligible effect on the plasticity of most metals (Bigoni and Piccolroaz, 2004; Piccolroaz and Bigoni, 2009; Penasa et al., 2014; Lehmann, 1985), suggesting that their yield surface in the stress space has constant cross section along the trisector axis. Conversely, the deviatoric parameter  $X$  is found to play a key role on the yield of many metals. In such cases, the flow curves from tension may significantly differ from those obtained by torsion (Bai and Wierzbicki, 2008; Erice and Gálvez, 2014; Gao et al., 2009; Gao et al., 2011; Dorogoy et al., 2015; Cortese et al., 2015; Mirone, 2014), although it is not a generalized occurrence, and the stress-strain plastic response of other metals is almost unaffected by  $X$ . Then, the yield surface of metals may either have a circular Mises-like cross section or a six-lobed Lode-angle dependent cross section, with identical shape repeated every 120 degrees. In case of anisotropic metals with  $X$ -dependent yield, the six-lobed dependence of the yield stress on the Lode angle is not repeated every 120 degrees while it is variable all over the 360 degrees domain, for each given hardening state of the material. The starting points to calibrate a Yield Model are the flow curves of the material obtained under different stress states. Tensile tests are used to obtain the flow curves for  $X=1$  but the way to evaluate them is not straightforward. As far as properly designed tensile specimens undergo uniaxial and uniform stress and strain distributions, the simple engineering curve easily delivers the true curve via the known logarithmic formulae; under the above hypotheses, the true curve is also perfectly coincident to the flow stress-strain curve, which is the only one properly expressing the hardening of elastoplastic materials. Unfortunately, the necking inception causes the loss of strain uniformity along the specimen axis thus, beyond the necking onset, the logarithmic formulae applied to the engineering curve become unsuitable for delivering the true stress (current ratio of load to minimum cross section) nor the true strain (logarithm of the ratio between the undeformed and current neck area). Furthermore, if also the post-necking true stress is obtained by any other mean, the increasing triaxiality due to the progressive necking makes the Mises stress more and more different from the above true stress and, then, the hardening cannot be directly measured anymore. Then, cross section-based measurements become essential for calculating the local true strains and true stresses at the neck but, at the same time, the effect of the stress triaxiality on the true curve must be taken into account for converting the true curve in the Mises curve. The conversion of the true stress into the Mises stress has already received considerable efforts in the literature

and, despite its exact closed-form solution is not yet available, the problem has been solved from an engineering viewpoint. Different semi-empirical solutions with various degrees of accuracy and ease of use are available for translating the true curve into the flow curve, including among others the most famous one by Bridgman (1956), the MLR material-independent correction by Mirone (2004a) and the iterative finite elements (FE)-based reverse engineering approach firstly proposed by Ling (1996). Instead, the determination of the post necking true curve from experiments, based on the history of the evolving neck section, can only be achieved by experimental techniques of increasing difficulty depending on the specimen geometry:

- For round smooth specimens, the optical measurements of the minimum neck diameter can be done by video recordings and basic image analysis for distance measurement (Mirone et al., 2017; Noble et al., 1999; Le Roy et al., 1981), which is a rather simple technique for research purposes but is not yet common in industrial procedures.
- For thin sheet specimens, the two-dimensional DIC technique is the straightest option for measuring the true strain distributions and, in turn, for also determining the current cross section under diffused necking thanks to the volume conservation. Although the DIC technique for determining the true curve of thin sheets is quite common for research applications, it is definitely more complex and expensive than the simple optical measurement of a distance (Mirone & Corallo, 2010b; Sato et al., 2015). Technical problems like decorrelation and detachment of colour pattern before the specimen failure for very ductile metals, together with cost reasons make such technique only limited to rather important industrial R&D activities.
- For specimens with square and thick rectangular cross section things are still more complicate, because only 3D stereoscopic DIC techniques can deliver the effective strains and the current area of the shrinking cross section (Grytten et al., 2009; De Almeida et al., 2008; Besnard et al., 2012), allowing the successive determination of the experimental true curve.

The post-necking phase is crucial for many ductile materials exhibiting small necking strains and large failure strains; in fact, several studies investigated how the material behaves, beyond the stage of the stresses/strains localization, in the specimens typically adopted for characterization purposes. The already cited method by Bridgman (1956) requires the experimental measurement of the evolving curvature radius of the necking profile together with the neck diameter, and transforms the true curves into estimations of the Mises curves affected by approximations up to 15%, as it is also highlighted by La Rosa et al (2003), Celentano et al (2004) and Celentano et al (2005). The MLR function, proposed by

Mirone (2004a), does not require the experimental efforts intrinsic in the Bridgman method and delivers a lower error level within 5%. Such approach applies to smooth tensile specimens independently of their cross section although, so far, the cylindrical specimens have been usually preferred because they allow a simple determination of the resisting cross section and, in turn, of the true curve to be transformed in Mises curve. Ling (1996), as well as Joun et al. (2008), proposed iterative FEM-based procedures for obtaining the Mises stress–strain curves, where either the engineering curves or the load-displacement curves from experiments were used as the target functions to be reproduced by FEM. Zhang et al. (1999) proposed a method to overcome the issue of the resisting area in flat specimens with a function relating the total area reduction to the thickness reduction at a single specific strain level. Zhang et al. (2001) extended the same method to materials with isotropic elastic proprieties but anisotropic plastic proprieties. Cabezas et al (2004) made an experimental and numerical study of the mechanical behaviour of SAE 1045 steel sheet specimens during the conventional tensile test, extending the procedure they proposed for cylindrical specimens. Kim et al (2013) determined the true stress–strain curves of three types of sheet metals, namely, DP780, TRIP780 and EDDQ up to the initial stage of localized necking, by using a full-field measurement technique combined with the virtual fields method (VFM). However, the engineering approach is still frequently adopted instead of the true one for the material characterization within industrial applications, despite its known poor accuracy, because of its ease of use. In fact, the engineering curves just require the experimental measurement of the current elongation over a given gage length, which can be done by very simple sensors; instead, the true curves require the experimental measurement of the shrinking cross section, which needs the implementation of more complicate optical techniques. Verleysen et al. (2009) and Verleysen & Degrieck (2004) highlighted the deviation occurring in the post-necking range between the elongation-based engineering strains and the effective maximum local strain in split Hopkinson tensile bar (SHTB) tensile specimens, based on image analysis measurements. Mirone et al. (2017) shown that, during high strain rate tensile tests on a mild steel by Hopkinson bar, the true strains at failure are up to 3 times greater than their engineering counterparts, depending on the specimens slenderness.

### **1.3 Dynamic Characterization Literature Review**

The effect of the strain rate on the elastoplastic response of metals consists of a positive dynamic amplification of the equivalent stress, usually modeled by monotonically increasing functions of the strain rate, saturating at strain rates within the range of those achieved in Split Hopkinson Tensile Bar (SHTB) tests, as in the Johnson-Cook (Johnson & Cook, 1983), Cowper-Symonds (Cowper & Symonds,

1957) and Zerilli-Armstrong (Zerilli & Armstrong, 1987) formulations. The tensile tests performed at high strain rates by way of the SHTB are subjected to the same length-induced and necking-induced stress-strain uniformity issues typical of the static tension tests, together with other possible inaccuracy causes inherent to the strain-rate-dependent nature of the SHTB tests. The strain gauge readings on the input and output bars only allow to derive the gross elongation rate of the entire specimen, which always includes the contribution of the specimens shoulders and also hides any information about the post necking strain localization. The reference to the initial cross section of the undeformed specimen deteriorates the accuracy of the stress, whose distributions also undergo significant gradients and non-uniformities after the necking onset. Thus, the standard SHTB formulation is rather dependent on the specimen geometry and returns approximate stress, strain and strain rate. Verleysen et al. (2004), Verleysen & Degrieck (2004) and Sato et al. (2015) addressed this topic by providing a quantitative estimation of how much the elongation-based engineering strain, based on classical SHTB strain gauge readings on the bars, differs from the effective maximum local strain on the specimen, based on image-analysis measurements. Mirone (2013) also evaluated the necking-induced progressive deviation of the local true strain and true strain rate from the nominal (engineering) strain and strain rate. When the strain measurements in SHTB experiments are only based on strain gauge readings, without high speed camera image analysis, the initial gage length of the specimen may greatly affect the measured engineering strain, as also pointed out by Rusinek et al. (2005), Osovski et al. (2013), Rodriguez-Martinez et al. (2013) and Rotbaum & Rittel (2014). The specimen length also influences the ringing time required for attaining equilibrium of the forces at both specimen ends, as evidenced in Rusinek et al. (2005) and Yang & Shim (2005). The non-uniformity of the stress distributions and their deviation from the stress uniaxiality are directly related to the specimen shape and to the necking-induced perturbations, but the latter issue and its interaction with the strain rate are not yet fully resolved in the literature. The stress state is analysed in Anderson et al. (2014) and Roth & Mohr (2014) accounting for the dynamic necking; the stress triaxiality is observed for checking its influence on the whole stress-strain response. Cadoni et al. (2011) analysed, among other mechanical characteristics, the variation of the necking strain with the strain rate for aluminium alloy 7039 T-651 and for titanium alloy Ti-6Al-4V. Rusinek et al. (2005) correlated the critical impact velocity and multiple necking to the energy storage capability of specimens, Besnard et al. (2012) implemented stereocorrelation techniques for in-depth necking measurements, while Sato et al. (2015) adopted digital image correlation to the same subject for getting detailed distributions of necking-affected strains and fracture surfaces. Osovski et al. (2013) found a deterministic relationship between the position of the necking along the specimen axis, with possible multiplicity, the wave propagation speed and the specimen length. Guan

(2014) proposed an upgrade of the Hart criterion for identifying the dynamic necking onset, while Vaz-Romero et al. (2016) found a relationship between the specimen size and the necking speed development. The dynamic strain localization is also successfully analyzed and modeled by Tarigopula et al. (2008) via coupled imagery and numerical techniques. Other necking-related counter-intuitive outcomes are also reported by Rotbaum et al (2015) who discussed the apparent insensitivity of notched specimens under dynamic loads exhibiting localization and failure far from the notches, which, from the viewpoint of the stress uniformity and triaxiality, can be regarded as an artificially generated neck already active at the first yield. Detailed analyses of the interaction between necking and strain rate are also provided by Rusinek et al. (2005), who relate the critical impact velocity to the wave length and to the position where the neck originates along the specimen axis, and by Yan et al. (2014) who assess the variability of the necking onset depending the strain rate for two different alloys. The occurrence of multiple necks and their retardation, together with the capability of gross energy absorption by the deforming specimens, can be directly related to the strain rate and to the specimen length, as discussed in Yang & Shim (2005), Nilsson (2004), Besnard et al. (2012), Zaera et al. (2014), Guan (2014), Xue et al. (2008). Peroni et al. (2015) developed a numerical procedure which allows to derive the dynamic material hardening by iteratively guiding the deforming mesh profile to comply to the experimental necking profile, acquired by speed camera.

## 1.4 Objective of the Study and Thesis Overview

Despite the several yield models available in the literature, there is not a universally accepted one, considering that everyone has its pros and cons. In this thesis, a new flexible and easy-to-calibrate yield model including a dependence on both the triaxiality factor  $TF$  and the deviatoric parameter  $X$  is proposed, including the functions by von Mises and by Tresca as special cases of full insensitivity and of reference sensitivity to  $X$ , respectively. Experimental data from the literature including mixed tension/torsion tests are used for assessing the predictive capability of the yield model by way of Fortran subroutines implemented in finite element simulations of the experiments.

Regarding the static experimental characterization by means of tensile tests, it is clear that a method for obtaining the true curves of materials just from the engineering curves would be highly desirable. In fact, such method would have the benefits of the simple experimental procedures typical of the engineering approach while maintaining at the same time the accuracy degree typical of the true approach. In this thesis, a very simple new way for obtaining the true curve of a material with just “engineering efforts” is presented. The starting consideration, common to the derivation of the MLR correction in Mirone (2004a), is that the necking only affects

the structural response of specimens due to geometry changes, and such changes are somehow independent of the specimen material. This is similar to what happens to columns under buckling whose deformed shape depends on the column geometry and on its constraints rather than on its material properties. A set of tensile tests with different arbitrary material hardening curves and different specimen shapes is simulated by finite elements. For each given specimen shape, the true curves predicted by FEM are demonstrated to be directly related to the engineering curves, via the proposed MVB functions, independently of the considered material. The material-independent MVB functions are then provided for the considered geometries including round, flat thick and flat thin tensile specimens, allowing to derive the true curves from the engineering curves without the need of any further experimental measurement. The validity of the MVB functions is finally demonstrated through tests data from experiments and from the literature.

Dynamic characterization is also object of the present study. Firstly, the issues regarding the materials characterization by means of SHTB setups are discussed. Two series of SHTB tests on different metals are considered, the first one based on the classical Hopkinson-bar techniques, the second one based on high speed camera-assisted SHTB tests allowing to derive the post necking true stress, true strain, and true strain rate. The experimental findings from the standard SHTB tests are firstly used to assess the influence of the initial gage length/diameter ratio ( $L/d$ ) of smooth specimens on the engineering stress, strain and strain rate and, in turn, on the overall engineering characterization at high strain rates. The engineering stress, strain and strain rate from the classical SHTB experiments are then compared to the true stress, strain and strain rate from the high speed camera-assisted SHTB tests, in order to attempt a reliable quantitative evaluation of the approximations intrinsic in the engineering approach. The camera-assisted experimental data at different strain rates also show that the necking onset significantly affects the strain rate sensitivity and the dependence of the true curves on the strain rate. A new aspect of the dynamic characterization by means of SHTB setups is also shown and discussed in the present research. The strain rate effect is determined by static and high strain rate experiments on a mild steel named FEN steel, where the evolving resisting cross section and the corresponding load, measured at known time intervals, delivered the true stress, true strain and true strain rates. The dynamic tests are ran on a direct-tension SHTB with different incident waves and different specimens lengths, leading to different nominal engineering strain rates. For each SHTB test, the ratio of the dynamic true stress to the static true stress is calculated at fixed strain intervals and is associated to the current value of the evolving true strain rate; the resulting trends of the dynamic amplification are approximated by different tentative functions expressing the strain rate sensitivity of the FEN steel. Two “extreme” experiments, representative of the entire set of trails, are then simulated by FEM adopting all the tentative strain rate functions: the FEM outcome

compared to the experimental results delivers enough information for proving that an important relationship exists between the necking and the strain rate effect. A discussion is finally provided about the limits, arising from the above interaction, to the effective testability of metals at high strain rates via SHTB equipment.

This thesis includes four Chapters. After the introductory Chapter 1, Chapter 2 is about the static characterization of metals. Firstly, the proposed new Yield model is shown with a first part in which an experimental campaign on Electron Beam Melting Ti6Al4V is discussed and a second part in which the mathematical formulation and the application of the new Yield model to literature data are presented. Secondly the new proposed experimental characterization method, able to convert engineering variables coming from a tensile test to true data, is shown; in a first part, the theoretical background is explained while, in a second part, its application to experimental data is shown. Chapter 3 is about dynamic characterization of metals. Firstly a focus on the experimental issues regarding SHTB dynamic tests and, in particular, the comparison between the true and the engineering approaches and the influence of the specimen geometry is presented. Then, the freezing of the strain rate amplification effect induced by the necking phenomenon in SHTB dynamic tests is investigated. In a first part, dynamic tests on Electron Beam Melting Ti6Al4V specimens are discussed and in a second part a dynamic campaign on FE370 steel specimens is analysed regarding the evidence of the necking freezing effect. Finally, Chapter 4 discusses about the conclusions and suggestions for future researches.

## **Copyright Statement**

Some passages have been quoted verbatim from the published papers of the author (Mirone et al, 2016b; Mirone et al, 2016c; Mirone et al, 2017).

# 2 Static Characterization and Modelling of Metals

## 2.1 Overview

To simulate the static behaviour of a material it is necessary to have an accurately calibrated yield and damage model able to consider all the possible stress states that such material could undergo. In this Chapter, a new yield model and a new experimental characterization procedure will be discussed.

According to several experiments reported in the literature, the elastoplastic behaviour of metals depends on all the three invariant of stress, represented by the triaxiality factor  $TF$ , the equivalent von Mises stress and the normalized Lode angle  $X$ . In this Chapter, after showing an experimental campaign conducted on Electron Beam Melting Titanium Alloy demonstrating the unsuitableness of the classical Von Mises approach, a new yield model is presented, where the yield surface depends on the Lode Angle and, eventually, also on the triaxiality ratio. The proposed model is identified by a calibration parameter expressing the degree of nonlinearity of the yield with respect to the Lode angle, and a calibration function expressing the maximum variability of the hardening stress at the two extremities of the Lode angle range, corresponding to the uniaxial and to the pure shear stress states. The proposed model has been tested against experimental data from the literature on the Titanium alloy Ti6Al4V, including mixed tension-torsion loading which allowed to control the evolution of  $X$  and to confine its values into different narrow ranges for better investigating the Lode angle effects on the yield response. A yield model must be calibrated and the starting points to do that are the flow curves of the material obtained under different stress states. Tensile tests are used to obtain the flow curves for  $X=1$  but the way to evaluate them is not straightforward. The usual elastoplastic characterization of metals consists of determining the experimental tensile true stress-true strain curve (true curve) and of correcting it for the post-necking triaxiality, in order to obtain an estimation of the equivalent Mises (flow) stress-strain curve. However, especially in the industry, the elongation-based engineering curve is often used because of its simplicity opposed to the cross section-based true curve, which, instead, is less simple to be measured, unless either measurements of the shrinking specimen area and/or digital image correlation for local strains are used. A new methodology is also proposed in this Chapter for translating the engineering curves into the true curves via material-independent mathematical tools named MVB functions, which only depend on the necking initiation strain and on the aspect ratio of the undeformed



cross section. The true curves delivered by the MVB functions can be then translated into the flow curves via the MLR correction, proposed by Mirone (2004a). The MVB functions are found to work properly for various specimens with round, square and rectangular cross sections, provided that the specimens slenderness (ratio of length to section area) is large enough to prevent the necking-induced stress triaxiality to overlap with the triaxiality induced by the specimen shoulders. Nine arbitrary hardening laws are adopted for checking the validity of the MVB functions by finite elements, encompassing very different combinations of early/medium/late necking strains and low/medium/high hardening slopes. The flow curves of the above arbitrary materials are obtained as Ludwik functions, which, beyond the necking onset, become linear true curves corrected via the MLR function. It is worth noting that such hypothesis about the flow curves, widely supported by literature data, also imposes a remarkable constraint to the way the curvature of the flow curve and, then, the hardening itself, may evolve in the post-necking range. The material independency of the relationships between engineering curves and true curves nicely complies with the evidence that the necking evolution is a purely geometric phenomenon, as it was also found in previous works. The experimental validation is provided by in-house tests and by literature data, referred to round, thick plate and thin sheet specimens.

## **2.2 Yielding, Anisotropy and Lode Angle Dependence**

### ***2.2.1 Static Response of Titanium Alloy Produced by Electron Beam Melting***

#### ***2.2.1.1 Electron Beam Melting Ti6Al4V***

The Ti6Al4V alloy, known also like F136, is by far the most used titanium alloy. In general, the titanium alloys have an austenitic  $\alpha$ -phase stable at high temperatures and a martensitic  $\beta$ -phase stable at lower temperatures. The F136 is a mixed  $\alpha+\beta$  alloy. Adding aluminium tends to stabilize the  $\alpha$ -phase, while vanadium stabilizes the  $\beta$ -phase.

The Electron Beam Melting (EBM) process developed by Arcam allows for end products with complex structures and geometries that, in many cases, are impossible to obtain by foundry process and standard machining techniques. EBM is an advanced process in the Solid Free Form Fabrication Industry, which consists in the manufacture of components obtained directly from the CAD model. The basic idea of this technology is to get the final product building it layer by layer; the geometric information, obtained from the 3D model, is translated into the product by melting the metal powder using an electron beam. This process can be applied to different alloys. The speed of growth is about 60 cm<sup>3</sup>/h and the thickness of the metal powder layers vary from 0.05 to 0.20 mm. After each melting process, a movable element passes through the entire surface positioning the new powder

layer. Table 2.1 shows the chemical composition of the powder used for producing Ti6Al4V alloy.

Arcam Ti6Al4V						
Al	6%	Fe	O	N	H	Ti
V	4%	0.03%	0.015%	0.01%	0.003%	Bil

Table 2.1 Chemical composition of the powder used for the Ti6Al4V alloy

The whole production process may confer a certain degree of anisotropy to the components. The material behaviour of the EBM alloy may be orientation-dependent in terms of stress-strain elastoplastic response as well as in terms of damage sensitivity and ductile fracture under given triaxiality histories.

### 2.2.1.2 Experimental Campaign

The static behaviour of a sintered Ti6Al4V alloy is investigated here by way of quasistatic tension and torsion tests, part of a greater experimental campaign described here including also dynamic tension tests, which will be discussed in Chapter 3.3. In particular, five static tensile tests, three static torsion tests and two high strain rate tests have been carried out. The outcome of the static experiments will give information about the Lode Angle influence on the behaviour of the material. Moreover, comparing such results to similar tests results from the literature concerning Ti alloy obtained by classical metallurgical techniques, will give some indications about how the technological process may affect the final performance of the material and the component.

The considered specimens, all with the same shape (*Figure 2.1*), were produced by the MT Ortho Srl by way of an Arcam Q10 machine using EBM technology, capable of melting successive metal layers perpendicularly to the specimen axis.

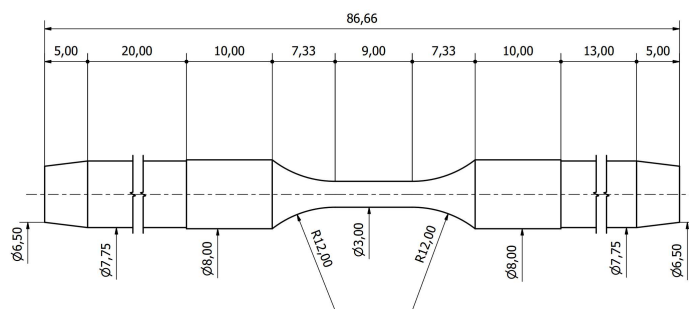


Figure 2.1 Specimen geometry

The static tensile and torsion tests have been performed using a Zwick/Roell Z100 machine, retrofitted with a torsional actuator and the respective control system, together with a camera recording for image acquisition and analysis (*Figure 2.2*). Instead, the dynamic tests have been performed by way of a Split Hopkinson

Tension Bar (SHTB) with fast camera recording (in Figure 2.3 a frame captured at 150'000 fps).

The used production technology for the specimens has the drawback of generating specimens with a very high superficial roughness that can be only partially rectified with after production mechanical finishing. This characteristic causes a difficult post processing analysis of the camera images, especially in the dynamic tests where a lower resolution is essential for achieving high frame rates. Moreover, the tolerance of about 0.2 mm and the ellipticity of the cross sections together with the small size of the specimens generates differences from the nominal diameter up to 6%.



*Figure 2.2 Static tensile test*

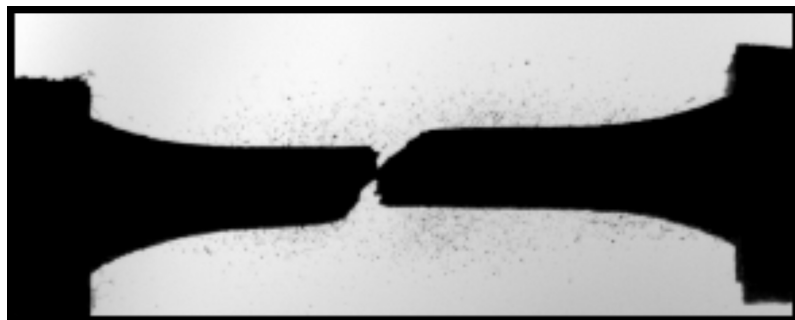


*Figure 2.3 Fast camera image of a dynamic tensile test*

### **2.2.1.3 Static Tests Results**

*Figure 2.4* shows the Force-Displacement curves of the tensile static tests extracted directly from the machine, showing a significant scattering of both maximum loads and displacements at fracture within the series of five specimens. The maximum load difference is due to the small differences in the diameter of the cylindrical segment, while the differences in elongation are reasonably due to the intrinsic

characteristics of the material: the build-up process makes the material very irregular so it can contain little defects that can suddenly initiate the fracture.

The displacement readings of the machine are affected by the elastic deformation of the clamps so, elongation readings from camera images has been performed for getting the real elongation of the centre cylindrical segment of the specimen. The corrected results are shown in *Figure 2.5*.

The static torsion tests have been performed in “free end” modality, that is ideally without axial constrains on the specimen, in order to avoid axial forces and obtain a pure shear loading condition. In *Figure 2.6* are shown the Moment-Rotation results of the static torsion tests extracted directly from the machine. Also in this case the maximum moment difference is due to the small differences in the gage length diameters while the different maximum displacement is reasonably due to the intrinsic sudden damage initiation of the material.

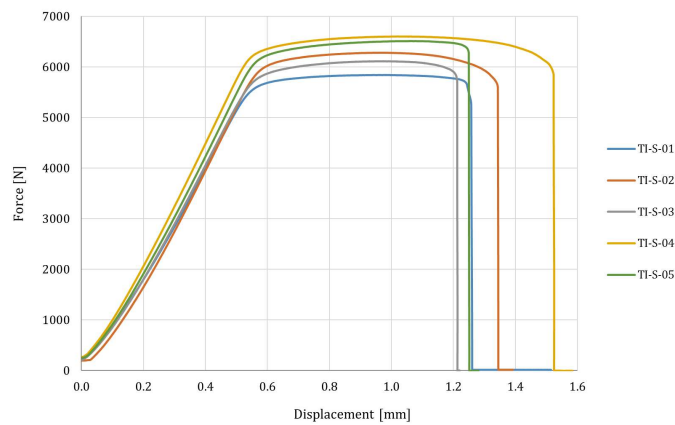


Figure 2.4 Static Tensile tests, Force-Displacement results

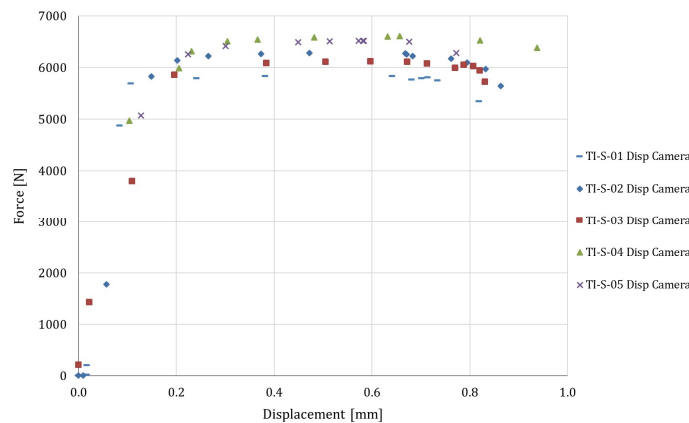


Figure 2.5 Static Tensile tests, corrected Force-Displacement results

Also for the torsion tests, the elastic deformation of the clamps affects the rotation readings but, in this case, is not possible to use camera images analysis to correct them. Then, the curves have been corrected by subtracting an elastic torsion of the

clamps estimated by imposing that torque and torsion at the first yield must agree with the elasticity modulus of the material assumed by literature. In Figure 2.7 are shown the corrected curves.

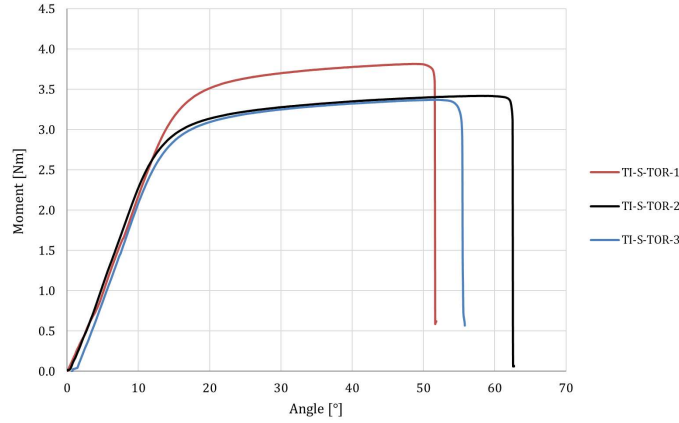


Figure 2.6 Torsion tests, Moment-Rotation results

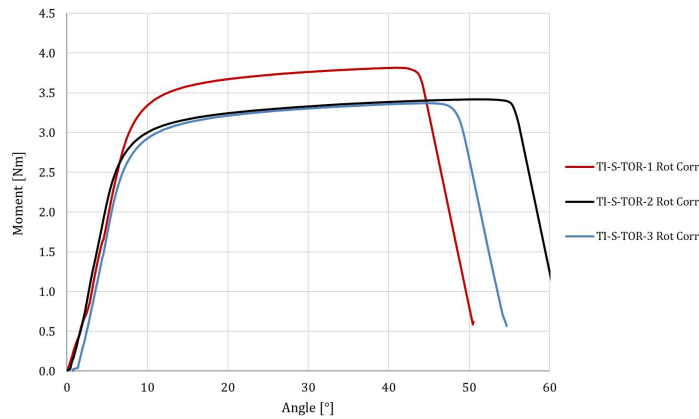


Figure 2.7 Torsion tests, corrected Moment-Rotation results

While for the tensile tests it is possible to obtain the true curves of the material synchronizing the camera images with the load curve of the machine and calculating the instant area of the necking section from the diameter extracted from the images, for the torsion tests a direct calibration procedure proposed by Nadai (1963) was used. Nadai's formulas allow to obtain the  $\tau - \gamma$  curve directly from the Moment – Rotation experimental data:

$$\tau(\gamma_0) = \frac{1}{2\pi r_0^3} \left( \theta_n \frac{dM}{d\theta_n} + 3M \right) , \quad \gamma_0 = \gamma(r_0) \quad (1)$$

where  $\theta_n$  is the rotation normalized by the gage length and  $r_0$  is the initial radius of the specimen. Then it is possible to obtain the  $\sigma - \epsilon$  curve considering the following well known correlations

$$\sigma_{eq} = \sqrt{3}\tau \quad , \quad \varepsilon_{eq} = \frac{\gamma}{\sqrt{3}} \quad (2)$$

Equations (1) and (2) can be applied directly to the experimental results but the obtained  $\tau - \gamma$  curves (solid lines in Figure 2.8) include a lot of noise because the derivative of the moment greatly amplifies the digital approximation of the torque measurement. Then, the same equations are applied successfully to the filtered experimental torque-torsion data, leading to smooth  $\tau - \gamma$  curves (dashed lines in Figure 2.8). As it is possible to see in such figure, there is a big scattering between one curve and the other two suggesting that the higher one is due to an experimental error like in the estimation of the original diameter.

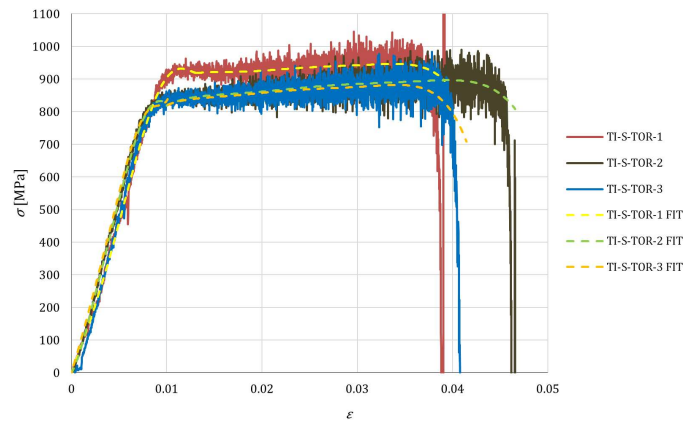


Figure 2.8 Constitutive torsion curves, Nadai EXP vs Nadai FIT EXP

Figure 2.9 shows together the true curves obtained from the static tensile tests (orange circles) and from the static torsion tests (grey triangles) with the correspondent fitting curves.

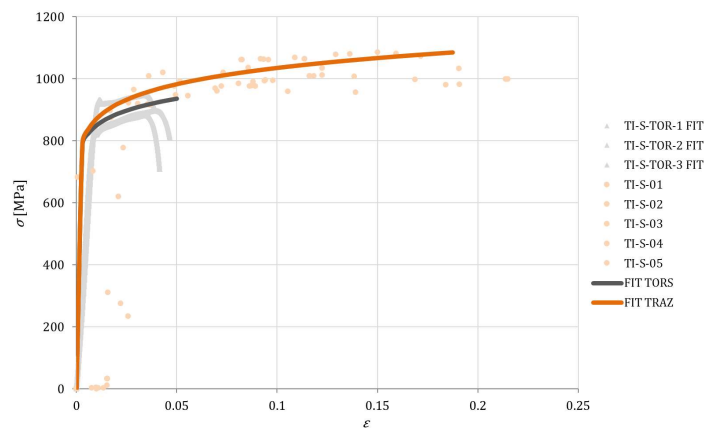


Figure 2.9 True curves, Static Tensile vs Static Torsion

This graph must be analysed considering that, as already highlighted, the build-up process makes the material very irregular so it can contain little defects that can suddenly initiate the fracture. However, it is possible to see how the deformation at fracture is less than 0.05 for all the torsion tests and up around 0.20 for the tensile tests, therefore there is lode angle influence in terms of damage sensitivity and ductile fracture. Moreover, considering the fitting curves, it is possible to see also a lode angle influence in the stress-strain elastoplastic response despite the very low fracture strain of the torsion tests.

#### 2.2.1.4 Comparison with Literature Data

The fitting curve of static true tensile curves obtained in this thesis work from EBM Ti6Al4V specimens with axis orientation perpendicular to the melting plane (UNICT curve) is now compared to the following literature data:

- Static curves from rolled Ti6Al4V by Galàn et al. (2013), Peirs et al. (2011) (*UGHENT* curve),
- Static curve from rolled Ti6Al4V by Allahverdizadeh et al. (2015) (*POLIMI* curve),
- Static curves from EBM Ti6Al4V specimens with axis orientation parallel and perpendicular to the melting plane by Rizza (2015) (*UNICT PW* curves).

Figure 2.10 shows the above comparison with the curves marked with “\*” obtained by transforming the engineering curves through the well-known relations  $\sigma = S^*(1+e_p)$  and  $\varepsilon = \ln(1+e_p)$  until the necking onset and completing them with a linear extension tangent to the curve, as a reasonably approximate prosecution of the true curve.

The orientation of the EBM specimens with respect to the melting plane of the machine has a great effect on the material behaviour. When the axis of EBM specimens is parallel to the melting plane, the static response of the alloy is very similar that of the rolled alloy Ti-6Al-4V tested at the UGHENT and at the POLIMI. On the other hand, the specimens with axis perpendicular to the melting sections tested by Rizza, exhibit a static behaviour very similar to the initial response of the static specimen tested within this thesis work, unless that the former curves are derived from the engineering curves then only extend up to strains of about 0.1, while the latter ones extend up to failure at more than twice the above strain.

All this data clearly shows that the axis orientation perpendicular to the melting plane decreases the static stress response of about 10% with respect to the case when the axis is parallel to the melting plane.

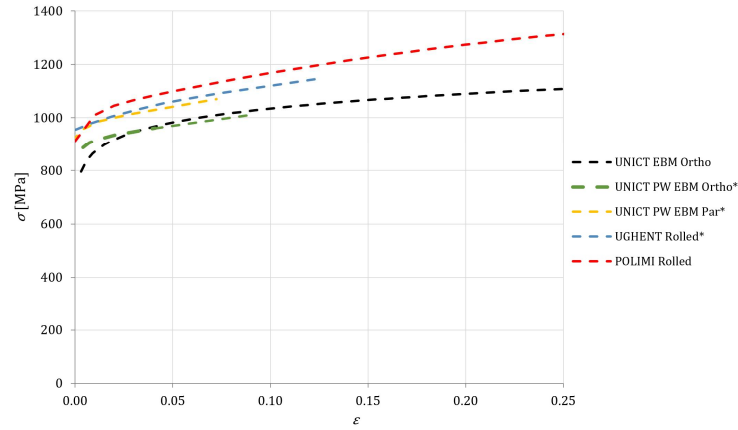


Figure 2.10 True tensile curves – Comparison with literature data. \*Obtained from engineering curves until neck + linear extension

In conclusion, it is possible to assert that the EBM Ti6Al4V is a significant lode angle sensitive material looking both at the differences between torsion and tensile curves of specimens with the same orientation in respect to the melting plane and at the differences between tensile curves of specimens with different orientation in respect to the melting plane (anisotropy could be seen as a lode angle dependency). To simulate correctly a material with this kind of behaviour, it is necessary to use a lode sensitive model as the novel one proposed in the following section.

## 2.2.2 New Yield Model

### 2.2.2.1 Mathematical Formulation

A given stress tensor corresponds to a point in the space of principal stresses and can be either identified by the Cartesian coordinates  $s_1, s_2, s_3$  in a rectangular reference system or by the Haigh coordinates in a cylindrical reference system. The stress coordinates also express the three invariants of the stress tensor which can be combined each other in the following parameters:

$$\sigma_{Mises} = \sqrt{\frac{1}{2}[(\sigma_1 - \sigma_2)^2 + (\sigma_3 - \sigma_2)^2 + (\sigma_1 - \sigma_3)^2]} \quad (3)$$

$$X = \text{Sin}(3 \cdot \vartheta) = \frac{27}{2} \cdot \frac{(\sigma_1 - \sigma_H) \cdot (\sigma_2 - \sigma_H) \cdot (\sigma_3 - \sigma_H)}{\sigma_{eq}^3} \quad (4)$$

$$TF = \frac{\sigma_H}{\sigma_{eq}} = \frac{\sigma_1 + \sigma_2 + \sigma_3}{3 \cdot \sigma_{eq}} \quad (5)$$

where  $\sqrt{\frac{2}{3}} \cdot \sigma_{Mises}$  is the radial coordinate of the stress state (Figure 2.11) based on the second stress invariant, the deviatoric parameter  $X$  is the Lode angle  $\theta$  (third invariant of deviatoric stress) normalized over +/- 30 deg intervals, and the triaxiality factor  $TF$  expresses the axial coordinate (related to the first stress invariant and to the hydrostatic stress  $\sigma_H$ ), normalized to the equivalent stress.



Considering that isotropy is assumed to apply, the Yield Surface (YS) has a tri-lobe symmetry around the  $\{1, 1, 1\}$  axis. In case of positive-negative symmetry (yield stresses in tension and compression identical each other), then a six-lobed symmetry applies.

The greatest possible evidence of the Lode angle affecting the yield of some materials is given by the difference found between the hardening curves in pure tension and in pure torsion.

The phenomenological YS proposed here is a combination of the von Mises and the Tresca surfaces, based on a Tresca-like linear cross section with straight edges connecting the pure shear and the purely uniaxial yield conditions, over which a tunable amplification is superimposed in the form of a quadratic function of the Lode angle, ensuring a flexible calibration parameter with good control of the convexity of the yield surface.

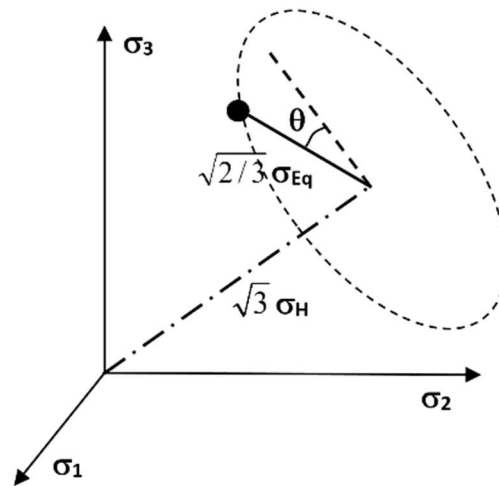


Figure 2.11 Cylindrical, stress invariants-based coordinates

As usual for metals, the effect of the triaxiality on the yield surface is supposed to be negligible, then the yield surface has a uniform cross section along the trisector axis, and the whole surface can be then identified by its intersection with the deviatoric plane. However, a tapered cross section modelling the effect of hydrostatic pressure on the yield can be easily included as in Mirone (2014).

Assuming symmetrical behaviours in tension and compression the definition of the yield surface can be limited to the interval of Lode angles  $[0, 30]$ .

According to the scheme of Figure 2.12, a Cartesian reference U-V is assumed on the deviatoric plane, so that the U axis identifies a zero Lode angle, pure shear direction. The red line identifies a Tresca-like yield surface with 12 straight edges accounting for a Lode-angle dependent yield stress, spanning between  $\sigma_{TE}$  in pure tension and  $\sigma_{SH}$  in pure shear.

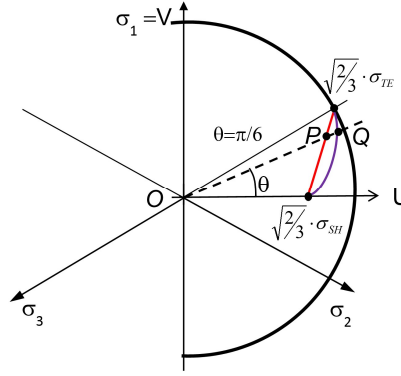


Figure 2.12 Yield surface edge definition

Such a segment is described by the equation of a line passing across the above points on the deviatoric plane:

$$V = \frac{1}{m} \cdot \left( U - \sqrt{\frac{2}{3}} \cdot \sigma_{SH} \right); \quad m = \frac{\sigma_{TE} \cdot \cos(\pi/6) - \sigma_{SH}}{\sigma_{TE} \cdot \sin(\pi/6)} \quad (6)$$

The intersection  $P$  between such segment and the general direction at Lode angle  $\theta$  can be then easily found, and its distance from the origin returns the current yield stress according to the straight-edged yield surface connecting the pure shear and the uniaxial yield stresses:

$$\overline{OP}(\vartheta) = \sqrt{U_p^2 + V_p^2} = \sqrt{\frac{2}{3}} \cdot \sigma_{SH} \cdot \frac{\sqrt{1 + \tan^2(\vartheta)}}{1 - m \cdot \tan(\vartheta)} \quad (7)$$

Then, a Lode angle-dependent quadratic amplification of the yield stress is introduced for better flexibility as a second order multiplicative term, whose effect is qualitatively depicted by the blue curve in Figure 2.12. Such a quadratic amplification spans from 1.0 at the extremities of the Lode angle range ( $\theta=0$  and  $\theta=\pi/6$ ), up to the desired calibration value at the desired representative angle  $\theta^*$ , so providing a single calibration parameter. As far as the calibration value is positive, the resulting yield surface is convex in the Lode angle range  $(0, \pi/3)$ , which is where convexity must be ensured.

The radial coordinate of the point  $Q$  is then obtained by incrementing that of the point  $P$  by the above quadratic term, and the equivalent stress is finally defined as in equation (8).

$$\sigma_{Eq}(\vartheta) = \sqrt{\frac{3}{2}} \cdot \overline{OQ}(\vartheta) = \sigma_{SH} \cdot \frac{\sqrt{1 + \tan^2(\vartheta)}}{1 - m \cdot \tan(\vartheta)} \cdot \left[ 1 + qa \cdot \frac{(\vartheta^2 - \pi/6 \cdot \vartheta)}{\vartheta^{*2} - \pi/6 \cdot \vartheta^*} \right] \quad (8)$$

where  $qa$  is the only calibration parameter, required together with the  $m$  function, for assessing the quadratic amplification of the yield due to the Lode angle, and for finalizing the current shape of the yield surface.

The hardening effect in equation (8) is provided by the evolving scale factor  $\sigma_{sh}$ , which is the current, strain-dependent yield stress in pure shear, while the possible variability of the surface shape during the straining process is included in the term  $m$ , which expresses the strain-dependent relationship between the hardening stresses under pure uniaxiality and pure shear. The degree of curvature of the surface edges is instead assumed to be constant as the parameter  $qa$ , so far, is assumed to be a strain-independent material constant.

Then the yield surface can be also expressed in the fully equivalent form of eq. (9), where the hardening is accounted for by the more familiar hardening stress in pure tension  $\sigma_{TE}$ , playing the role of the evolving, strain-dependent scale factor:

$$\sigma_{Eq}(\vartheta) = \sigma_{TE} \cdot \left( \cos\left(\frac{\pi}{6}\right) - m \cdot \sin\left(\frac{\pi}{6}\right) \right) \cdot \frac{\sqrt{1 + \tan^2(\vartheta)}}{1 - m \cdot \tan(\vartheta)} \cdot \left[ 1 + qa \cdot \frac{\left(\vartheta^2 - \frac{\mu}{6} \cdot \vartheta\right)}{\vartheta^{*2} - \frac{\mu}{6} \cdot \vartheta^*} \right] \quad (9)$$

In principle, the complete identification of such a yield surface can be made by two base experiments in pure tension and in pure torsion, providing the hardening stresses ( $\sigma_{TE}$ ,  $\sigma_{SH}$  and  $m$ ), plus one more single test at the intermediate Lode angle  $\theta^*$ , for calibrating the additional parameter  $qa$ .

More reasonably, the parameter  $qa$  can be found by minimizing the discrepancies of finite elements runs against a finite set of tests at intermediate Lode angles.

If  $m = \tan(15 \text{ deg})$ , then the parameter  $qa$  can be tuned for making the yield surface to collapse on the Mises surface, depending on the arbitrary calibration angle  $\theta^*$ . If instead  $m = 0$  and  $qa = 0$ , the Tresca surface is obtained as a special case.

The variability of  $qa$  with the plastic strain can be eventually introduced, making it a calibration function instead of a calibration constant, so allowing to model further strain-promoted shape evolutions of the yield surface and then giving one more degree of flexibility to the proposed Yield model.

Figure 2.13 shows four possible yield surfaces for a given reference uniaxial yield stress, where the shear yield stress is greater or smaller than the Tresca yield stress (outward or inward protruding dodecagons) and the quadratic amplification is either turned off or is imposed to be 20% at 15 degrees (straight or curved edges).

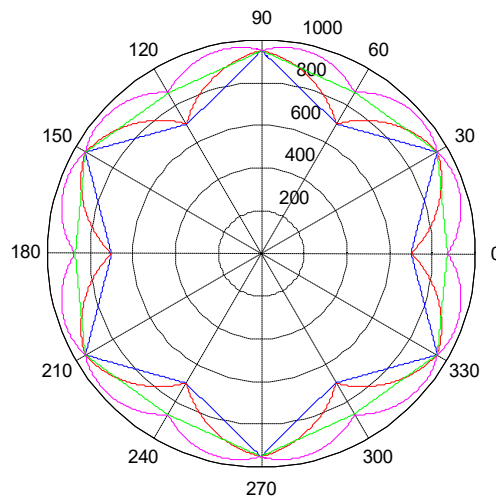


Figure 2.13 Four different Yield surfaces corresponding to a given uniaxial stress and two couples of shear stress / quadratic amplification.

### 2.2.2.2 Calibration to Literature Data

The yield model discussed here is checked against literature experimental data on Ti6Al4V by Allahverdizadeh et al. (2015). Such experimental campaign includes pure tension, pure torsion and mixed tension-torsion tests imposed by a constant tensile preload followed by monotonically increasing torque up to failure, so that the deviatoric parameter can be virtually controlled at the local scale for investigating its effect on the stress-strain response.

In fact, axisymmetric tensile stress states (including uniaxiality as special case) generates  $X=1$ , while the generalized plane strain (including pure torsion as special case) makes  $X=0$ ; mixing both load types in the desired proportions allows to determine and maintain the desired values of  $X$  at the meaningful material points within the specimens.

Material	Series id	Test type	Specimen shape
Ti6Al4V Allahverdizadeh et al.	ATo	Torsion	“
	A20	pre-Tension 20 kN + Torsion	“
	A30	pre-Tension 30 kN + Torsion	“
	A40	pre-Tension 40 kN + Torsion	“
	TFS	Tension	Tens. Flat smooth
	SFB	Shear	Shear Flat butterfly
	TFH	Tension	Tens. Flat holed
	TFN	Tension	Tens. Flat notch. R 6.67
	TRS	Tension	Tens. Round smooth
	TRN	Tension	Tens. Round Notched
	TPB	Three-points Bending	Notched square bar

Table 2.2 Experimental tests by Allahverdizadeh et al.

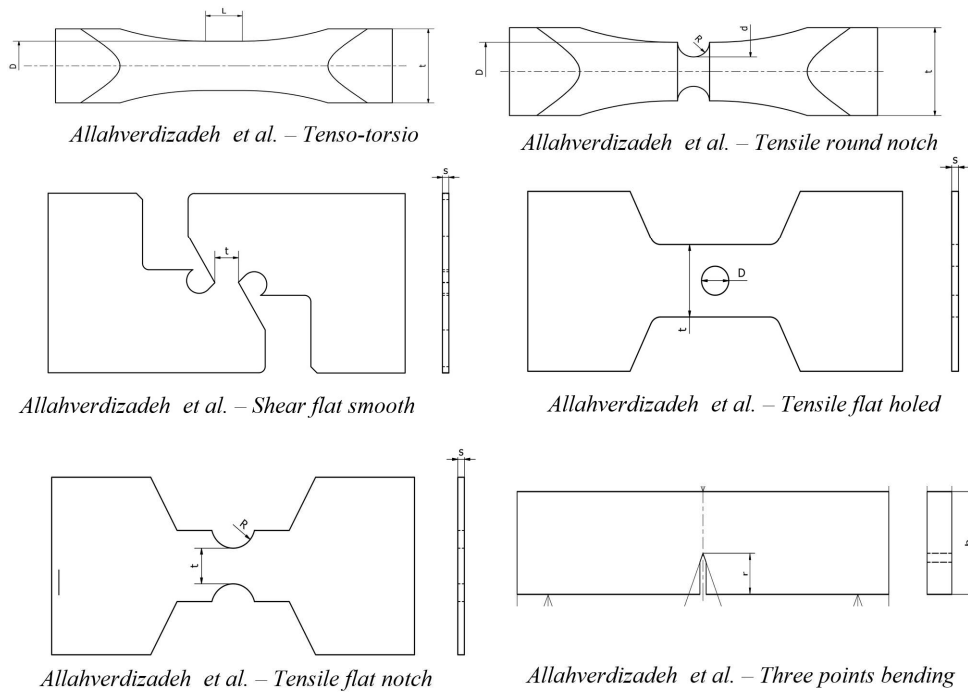


Figure 2.14 Specimens shapes and load modes

In Table 2.2 are identified the tests from literature (Allahverdizadeh et al, 2015) used here for checking the accuracy of the proposed yield model.

Also flat specimens with butterfly-like, grooved and notched shapes are included in the test series according to Figure 2.14, providing further data about particular combinations of evolving X and TF values.

For the Ti alloy considered here, the torque-rotation and load-elongation-diameter curves and the specimens geometry data reported in Allahverdizadeh et al. (2014), Allahverdizadeh et al. (2015) and Allahverdizadeh, N., (2014) allow the derivation of the torsion and tensile flow curves, including for the latter the postnecking correction (e.g. reverse engineering, Bridgman, MLR).

The material hardening functions from tensile and from torsional tests after a general reassessment of the data are summarized in Table 2.3 and plotted in Figure 2.15.

Material	Test type	Flow curves
Ti6Al4V Allahverdizadeh et al.	Tension	$\sigma_{Eq-Tens} = 1335 \cdot \varepsilon_{Eq}^{0.06}$ (pre-necking)
		$\sigma_{Eq-Tens} = 1058 + 1230 \cdot \varepsilon_{Eq} - 550 \cdot \varepsilon_{Eq}^2$ (post-necking)
	Torsion	$\sigma_{Eq-Tors} = 1325 \cdot \varepsilon_{Eq}^{0.08}$

Table 2.3 Material hardening functions in tension and torsion

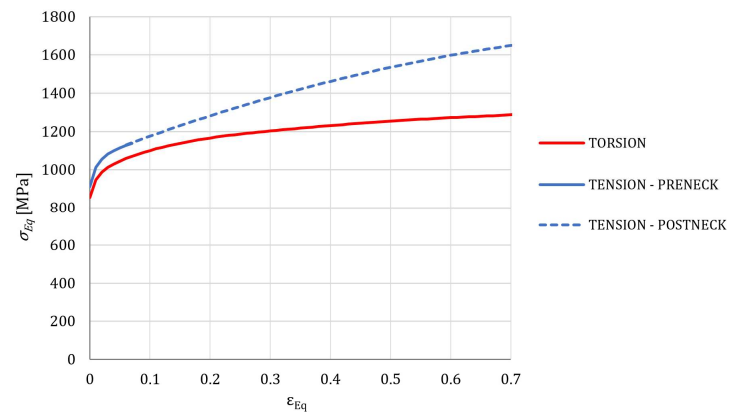


Figure 2.15 Material hardening functions in tension and torsion

The significant departure of the flow curve in torsion from that in tension evidences that the Lode angle plays a key role in the yield of this metal. The evolving function  $m(\epsilon_{Eq})$  for the Ti6Al4V alloy, derived according to the yield model proposed here and to eq. (6), is plotted in Figure 2.16. The initial negative values of  $m$  indicate that, at the beginning of the plastic range, the yield stress in pure shear is intermediate between the Tresca one and the Mises one at the given hardening level. The increasing values of  $m$  imply that the shape of the cross sections of the yield surface progressively changes, and the small protrusion it shows just after the first yield at the pure shear angular coordinate, tends to move inward and becomes less and less pronounced as the plastic strain evolves.

When  $m=0$  the yield in pure shear becomes identical to that of the classical Tresca criteria, although the yield stress at different Lode angles is generally beyond the Tresca prediction; if instead also the quadratic parameter  $qa=0$ , then the whole surface collapses into the Tresca one.

Positive values of  $m$  indicate that the yield surface exhibits inward edges at the zero Lode angle and the yield stress in pure shear is lower than the Tresca prediction at that hardening level.

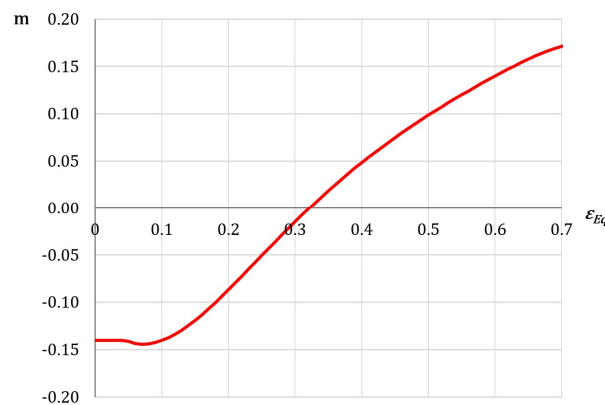


Figure 2.16 The  $m$  function for the considered material

The second yield parameter of the yield model,  $qa$ , is calibrated by finite elements-based reverse engineering, as a compromise allowing to satisfactorily reproduce the macroscopic response (load-elongation and torque-angle curves) of the various mixed tension-torsion tests performed at different combinations of such loading modes.

All the finite elements analyses are based on the update Lagrangian finite general plasticity with additive decomposition of the strains, available in a commercial nonlinear code; the proposed yield criteria and the corresponding associative plasticity are implemented via Fortran user subroutines. The tension-torsion displacements are imposed via contact surfaces where the proper constraints, motions and loads are imposed (see Figure 2.17).

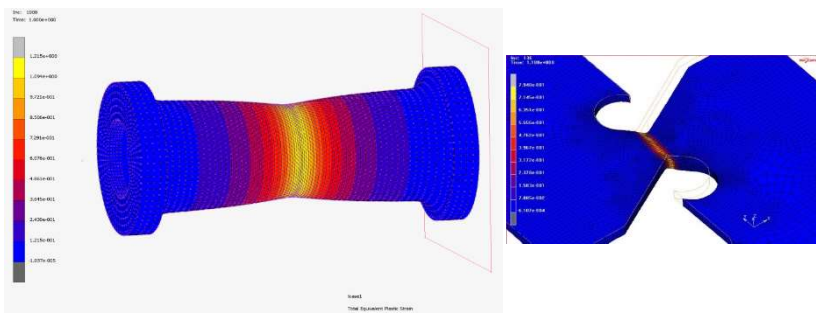


Figure 2.17 Deformed meshes of tension-torsion and flat shear specimens

The value attributed to the  $qa$  parameter for the Ti6Al4V is 0.043 and, together with the  $m$  function in Figure 2.16 and the uniaxial hardening function in Figure 2.15, generates the expanding yield surfaces reported in Figure 2.18 at the strain levels of 0.02, 0.2, 0.4, and 0.6, respectively.

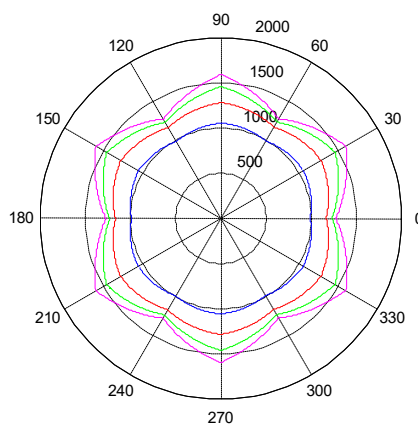


Figure 2.18 Evolving yield surface of the Ti-6Al-4V alloy at different strain levels

The yield surface changes its shape during the straining history, but the degree of curvature of its cross section edges is fixed because of the constant value of  $qa$ . An

upgrade of the model is in progress for making the quadratic amplification  $qa$  variable with the plastic strain, increasing the model flexibility.

The results of the finite elements runs performed with the proposed yield model and with the standard Mises yield criteria are presented in the next section for the various tests by Allahverdizadeh et al.; the data are presented in terms of macroscopical response parameters like load, elongation, torque and twist angle.

### 2.2.2.3 X-dependent Yield Numerical Simulation of Literature Experiments

In Figure 2.19 the experimental results are compared to the predictions of the proposed yield criteria (plots A and C) and to the outcome of finite elements with standard Mises plasticity (plots B and D).

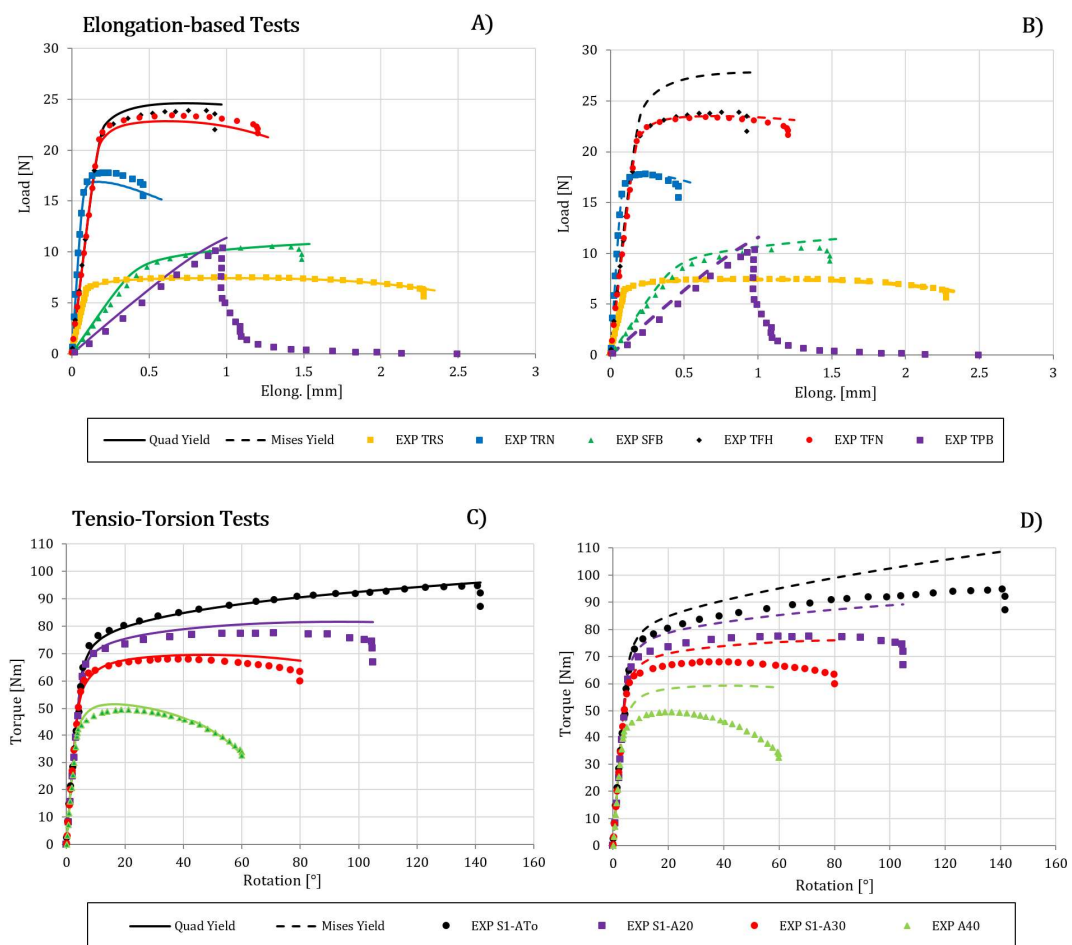


Figure 2.19 Finite elements modelling of experiments by quadratic yield and by von Mises yield

The most important outcome of a Lode angle-dependent yield surface is the differentiation of the evolving yield stress under pure tension from that under pure shear; with this regard the proposed model (black continuous curve in Figure 2.19 C) allows to reproduce very well the experimental data with almost no error (large filled black dots in Figure 2.19 C and D), while the standard von Mises predictions,



typically based on the flow curves from tension, (black dashed line in Figure 2.19 D) generate considerable approximations in simulating the torsion experiments with an error close to 15% at failure.

The data in Figure 2.19 A and B refer to the extension-based tests where, although shear stress at the local scale can be generated due to finite straining, no macroscopical twist nor torque are applied. Here no color code is used for differentiating the curves of the various tests, as the relationship between an experimental set and the corresponding finite element simulation is clearly identified.

All the tests of this series are simulated reasonably by the Mises yield and no great improving is introduced by using the quadratic yield, except for the “tensile flat holed” test, TFH, where the poor accuracy provided by the Mises yield (error beyond 12% at failure) is substantially fixed by the proposed yield model (error close to 3% at failure).

Instead, the data in in Figure 2.19 C and D, for the mixed tension-torsion tests, include a color coding other than the curves symbols, because the Mises-based numerical simulations exhibit such a poor approximation that the curves from a certain simulated test are close to the experimental data from a different test, and the correspondence of the numerical curves to the experimental ones is not always clear. The error at failure of the tensio-torsion simulations based on the Mises yield spans from 15% (pure torsion) to 30% (A40 tests).

Such a discrepancy cannot be due to the damage, affecting the experiments and not modeled by the finite elements. In fact, the progressive microvoid evolution in tension-dominating stress states is known to play negligible role on the value of the local stresses and of the macroscopic load, as confirmed by the good accuracy of the Mises-based finite elements for the elongation-based tests of Figure 2.19 A and B. Instead in Figure 2.19 C and D, the 15% error of the pure torsion, increases up to 30% for the test A40 where the axial component of the stress state is the greater of the lot.

Then, such a poor accuracy of the simulations with Lode angle deviating from 30 degs. can be reasonably attributed to the whole Mises yield criteria alone, and the adoption of the quadratic-yield formulation proposed here is capable of largely reducing the error, which drops down to the range between almost zero (pure torsion) and 8% (A20 test), with no apparent dependence on the mix between tension and torsion.

The stress paths for the A20 and A40 tension-torsion tests at the most meaningful material points in the specimens (mid-thickness and outer surface at the neck section) are acquired from the finite elements runs with the X-dependent yield, and are reported in Figure 2.20 for the “extreme” mixed tests A20 and A40. The stress paths are initially very close to the pure tension because of the tensile preload, then the A20 test quickly departs from uniaxiality after yield because of the low preload,

instead the A40 test where the tensile preload is greater, only later departs from uniaxiality, closer to the first yield condition.

In both cases the paths tend to deviate from their initial straight trajectory, converging toward intermediate stress states at higher plastic strains.

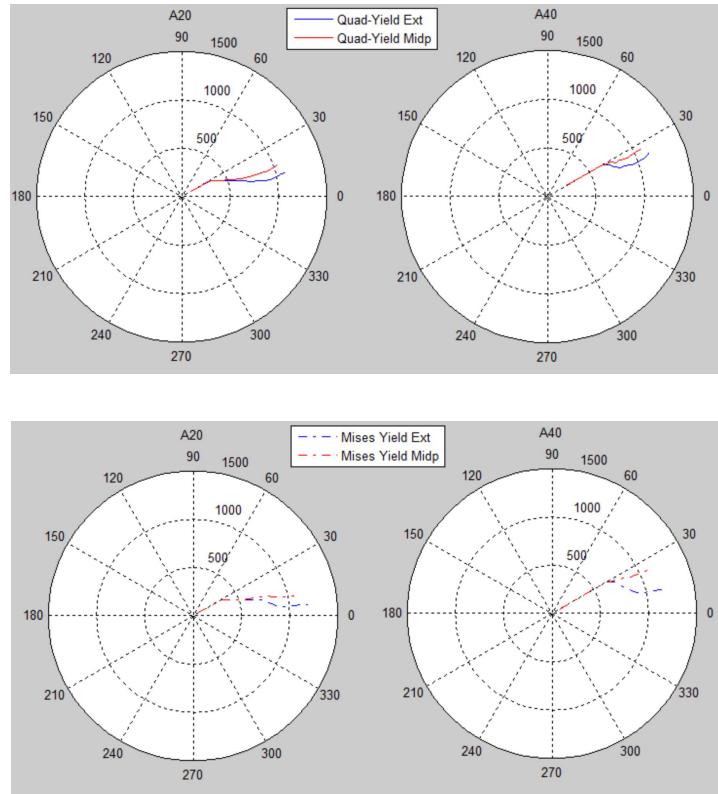


Figure 2.20 Stress histories of A20 and A40 tests at critical material points (mid-thickness and outer surface at the neck section)

As expectable, the larger deviations from uniaxiality occur in the A20 test because the evolving ratio between the torque and the low-level tensile preload is greater than it is in the A40 test.

In both tests, the stress paths of the material points on the outer surface of the specimens deviate from uniaxiality more than the inner ones, because the torque-induced shear stress is null at the specimen core and increases along the section radius toward the specimens surface.

The points on the specimen axis, not reported in Figure 2.20, are subjected to the tensile preload alone, so their stress path evolves along the 30 deg direction until failure. The adoption of the quadratic yield also implies minor modifications of the stress paths, by reducing the variation of the Lode angle between the beginning and the end of each test, as visible by comparing the upper solid line plots of Figure 2.20 to the lower ones.

Summarizing, it is possible to say that the greater departure of the experimental evidence from the Mises criteria, occurring under pure shear conditions, is

reproduced very well by the new yield criteria proposed here; this means that the  $m$ -based feature of the model is capable of correctly reproducing virtually whatever possible departure function of the pure torsion hardening from the purely tensile hardening.

The  $qa$ -based feature which determines the model transition from pure tension to pure shear at intermediate values of the deviatoric parameter might require further adjustments and upgrades.

The single-valued constant  $qa$  resulted to be suitable for correctly modeling the response of the Ti6Al4V alloy but, for different materials, it is very likely that a strain-dependent variable curvature of the edges of the yield surface must be implemented through a multi-valued  $qa$  function of the strain.

## 2.3 Novel Experimental Characterization Method

### 2.3.1 Engineering Curve vs True Curve Vs Flow Curve

The elastoplastic characterization of materials is the identification of the relationship between the equivalent strain and the equivalent stress and it can be done by means of pure tensile tests on a cylindrical specimen. There are three possible curves representing the behaviour of the material with different level of approximation. Starting from the less accurate, they are:

- Engineering Curve
- True Curve
- Flow Curve

The Engineering Curve is obtained relating the Engineering Tension (eq. (10)), calculated as the axial force  $F$  over the initial area of the specimen  $A_0$ , and the Engineering Strain (eq. (11)), calculated as the elongation  $\Delta L_0$  of the gage length over its initial length  $L_0$ .

$$\sigma_{eng} = \frac{F}{A_0} \quad (10)$$

$$\varepsilon_{eng} = \frac{\Delta L_0}{L_0} \quad (11)$$

Such expressions can be considered as the equivalent stress and strain since are true the following hypothesis:

1. In every point of the considered volume of the material (gage length), tensions are perfectly uniform and uniaxial.

2. The test is quasistatic, therefore there is not strain rate influence on the material behaviour.
3. The differences between the initial and the current configuration of the specimen in terms of diameter and gage length are negligible.

The first two hypothesis are reasonably true if the specimen is properly designed and the test speed is sufficiently low. The third one is true only for very low deformations, almost only for elastic phase. The True Curve addresses the imprecisions concerning hypothesis 3. When the strains cannot be considered infinitesimal, tensions and strains must be referred to the actual configuration instead of to the initial configuration to be meaningful. Therefore eq. (10) becomes

$$\sigma_{true} = \frac{F}{A} \quad (12)$$

Eq. (11) is valid only for infinitesimal strains, therefore for finite strains it becomes

$$\varepsilon_{true} = \frac{\Delta L_n}{L} + \frac{\Delta L_{n-1}}{L_{n-1}} + \dots + \frac{\Delta L_1}{L_2} + \frac{\Delta L_0}{L_1} = \int_{L_0}^L \frac{dL}{L} = \text{Log} \left( \frac{L}{L_0} \right) \quad (13)$$

and it is related with the engineering one with the following

$$\varepsilon_{true} = \text{Log} \left( \frac{L}{L_0} \right) = \text{Log} \left( \frac{L_0 + \Delta L}{L_0} \right) = \text{Log}(1 + \varepsilon_{eng}) \quad (14)$$

Considering negligible the elastic strain in respect to the plastic strain, it is possible to consider the volume conservation and write

$$\varepsilon_{true} = \text{Log} \left( \frac{L}{L_0} \right) = \text{Log} \left( \frac{r_0^2}{r^2} \right) = 2\text{Log} \left( \frac{r_0}{r} \right) \quad (15)$$

This last relationship allows to calculate the true strain by means of diameter measuring that is experimentally simpler and more accurate than elongation measuring. The True Curve is much more meaningful than the Engineering Curve in terms of fracture strain and ultimate stress but it does not take into account the perturbations induced by the necking phenomenon, that is the concentration of the strain in a particular section of the specimen. In such condition, the calculated true values are just average values of variables that are very different from point to point in the necking section and does not represent anymore the equivalent values. The necking phenomenon makes the stress state no more uniaxial and uniform and part of the stress state is used to increase the hydrostatic tension; consequently, not all the axial tension considered in the ratio “Force over Area” becomes Equivalent Stress. Therefore, the real Equivalent Curve will be lower the True Curve obtained

before (typically 10-20% lower at fracture for metals). The most known and used method to transform the True Stress into the Equivalent Stress is the one proposed by Bridgman (1952). Such method requires the experimental measurement of the evolving curvature radius of the necking profile together with the neck diameter, and transforms the true curves into estimations of the Mises curves affected by approximations up to 15% , as it is also highlighted by La Rosa et al (2003), Celentano et al (2004) and Celentano et al (2005). The MLR function, proposed by Mirone (2004a), does not require the experimental efforts intrinsic in the Bridgman method and delivers a lower error level within 5%. In the thesis work presented here, the following new slightly modified and more accurate version of the MLR has been obtained and used, called *MLR +*:

$$MLR+= (1 + 0.05(\varepsilon_{True} - \varepsilon_{TrueNeck})) * (1 - 0.6058(\varepsilon_{True} - \varepsilon_{TrueNeck})^2 + 0.6317(\varepsilon_{True} - \varepsilon_{TrueNeck})^3 - 0.2107(\varepsilon_{True} - \varepsilon_{TrueNeck})^4) \quad (16)$$

### ***2.3.2 Relationship between True Curve and Macroscopic Experimental Data: the MVB Functions***

#### ***2.3.2.1 Underlying Concept***

The starting idea behind this thesis work is that the necking phenomenon during tensile tests is strongly shape-dependent while it is rather material independent, provided that specially “translated” strains are adopted as the governing variables. A similar approach was proposed in Mirone (2004a) for deriving the material-independent MLR function, which, beyond the necking onset, converts the true stress into the flow stress only depending on the post-necking true strain, defined as the difference between the current value of the true strain and the value at the necking onset.

Then, a simple procedure for the complete elastoplastic characterization, just relying on the experimental engineering curves, should consist of two steps: the first is the conversion of the engineering curve into the true curve; the second is the conversion of the true curve into the Mises curve.

While the second step can be easily accomplished via the MLR correction or the Bridgman method, the first one is a still remarkably open issue addressed in this research via the MVB functions.

The FEM-based iterative method joins both steps into a single one, but it can be time-consuming and poorly accurate for materials whose engineering curves exhibit long flat plateau, because very small discrepancies between the target functions and the actual FEM response, which may be perfectly acceptable, for these materials can lead to hardening curves with anticipated / delayed necking onset. Furthermore, the FEM iterative approach for getting a material curve can be beyond feasibility for most industrial activities.

As mentioned before, the experimental true curve of round specimens can be determined by simple optical diameter measurement, while it requires slightly more complicated two-dimensional DIC techniques for thin sheets and rather onerous 3D stereoscopy optics for thick rectangular cross sections.

The relationship between the elongation-based engineering curve and the cross-section-based true curve is then investigated here, leading to a solution which simply solves the problem of the cross section measurement during tensile tests.

In order to search for a material-independent correlation between the engineering strain and the true strain, the specimen gage length where the engineering data are acquired must be at least capable of including the entire zone of the specimen really affected by the necking. At the same time, no other factors generating any triaxiality/stress gradients must interact with such necking-inclusive gage length.

This means that the gage length must be at least long enough with respect to the size of the cross section for also including, at its extremities, specimen zones nearly undisturbed by the necking. At the same time, the specimen shoulders must be far enough from the extremities of the gage length, to ensure that the stress gradients they generate do not reach the necking-inclusive gage length.

In other words, an arbitrarily long “undisturbed zone” of specimen should exist between the gage length and the shoulders, where the stress distributions are ideally not affected by the necking nor by the shoulders.

Then, for complying with such requirements, the gage length should be roughly longer than a few times the maximum side of the cross section and, in turn, the overall length of the specimen with constant cross section, extending between the shoulders, should include one or two more lengths of the larger side of the cross section in excess to the gage length.

Specimens exceeding such length requirements will be as well suitable for implementing the procedure proposed here, while specimens below such length requirements are incompatible with it. It is worth noting that the standard testing regulations usually require specimen slenderness in excess of the above minimum requirements.

The volume conservation, applied to the specimen region corresponding to the gage length, ensures that, before the necking onset, the engineering curve and the true curve are related each other by the known eq. (17) and eq. (18).

$$\varepsilon_{true} = \ln(1 + \varepsilon_{eng}) \quad (17)$$

$$\sigma_{true} = \sigma_{eng}(1 + \varepsilon_{eng}) \quad (18)$$

In eq. (17) and eq. (18), the considered engineering stress and strain are referred to the initial undeformed geometry of the specimen (eq. (19) and (20)) while the true

stress and strain are referred to the current deformed specimen configuration (eq. (21) and eq. (22)).

$$\varepsilon_{Eng} = (L - L_0)/L_0 \quad (19)$$

$$\sigma_{Eng} = F/A_0 \quad (20)$$

$$\varepsilon_{true} = Ln(L/L_0) \quad (21)$$

$$\sigma_{True} = F/A \quad (22)$$

After the necking onset, the gage length elongation can only represent the average true strain over a specimen volume undergoing large strain gradients. Then, for getting the current strain at the neck section, the volume conservation must be imposed to the ideal prism corresponding to the neck section itself with an infinitesimal thickness and the true strain can be calculated by means of eq. (23).

$$\varepsilon_{true} = Ln(A_0/A) \quad (23)$$

Eqs. (21), (22) and (23) and (5) show that, apart from the current load, the current area  $A$  of the shrinking neck section is the key parameter for obtaining the true curve by experiments and that it is tightly connected to the true strain.

Below in this chapter it is shown that the FE modelling of tensile tests with the proper specimens, where the necking effect is fully included within a control volume and is also “isolated” from other possible stress perturbations, delivers a material-independent *MVB* function for each specimen geometry considered (i.e. round, thick or thin rectangular cross sections), capable of expressing the relationship in eq. (24) between the engineering strain and the true strain beyond the necking onset.

$$\varepsilon_{true} = MVB(\varepsilon_{eng} - \varepsilon_{eng\_Neck}) \cdot \varepsilon_{true\_Neck}^{0.1} + \varepsilon_{true\_Neck} \quad (24)$$

Combining eqs. (19), (20), (23) and (24), the effective current area of the neck section can be derived as a function of the current gage elongation and, in turn, the current true stress can be easily expressed as the function of the engineering stress reported in eq. (25).

$$\sigma_{true} = \sigma_{eng} * \frac{A_0}{A} = \sigma_{eng} * e^{\varepsilon_{true}} = \sigma_{eng} * e^{\left[ MVB(\varepsilon_{eng} - \varepsilon_{eng\_Neck}) \cdot \varepsilon_{true\_Neck}^{0.1} + \varepsilon_{true\_Neck} \right]} \quad (25)$$

Then, the identification of the *MVB* functions, discussed ahead, constitutes one more confirmation of the material-independence of the necking effect and allows to transform the engineering curve in the true curve without the experimental efforts of the cross section measurements beyond the necking onset.

For completing the elastoplastic characterization of a metal, the true curves obtained by the *MVB* functions can be finally transformed into the Mises equivalent stress-strain curves through the *MLR* correction.

### 2.3.2.2 FEM Simulations

The following six specimen geometries, whose FE models are shown in Table 2.4, are analysed for studying the above relationships between engineering and true data:

- Round cross section diameter 9 mm (gage length 40.5 mm,  $s = 5.08$ );
- Square cross section 12.5 x 12.5 mm (gage length 40.5 mm,  $t = 1$ ,  $s = 3.24$ );
- Rectangular cross section 12.5 x 6.25 mm (gage length 40.5 mm,  $t = 2$ ,  $s = 4.58$ );
- Rectangular cross section 15.9 x 6 mm (gage length 40.5 mm,  $t = 2.65$ ,  $s = 4.15$ );
- Rectangular cross section 12.5 x 2.5 mm (gage length 40.5 mm,  $t = 5$ ,  $s = 7.24$ );
- Rectangular cross section 20 x 1 mm (gage length 50 mm,  $t = 20$ ,  $s = 11.18$ ).

With the following meaning of the shape parameters:

- Thickness ratio  $t = \text{width} / \text{thickness of the cross section}$ ;
- Slenderness ratio  $s = \text{gage length} / \text{square root of the cross section}$ .

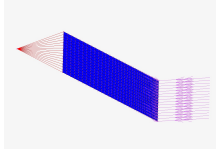
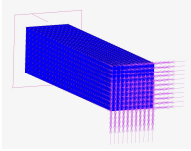
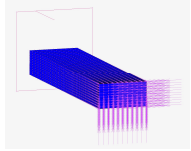
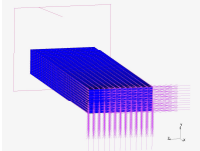
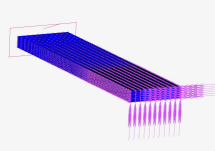
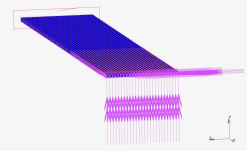
<u>ROUND</u> $\phi = 9 \text{ mm}$ , $s=5.08$ FEM Model: Axisymmetric	<u>SQUARE</u> 12.5x12.5 mm, $s=3.24$ , $t=1$ FEM MODEL: 1/8 of the specimen	<u>RECTANGULAR <math>t=2</math></u> 12.5x6.25 mm, $s=4.58$ , $t=2$ FEM MODEL: 1/8 of the specimen
		
<u>RECTANGULAR <math>t=2.65</math></u> 15.9x6 mm, $s=4.15$ , $t=2.65$ FEM MODEL: 1/8 of the specimen	<u>RECTANGULAR <math>t=5</math></u> 12.5x2.5 mm, $s=7.24$ , $t=5$ FEM MODEL: 1/8 of the specimen	<u>RECTANGULAR <math>t=20</math></u> 20x1 mm, $s=20.12$ , $t=20$ FEM MODEL: 1/8 of the specimen
		

Table 2.4 Specimens FEM Models



Nine arbitrary material curves, described in Table 2.5 and plotted in Figure 2.21, are identified by combining three necking initiation strains (early 0.03, medium 0.125 and late 0.25) with three increasing rates (low, medium and high).

Such curves are expressed by various arbitrary Ludwik functions up to the respective necking strains, as far as the uniaxiality and uniformity of smooth specimens ensure that  $\sigma_{Eq} = \sigma_{True}$ . In the post necking range, the assumption is made that  $\sigma_{True}(\epsilon_{True})$  is linear with the same slope of the Ludwik function at the necking onset, as it is typically found by experimental cross section measurements; then the Mises stress is obtained by the *MLR* postnecking correction,  $\sigma_{Eq} = \sigma_{True} \cdot MLR$ .

If the Ludwik-type functions were also extended all over the post-necking range for representing the Mises hardening, then the backward necking correction would have brought unrealistic true curves with remarkably concave or convex trends.

Indeed, either concave or convex post-necking true curves have never been found in our experiments and, in the knowledge of the author, also the true curves from the literature obtained by effective cross section measurements never show appreciable curvature beyond the necking, apart from the very late damage-induced failure propagation which, sometimes, is represented as the last short falling branch of a true curve.

	Low Hardening	Medium hardening	High hardening
Early necking ( $\epsilon_{Neck} = 0.030$ )	Mat G A=300, B=110, n=0.5	Mat B A=300, B=400, n=0.06	Mat A A=300, B=800, n=0.043
Medium necking ( $\epsilon_{Neck} = 0.125$ )	Mat F A=300, B=300, n=0.44	Mat I A=500, B=500, n=0.44	Mat H A=700, B=700, n=0.44
Late necking ( $\epsilon_{Neck} = 0.250$ )	Mat C A=300, B=400, n=0.95	Mat D A=300, B=500, n=0.6	Mat E A=500, B=833.3, n=0.6

Table 2.5 Materials characteristics

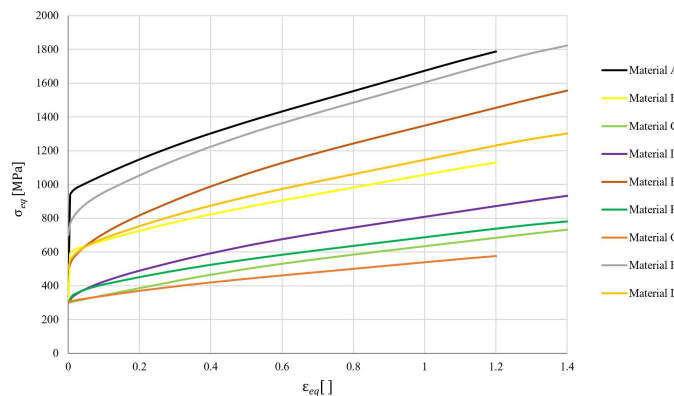


Figure 2.21 Material flow curves

All the FEM simulations are nonlinear implicit, with additive strain decomposition and updated Lagrangian formulation. The flat specimens are meshed as 3D models of 1/8 of the specimen, constrained in order to take into account the three planes of symmetry. The round specimens are modeled by axisymmetric elements. One end of each model is hold along the axial direction and the desired axial displacement is gradually imposed to the other end. The relevant data for calculating engineering curves and true curves (current values of axial force, gage length elongation and cross section area) are read at the proper nodes from the results of the FEM simulation.

### **2.3.2.3 Final Results**

The evolving true and engineering strains from all the FEM analyses are calculated from the current values of the minimum resisting cross section area and of the specimen elongation. Below, the full procedure for obtaining the MVB relationships is explained for the extreme cases of *round* and *rectangular*  $t = 20$  specimens, while the final graphs will be shown for all the considered geometries. All the plots are extended up to realistic post-necking true strains close to one.

Firstly, two variables are identified for expressing the “translated” evolution of the elongation and of the transverse area shrinking, in the sense that the specimen at the necking onset can represent some sort of “undeformed configuration” for such variables, which then only start evolving beyond the necking initiation.

The variables considered are the necking-referenced area reduction  $A/A_{Neck}$  and the necking-referenced engineering strain defined as in eq. (26).

$$\epsilon_{eng\_RefNeck} = \frac{L-L_{Neck}}{L_{Neck}} \quad (26)$$

where  $A$  is the current area of the neck section,  $A_{Neck}$  is the area of the same cross section at the necking onset,  $L$  is the current value of the elongated gage length and  $L_{Neck}$  is the value of such reference length at the necking onset.

The two above variables are read at different analysis steps from the FEM simulations and their relationship is shown in the plots of Figure 2.22.

Figure 2.22 evidences that, for materials with the same necking initiation strain, the relationship between  $A/A_{Neck}$  and  $\epsilon_{eng\_RefNeck}$  evolves independently of any other material parameter (hardening value, its slope or its curvature).

This first outcome demonstrates that the shape changes occurring in tensile specimens due to the necking phenomena are material independent for materials with the same necking strain; it also highlights once more the importance of  $\epsilon_{Neck}$ , easy to be determined, as the only material parameter still affecting the post-necking behaviour.

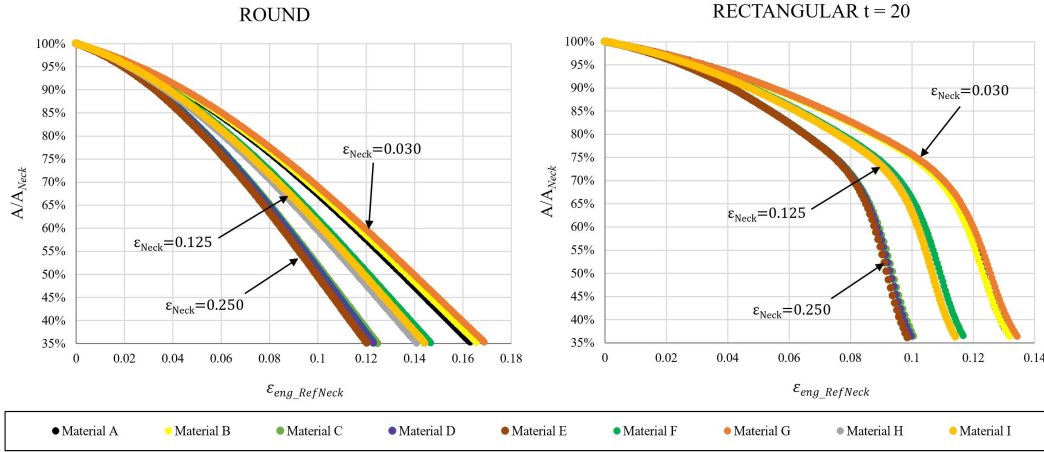


Figure 2.22 Post-necking area reduction VS engineering strain referred to the necking for round (left) and rectangular  $t = 20$  (right) specimens

Such plots also show that a function depending on  $\epsilon_{eng\_RefNeck}$  (abscissa) and on  $\epsilon_{Neck}$  (parameter) can be successfully identified as a best fit of such data for each specimen geometry.

A two-variable best fit based on data like those of Figure 2.22, eventually extended for including more materials with intermediate values of the necking strain, could deliver a surface plot capable of returning the post necking evolution of the neck section from simple elongation measurements, valid for the considered specimen shape (round, thick and thin flat) and for whatever material.

The possibility offered by the functions above, of determining the current neck area and, then, the whole true curve starting from just the elongation history, can be of significant interest for an industry-friendly approach to the material characterization.

One more attempt is made here for further simplifying the relationship between area-related variables and elongation-related variables in the post necking range.

The two variables in eqs. (27) and (28) are defined, where the first is a post-necking true strain and corresponds to the logarithm of the same function already plotted in Figure 2.22, while the second is a post-necking engineering strain conceptually very different from the abscissa of the plots in Figure 2.22, because two different reference lengths are adopted in each case.

$$\epsilon_{true} - \epsilon_{tru\_Neck} = \ln \frac{A_0}{A} - \ln \frac{A_0}{A_{Neck}} = \ln \frac{A_{Neck}}{A} \quad (27)$$

$$\epsilon_{eng} - \epsilon_{engNeck} = \frac{L-L_0}{L_0} - \frac{L_{Neck}-L_0}{L_0} = \frac{L-L_{Neck}}{L_0} \quad (28)$$

As it is possible to see in Figure 2.23, the relationship between the above variables seems to nearly remove the dependence on  $\epsilon_{Neck}$  appearing in Figure 2.22 as a

curve parameter, while leaves a certain amount of scattering between the materials groups with the same necking strain.

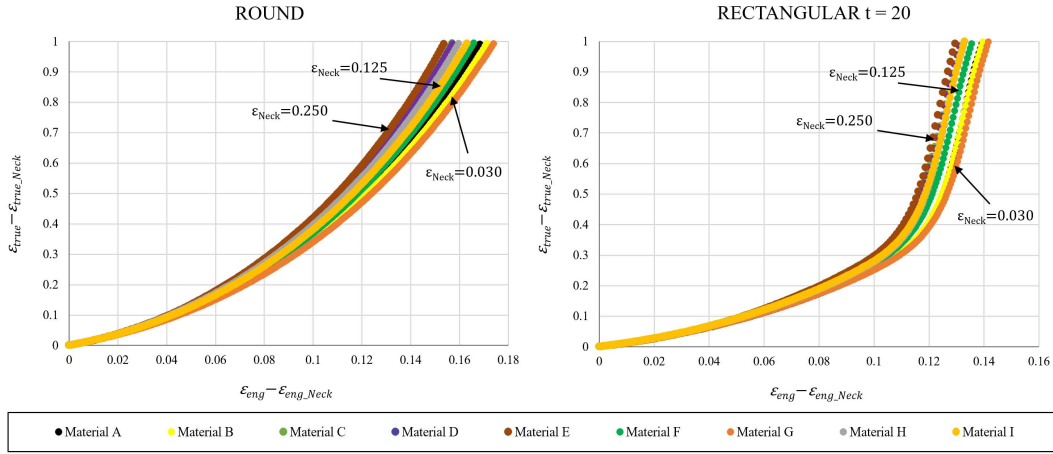


Figure 2.23 Post-necking true strain VS post-necking engineering strain for round (left) and rectangular  $t = 20$  (right) specimens

Then, one more relationship is considered between the same abscissa of Figure 2.23 and a modified post-necking variable, defined as in eq. (29) by multiplying the post-necking true strain by a power of the necking true strain.

$$\left(\varepsilon_{true} - \varepsilon_{true_{Neck}}\right) * \varepsilon_{Neck}^{-0.1} = \ln \frac{A_{Neck}}{A} * \varepsilon_{Neck}^{-0.1} \quad (29)$$

The power “- 0.1” has been found to nicely collapse all the curves for each specimen geometry into a single narrow bundle of curves with moderate scattering, as visible in Figure 2.24 where the relationship between the variables in eqs. (28) and (29) is plotted for the six considered cross section shapes.

Further investigations are necessary for understanding in more detail the meaning of the multiplying power factor in eq. (29) and for checking the possibility that other terms can also be used.

The best fit of the curves in Figure 2.24 finally delivers a single MVB function for each geometry, valid for whatever material, where the necking strain is included as an implicit variable.

The MVB functions allow to obtain the true strain from the knowledge of the engineering strain, by eq. (24), and the true stress by the knowledge of the engineering stress, by eq. (25), or, in other words, allow to derive the true curve from the engineering curve. The former curve can be finally corrected by the MLR polynomial in order to obtain the Mises curve.

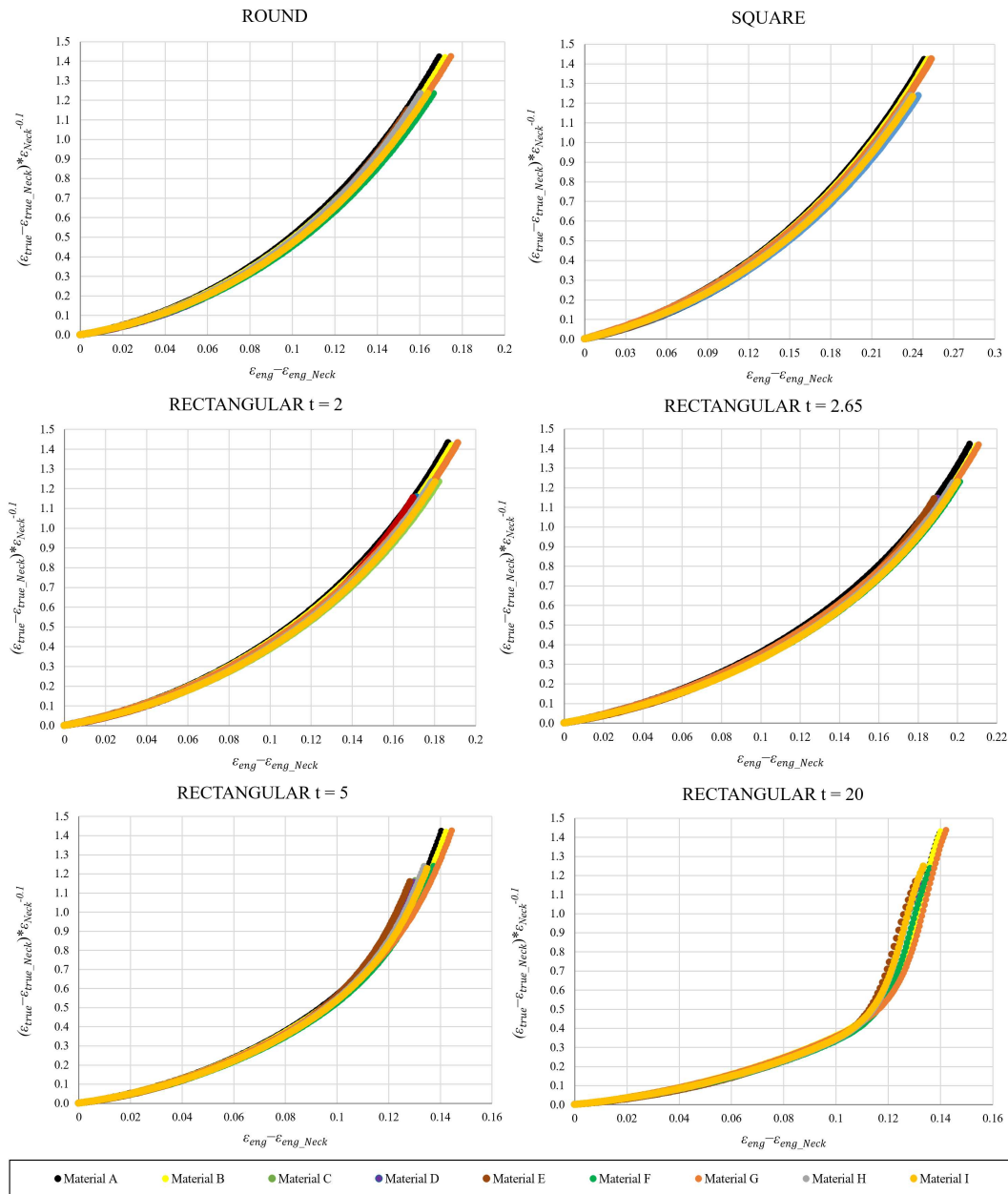


Figure 2.24 Modified post-necking true strain VS post-necking engineering strain for round (top left), square (top right), rectangular  $t = 2$  (middle left), rectangular  $t = 2.65$  (middle right), rectangular  $t = 5$  (bottom left) and rectangular  $t = 20$  (bottom right) specimens

Figure 2.24 shows that the MVB curves of thinner specimens, with higher values of the thickness ratio  $t$ , exhibit an increasing scatter near their end. This is probably due to the onset of the localized necking which tends to force a biaxial stress state and then limits the unconstrained evolution of the triaxiality induced by the diffused necking, in a way that is not captured anymore by the MVB functions.

A similar deviation was also found in Mirone and Corallo (2010b), where the MLR polynomial turned out to be appropriate for converting  $\sigma_{true}$  into  $\sigma_{Eq}$  all over the

phase of diffused necking for thin flat specimens of different materials, but stopped being accurate at the onset of localized necking.

The data in Figure 2.24, from which the MVB functions are obtained by best fitting, are referred to the specific values of the gage lengths prescribed ahead, complying with the requirements of minimum slenderness already discussed before.

Fortunately, it is possible to demonstrate that the MVB functions obtained for a certain reference gage length can be also easily applied to whatever other different slenderness-complaint gage length, by a simple change of variables.

In fact, the reference length  $L_0$  in the abscissa  $\frac{L-L_{Neck}}{L_0}$  can be updated according to the following considerations.

In Figure 2.25 is depicted the evolution of two possible gage lengths  $L^I$  and  $L^{II}$  during a tensile test on a specimen.

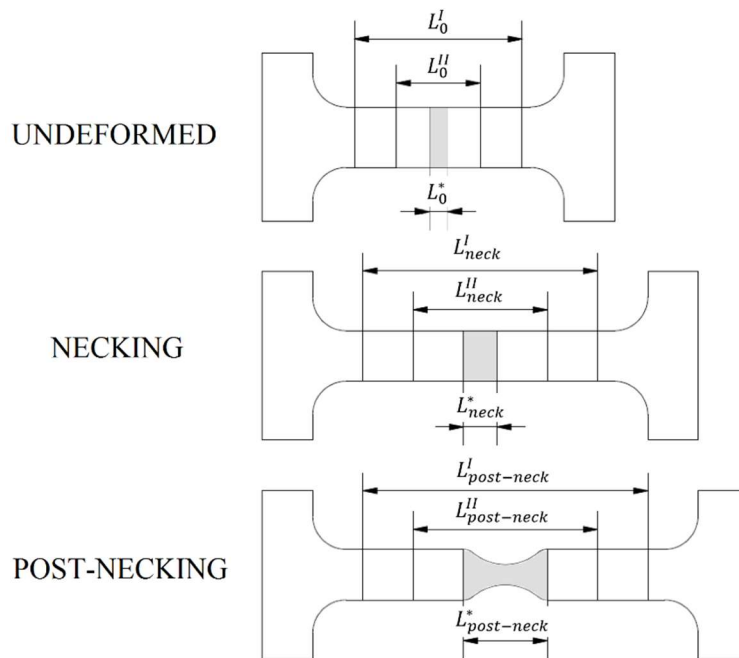


Figure 2.25 Specimen gage lengths evolution during a test

The specimen geometry ensures that the shoulders are far enough from the extremities of both gage lengths and that both such gage lengths are long enough that they fully include, during the entire test, the necking-affected segment  $L^*$ .

At the necking onset, all the gage lengths are uniformly stretched to  $L^I_{neck}$  and  $L^{II}_{neck}$  and, as the necking proceeds, the deformation will continue to develop only within  $L^*_{neck}$ , while outside such segment the deformation almost stops increasing and remains close to  $\epsilon_{trueNeck}$  up to failure.

At the necking onset, it is possible to write:

$$L_{neck}^I = L_{neck}^* + x^I \quad (30)$$

$$L_{neck}^{II} = L_{neck}^* + x^{II} \quad (31)$$

where  $x^I$  and  $x^{II}$  are the uniformly stretched parts of the specimen included within the gage length that, beyond the necking onset, will not deform anymore. Therefore, in the post-necking phase, it is possible to write the following:

$$L_{post-neck}^I = L_{post-nec}^* + x^I \quad (32)$$

$$L_{post-neck}^{II} = L_{post-neck}^* + x^{II} \quad (33)$$

Then the post-necking engineering strain based on the two different gage lengths can be expressed as:

$$\varepsilon_{eng}^I - \varepsilon_{engNeck}^I = \frac{L_{post-neck}^I - L_{neck}^I}{L_0^I} = \frac{L_{post-neck}^* + x^I - (L_{neck}^* + x^I)}{L_0^I} = \frac{L_{post-neck}^* - L_{neck}^*}{L_0^I} \quad (34)$$

$$\varepsilon_{eng}^{II} - \varepsilon_{engNeck}^{II} = \frac{L_{post-neck}^{II} - L_{neck}^{II}}{L_0^{II}} = \frac{L_{post-neck}^* + x^{II} - (L_{neck}^* + x^{II})}{L_0^{II}} = \frac{L_{post-nec}^* - L_{neck}^*}{L_0^{II}} \quad (35)$$

Such equations show that the only difference between the two post-necking engineering strains is the denominator. Then, the correspondence between the two of them is rather trivial as:

$$\varepsilon_{eng}^{II} - \varepsilon_{engNeck}^{II} = (\varepsilon_{eng}^I - \varepsilon_{engNeck}^I) * \frac{L_0^I}{L_0^{II}} \quad (36)$$

Therefore, despite the MVB functions are obtained from a certain slenderness ratio  $s$ , they can also be used for whatever other acceptable slenderness value, via the variables change in eq. (36).

### 2.3.3 Application to Experimental Data

#### 2.3.3.1 Thin Rectangular Section (20x1 mm) – Al Alloy

The first experimental validation of the MVB method is made for thin flat specimens, where DIC-assisted tensile tests have been carried out for determining the experimental true curve of an aluminium alloy provided by Hydro Aluminium and identified as 185D, previously investigated by Mirone and Corallo (2010b) and,

obviously, not included in the set of nine arbitrary materials discussed before. A 20x1 mm cross section is adopted, according to Figure 2.26.

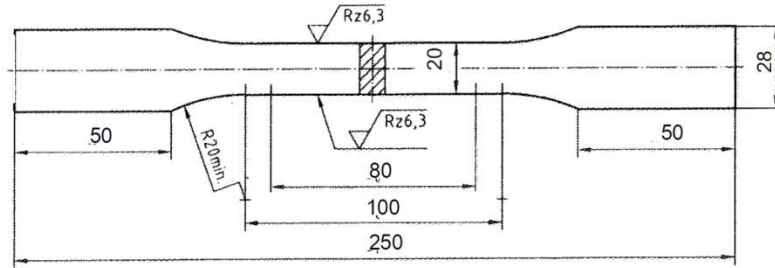


Figure 2.26 Alloy 185 specimen geometry

Full-field DIC data allowed to obtain the experimental  $\epsilon_{eng}$  averaged over a 50 mm gage length, together with three approximations of  $\epsilon_{true}$  at different global-local scales; such approximations respectively correspond to  $\epsilon_{true}$  averaged over the above 50 mm axially long specimen segment for the more global estimate,  $\epsilon_{true}$  averaged over a thin transverse rectangle enclosing the diffused neck section for the intermediate level, and  $\epsilon_{true}$  averaged over small areas of about 2 mm<sup>2</sup> at the intersection between the transverse diffused neck and the 55 degrees localized neck, for the most local estimate at latest test stages (Figure 2.27).

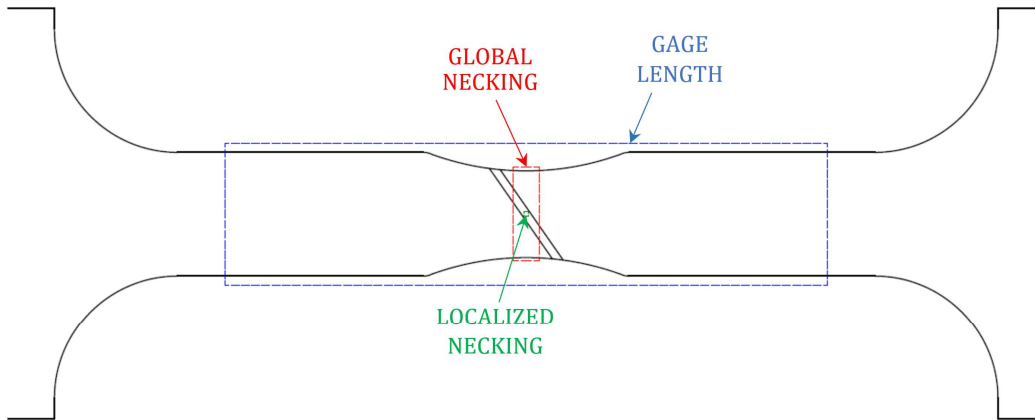


Figure 2.27 Scheme of the global/intermediate/local DIC acquisition scales

Each  $\epsilon_{true}$  measurement provided the corresponding conversion of the engineering stress into a DIC-based true stress, by eq. (37).

$$\sigma_{true} = \sigma_{eng} * \frac{A_0}{A} = \sigma_{eng} * e^{\epsilon_{true}} \quad (37)$$



All the experimental stress-strain curves are shown in Figure 2.28 and represent four different approximation levels of the experimental material curve, from the less to the most accurate.

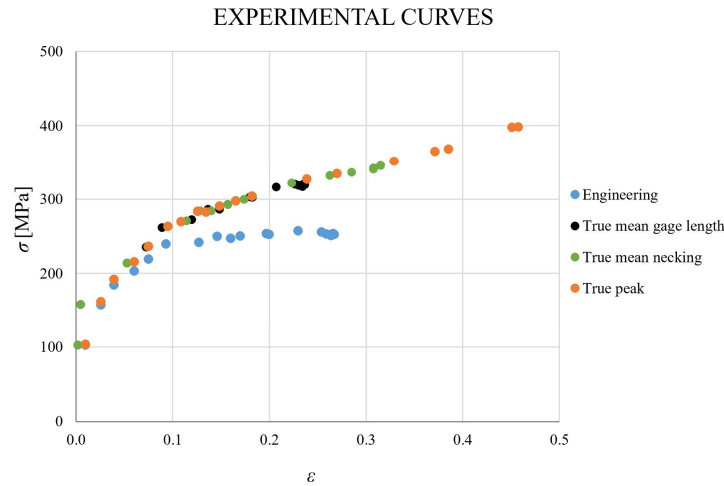


Figure 2.28 Experimental data for specimens of Al alloy with  $t=20$

The engineering curve is of no real help unless a MVB-like direct method for the material characterization is available; so far, it can only be used for FEM-based reverse engineering characterization.

The different DIC approximations of the experimental true curve are nicely overlap and, obviously, they also are as shorter as the more “global” is the strain measurement from which they are derived, because global measurements always include also specimen zones where the strain remains almost frozen at the necking onset.

The global true curve referred to the gage length suggests a fracture strain of about 0.22, the intermediate curve referred to the diffused neck section stops at a strain of 0.33 and the local peak-based true curve accounting for the localized neck fails at a strain of about 0.46.

The MVB polynomial and the MLR correction have been then applied to the engineering curve in order to obtain the equivalent material curve. The equivalent Mises curve so obtained has been used for driving the FEM simulation of the test; finally, the engineering curves and the true curves have been extracted from the deforming mesh in the FEM results and have been compared to the experimental ones in Figure 2.29.

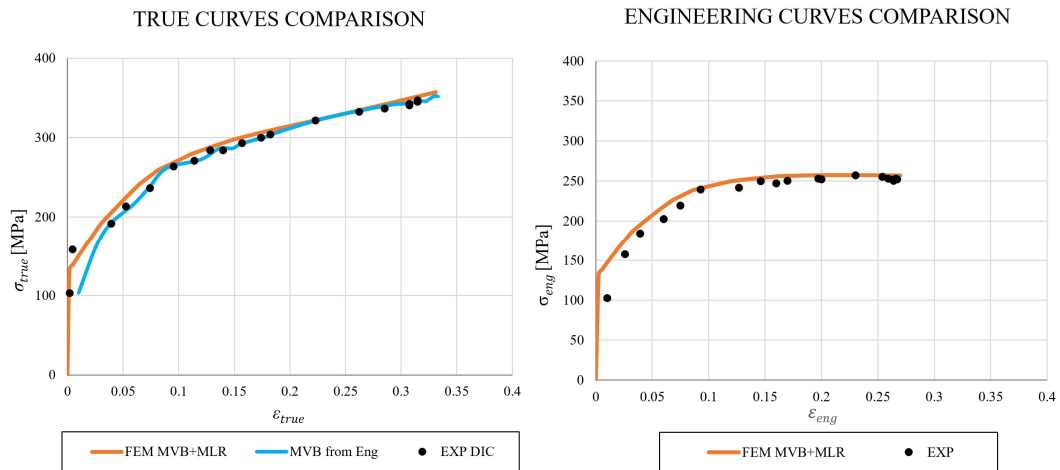


Figure 2.29 Comparison between the true curves by DIC, MVB and FEM (left); comparison between the engineering curves by experiments and by FEM (right): material modelled via experimental engineering curve processed by the MVB and by the MLR correction.

The left side of Figure 2.29 reports the comparison between the true curves obtained by DIC at the intermediate scale of the diffused neck, those obtained by the MVB functions and those derived from the output of finite elements.

It is worth noting that the good matching of the first two curves above conveys a very direct evidence, as it demonstrates that the experimental true curve can be successfully obtained by simply applying the MVB criteria to the experimental engineering curve, without the need of any numerical analysis nor any other mathematical/numerical tool.

Instead the agreement of the third FEM-predicted true curve to the previous two delivers a second-approximation evidence, demonstrating that the combination of the MVB functions and the MLR correction together deliver an accurate post-necking Mises curve which, in turn, accurately drives the FEM simulation of the test.

The right side of Figure 2.29 shows the comparison between the engineering curves obtained by experiments with those from the FEM simulation. This FEM vs. experimental comparison again validates the combination of MVB and MLR in delivering the accurate hardening function and, in turn, accurate FEM results, just starting from the experimental engineering curve.

The true strain at failure, estimated by the MVB function and by the engineering strain, also complies to the experimental true strain at failure of about 0.33 obtained from DIC measurements over the diffused neck. This further confirms that the MVB functions are capable of correctly relating the elongation-based curves to the cross section-based ones up to the diffused neck, while are not capable of taking into account for the high stress-strain gradients typical of the localized necking of thin sheets.

### 2.3.3.2 Round Section ( $d = 6.25 \text{ mm}$ ) – Carbon Steel

The second experimental validation of the MVB method is provided now for cylindrical specimens and, in particular, considering the experimental data from Joun et al (2008), concerning tensile tests on SWCH10A steel cylindrical specimens with diameter of 6.25 mm and gage length of 25 mm (Figure 2.30).

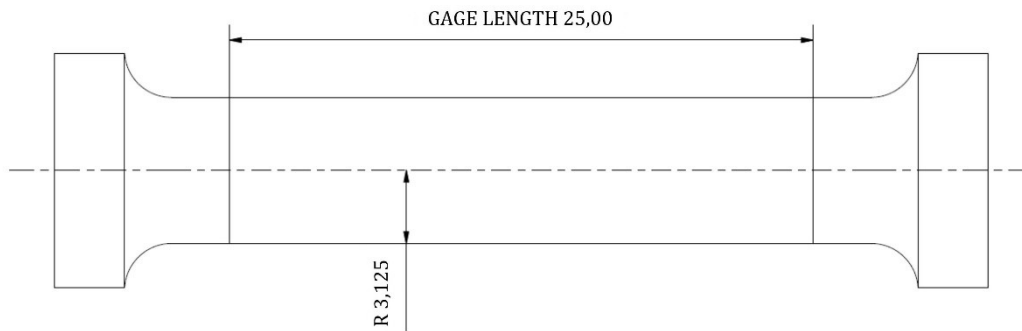


Figure 2.30 Scheme of the Joun specimen

The authors only provide the experimental engineering curve, with a strain at necking initiation of 0.145, corresponding to a true strain of 0.135. The MVB method applied to the engineering curve and to such necking initiation strain delivered the true curve of the material. This last curve has been then corrected by the MLR function in order to obtain the Mises curve. The true and the Mises curve are plotted together in Figure 2.31.

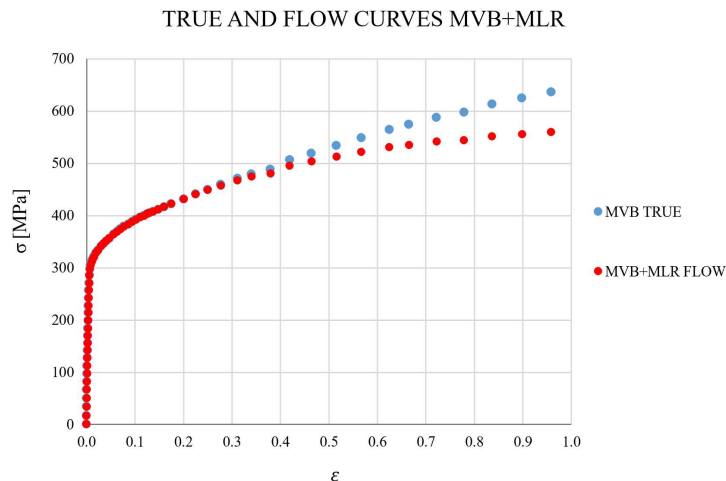


Figure 2.31 True and flow curves obtained with MVB and MLR

The equivalent Mises curve so obtained, named “Flow MVB+MLR” in the following plots, is used for driving the FEM simulation of the test.

Another FEM simulation is also ran, for comparison purposes, with a Mises curve estimated by a more classical approach frequently adopted in the literature, consisting of the elongation-based true curve from eq. (17) and eq. (18) up to the necking onset, prolonged by a linear segment with slope continuity from the necking onset up to failure. Such Mises curve and the related FEM results are afterwards named as “Flow Line”.

The engineering curves predicted by the two FEM runs are then calculated from load and displacements read on the deforming mesh, and are compared each other in Figure 2.32, together with the engineering curve from experiments.

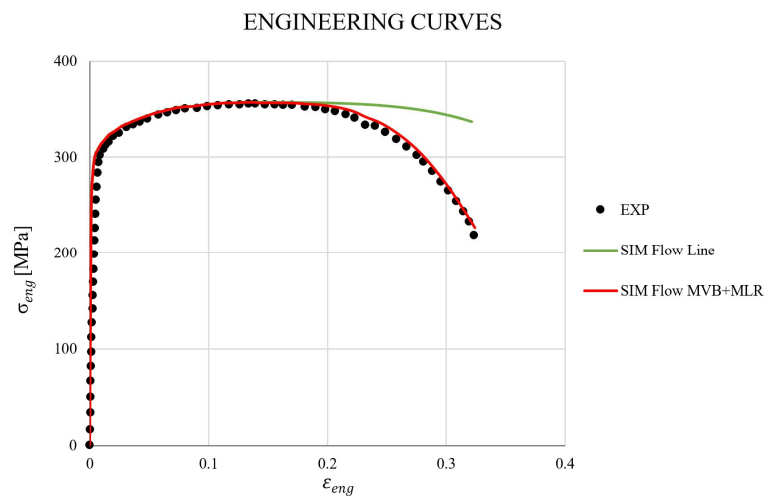


Figure 2.32 Comparison between the experimental, simulation MVB+MLR and simulation Flow Line engineering curves

Joun et al (2008) did not provide the experimental true curve, so only the engineering curves in Figure 2.32 can provide an indirect validation of the MVB method.

Figure 2.32 shows that the FEM results driven by the material curve “Flow MVB+MLR” reproduce the experimental response with very good accuracy, while the FEM results obtained with the “Flow Line” material curve largely deviate from the experiments just after the necking onset.

Such comparison confirms once more the effectiveness of the MVB method.

### 2.3.3.3 Thick Rectangular Section (15.9 x 6 mm) – Mild Steel

A final validation of the MVB method is reported for thick flat specimens; in this case, the experimental determination of the postnecking true curve is much more difficult than it is for round and thin flat specimens, because 3D stereoscopic measurements are essential for capturing the shrinkage of a thick cross section.

A camera-assisted experimental tensile test has been carried out on a steel rectangular 15.9x6 mm specimen with a gage length of 31.9 mm. The outcome of the test is the engineering curve and the true necking strain of about 0.37.

The experimental true curve is not available for this test due to the lack of 3D-DIC, then, the validation of the MVB method by such experiment is only possible by checking the accuracy of the test simulated by FEM where the input Mises curve of the material is based on the MVB functions.

Therefore, the MVB method is applied to the experimental engineering curve, returning the true curve of the material. The true curve is then corrected by the MLR function in the post necking range, for obtaining the Mises curve. Both latter curves are plotted in Figure 2.33.

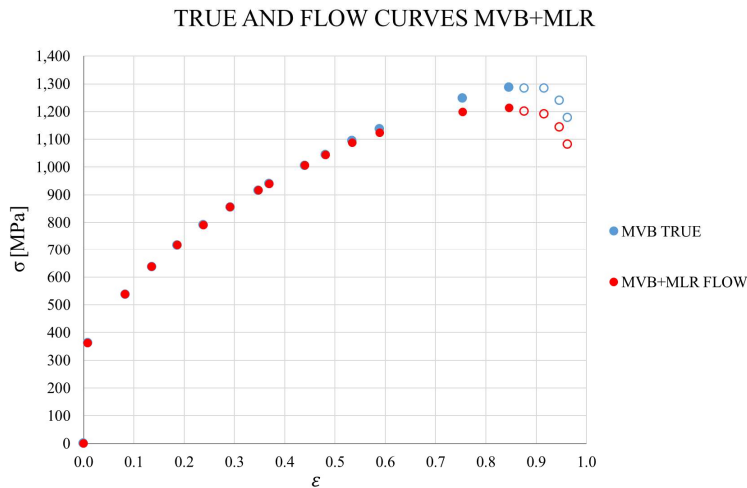


Figure 2.33 True and flow curves obtained with MVB and MLR

The true curve, obtained by processing the experimental engineering curve through the proper MVB function, exhibits a remarkable curvature and a descending branch at its late stages. This is probably due to internal fracture initiation within the neck section, which does not appear outside in the camera images but influences both the elongation increase and the load drop.

Considering such descending part in the true curve and in the corresponding flow curve, means to incorporate a damage phenomenon in the material curve considering that the FEM simulations done in this thesis work do not incorporate a damage model but only a plasticity model. This is obviously an incorrect approach but it is useful in the following.

To evaluate the influence of this aspect, two simulations of the test have been made, one with the complete flow curve (full and empty red dots in Figure 2.33 and depicted afterwards as “Flow MVB+MLR Comp”) and the other with an interrupted flow curve (only full red dots in Figure 2.33 and depicted afterwards as “Flow MVB+MLR Int”). Moreover, to assess the improvement in the characterization process of the MVB method compared with the classical approach, a third simulation has been made also in this case with a material flow curve obtained from the engineering curve until the necking onset with eq. (17) and eq. (18) and completing it with a line tangent to the curve in such point (depicted afterwards as

“Flow Line”). Then, the engineering curves have been extracted from the deforming mesh in the FEM results of the simulations and have been compared to the experimental one as it can be seen in Figure 2.34.

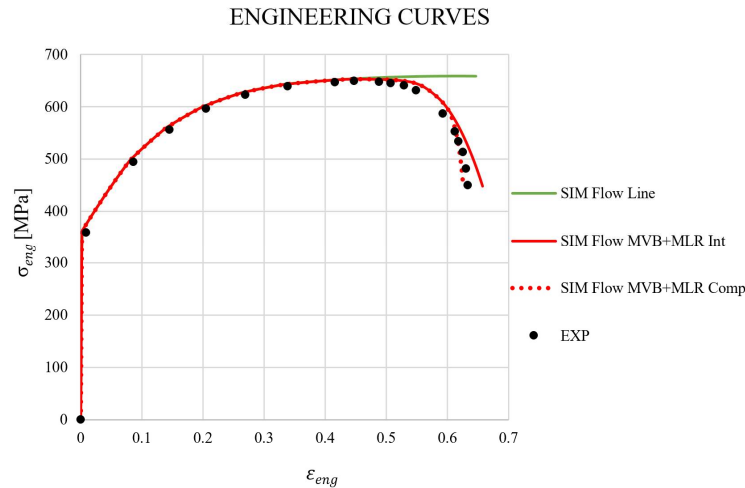


Figure 2.34 Comparison between the experimental, simulation MVB+MLR Interrupted, simulation MVB+MLR Complete and simulation Flow Line engineering curves

In such figure, it is possible to see how the best simulation is the one with the complete flow curve, which incorporates the damage process, while the simulation with the interrupted flow curve overestimate the final part of the experimental engineering curve. However, both simulations are much more accurate than the one with the flow curve obtained with the classical approach. The most correct approach would be to use the interrupted flow curve coupled with a damage model. It is important to underline that, in cases like this with thick rectangular specimens, there is no other technique to obtain the true curve and the MVB method proved to be very accurate, incorporating also the damage phenomenon occurring during the test, despite the incorrectness of the approach.

## 2.4 Static Characterization and Modelling Summary

In this Chapter, two aspects of the static characterization and modelling of metals were discussed: a new yield model and a new experimental characterization procedure. The proposed yield criteria is based on the experimental evidence that many structural metals exhibit different hardening functions when the plastic deformation occurs under differently evolving Lode angles. The shown yield surface is initially based on a blend of the von Mises surface to a Tresca-like one, with dodecagonal straight-edged cross section. Such yield function, X-dependent through the calibrating term  $m$  which expresses the relationship between the hardenings in pure shear and in pure tension, is further amplified by a quadratic function of the Lode angle calibrated through the material constant  $qa$ . Eventually,

a similar dependence on the hydrostatic stress can be added for including the effect of the stress triaxiality, if the material response requires it. Experimental data by Allahverdizadeh et al. (2014) on Ti6Al4V are used for calibrating the model and for checking its suitability to reproduce the behavior of such alloy undergoing various plastic straining histories, occurring under different stress paths and Lode angle ranges. The experimental variability of the Lode angle is provided through assorted mixes of tension-torsion, pure tension and pure torsion, as well as by pulling tests of flat plane strain and shear butterfly-like specimens. The calibrated model allows to reproduce all the experiments with good accuracy, leaving almost unaltered the already good accuracy shown by the classical Mises plasticity for the tests where the stress states evolve closer to uniaxiality, while almost completely fixing the substantial error which the same Mises plasticity introduces when the simulated tests involve variable Lode angles departing from uniaxiality. Further experiments, generating constant Lode angles and scanning the 0-30 degrees range in finer intervals, might be useful for better assessing the sensitivity of the yield to Lode angle variations. Although the elastoplastic response of the Ti6Al4V alloy is accurately modeled by the proposed yield function, other materials should be modeled for checking the model generality, eventually including an upgrade of the yield model currently in progress, which incorporates a strain-dependent quadratic amplification parameter  $qa((\varepsilon_{EQ}))$ .

As it was already highlighted, a yield model must be calibrated and to do that it is necessary to characterize the behaviour of the material under different stress states. In this Chapter, a new procedure for a simple quick tensile stress-strain characterization of metals was also proposed. It is based on the evidence that, if the right variables are identified for describing the necking evolution, in a tensile test necking shows its nature of geometric, material-independent phenomenon, only governed by the post-necking true strain. A set of nine arbitrary materials, encompassing very different combinations of early/medium/late necking strain and low/medium/high hardening slopes, is defined for simulating different tensile tests by FEM, referring to round, square and rectangular specimens with several different width-to-thickness ratios. All the material hardenings are based on the assumption that the pre-necking Mises curves can be described by arbitrary Ludwik functions, while the post-necking Mises curves are derived by the MLR triaxiality correction applied to linear segments of the true curves ensuring slope continuity at the necking onset. The relationships between elongation-based variables and area-based variables is analysed in the post-necking range by FEM, leading to material-independent functions of the post-necking strains, called MVB, able to convert the engineering curves into the true curves, for each considered specimen cross section and for virtually whatever material. Such finding is of significant interest for research and industrial applications since, by means of the proposed MVB converting functions, it is possible to obtain the true curves from simple engineering

elongation-based measurements, without the need of time-consuming optical measurements or 2D and 3D DIC techniques needed for the fully-experimental true approach. The experimental validation of the proposed method, provided for round, thick flat and thin flat specimens made of different materials demonstrated that the MVB functions are suitable for determining the very useful area-based experimental true curves, rather complicate to be obtained by experiments, from just the elongation-based and poorly meaningful engineering curves, much simpler to be obtained by experiments. Such large simplification of the experimental procedures is accomplished while maintaining a very good degree of accuracy. This makes the MVB functions a potentially desirable tool for those routinely involved in material characterization activities, especially in the industry where expensive equipment and time-consuming procedures carried out by highly specialized personnel are more critical.





# 3 Dynamic Characterization and Modelling of Metals

## 3.1 Overview

This chapter is aimed at the quantitative evaluation of the error levels in the dynamic characterization of ductile metals via Hopkinson bar tensile tests, ran according to the classical strain-gauge-based experimental procedure and to the enhanced high-speed-camera-assisted procedure. In such evaluation, the effect of the specimen slenderness is also investigated for checking the sensitivity of both the above techniques to different specimen geometries. Moreover, an experimental campaign on a sintered Electron Beam Ti6Al4V alloy, partially already shown in Chapter 2.2.1, and the results of an experimental campaign on a mild steel named FEN steel, will be discussed to investigate the freezing of the strain rate effect induced by the necking onset. For each SHTB test, the ratio of the dynamic true stress to the static true stress is calculated at fixed strain intervals and is associated to the current value of the evolving true strain rate; the resulting trends of the dynamic amplification are approximated by different tentative functions expressing the strain rate sensitivity of the material. Concerning the FEN Steel campaign, two “extreme” experiments, representative of the entire set of trails, are then simulated by FE adopting all the tentative strain rate functions: the FE outcome compared to the experimental results delivers enough information for proving that an important relationship exists between the necking and the strain rate effect. A discussion is finally provided about the limits, arising from the above interaction, to the effective testability of metals at high strain rates via SHTB equipment.

## 3.2 Experimental Issues in Tensile Hopkinson Bar Testing

### 3.2.1 Specimen Geometry, Necking and Engineering vs. True Curves Approximations

The classical equations used in SHTB experiments for the stress / strain / strain rate characterization of materials are based on the elastic strain waves measured along the bars (incident  $\varepsilon_i$ , reflected  $\varepsilon_r$ , transmitted strain waves  $\varepsilon_t$ ):

$$\dot{\varepsilon}_{Eng}(t) = 2 \cdot \frac{c_0}{L_0} \cdot \varepsilon_r(t) \quad (38)$$

$$\varepsilon_{Eng}(t) = -2 \cdot \frac{c_0}{L_0} \cdot \int_0^t \varepsilon_r(t) \cdot dt \quad (39)$$

$$\sigma_{Eng}(t) = \frac{E_{bar} \cdot A_{bar}}{A_{0-sp}} \cdot \varepsilon_i(t) \quad (40)$$

with  $c_0$ ,  $E$ ,  $A_{bar}$  the nominal sound speed, the elastic modulus and the cross section of the bars, and  $L_0$ ,  $A_{0-sp}$  the gauge length and the cross section of the round smooth undeformed specimen, respectively.

Eq. (38) expresses the time derivative of the total specimen length  $L_{tot}$ , including the length of shoulders and fillets always present in tension samples. If the ratio  $L_0 / A_{Sp}$  is significant (slender, “long” specimens), then the elongation of the specimen shoulders is much smaller than that of the gauge length and the former can be neglected: only in this case eq. (38) gives a good approximation of the engineering strain.

On the contrary, if the ratio  $L_0 / A_{Sp}$  is rather small (stub, “short” specimens), then the elongation of shoulders and fillets is comparable to that of the gage length and cannot be neglected, so eq. (38) gives a poor approximation of the engineering strain, as qualitatively illustrated in the scheme of

Figure 3.1.

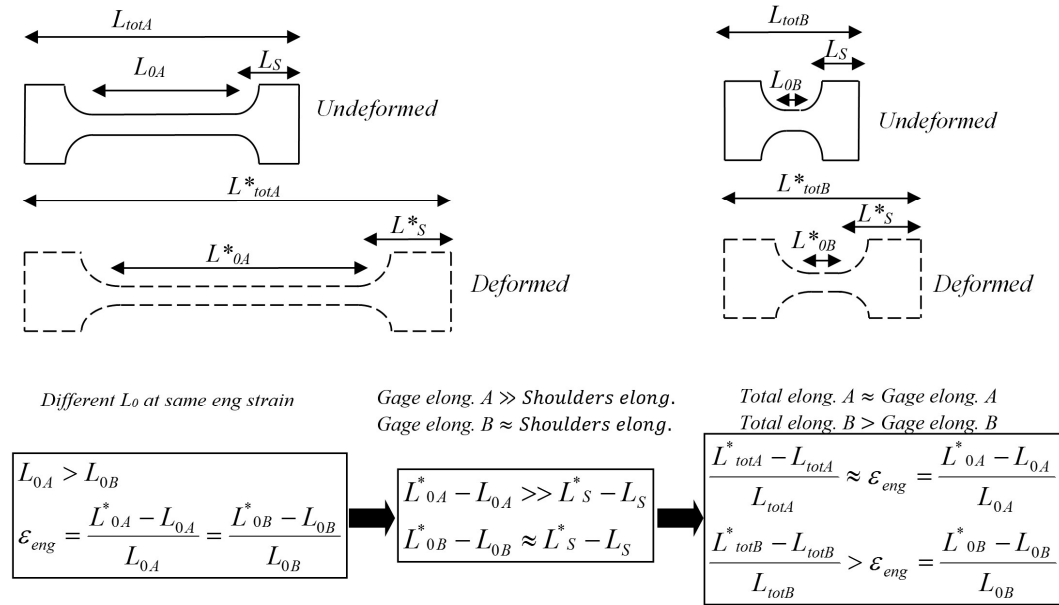


Figure 3.1 Effect of shoulders elongation on two different gage lengths subjected to the same  $\epsilon_{eng}$

Then short specimens, useful for increasing the achievable strain rate of SHTB tests, should only be adopted when high-speed camera images are available, so that strain evaluations based on the effective gage length elongation from image analyses are used instead of eqs. (38) and (39).

Another issue, affecting the dynamic tensile tests more than the static ones, is the necking-induced perturbation of the strain uniformity which always affects a finite volume of the specimen, roughly extending 2-3 times the undeformed diameter

along the specimens axis; in fact, such segment elongates many times more than the eventually remaining segments of the gage length.

The scheme of Figure 3.2 depicts that, for whatever necking-affected segment LN of a specimen with a given common “true” strain  $\text{Log}(A_{Sp-0}/A_{Neck})$  really deforming the material, the longer is the total gage length  $L_0$ , the smaller is the weight of the necking-elongated segment over the total gage length, the smaller is the nominal “engineering” strain  $\Delta L_0/L_0$ .

This implies that shorter specimens exhibit much larger engineering strains than longer ones, while this difference is only apparent as local measurements of the more pertinent true-strain  $\varepsilon_{True}$ , based on the initial and on the current specimen cross section, would deliver identical true strains:

$$\varepsilon_{True}(t) = \text{Log} \frac{A_{0-Neck}}{A_{Neck}} \quad (41)$$

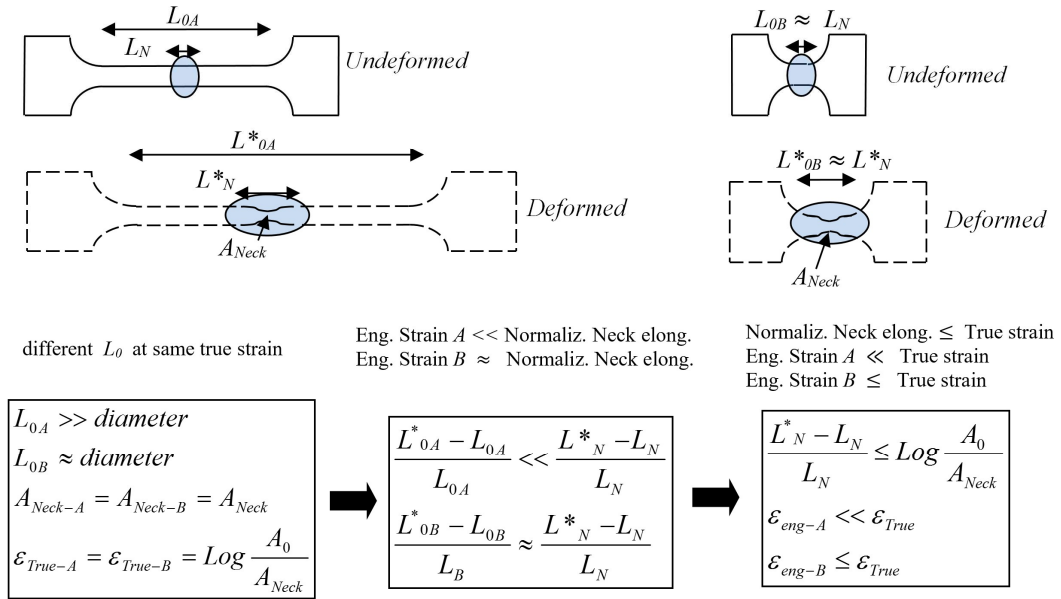


Figure 3.2 Effect of the same post-necking strain on two different gage lengths

Similar necking-induced uniformity issues also apply to the stress distributions, which may also undergo large, necking-induced deviations from uniaxiality.

This specific subject has already been extensively covered for the static case (Mirone, 2004a,b; Sato et al., 2015; García-Garino et al., 2006; Erice et al., 2012), and some results have been recently presented for extending such concepts also to the dynamic SHTB testing (Mirone, 2013; Erice et al., 2010; Mirone et al., 2016a). Two main points affect the stress evaluation. The first point is the variability of the resisting cross section of the deforming specimens during the test, which can be

easily sorted out by fast video capture of the evolving neck section during the experiments and by successive image analysis for determining the current resisting area of the specimen, so that the “true” stress  $\sigma_{True}$  of eq. (42), based on the latter area, is adopted instead of the “engineering” one of eq. (40) based on the initial specimen cross section :

$$\sigma_{True}(t) = \frac{E_{bar} \cdot A_{bar}}{A_{Sp}} \cdot \varepsilon_t(t) \quad (42)$$

The second point affecting the evaluation of the hardening stress (also called flow stress or equivalent stress below) is that the “true” stress  $\sigma_{True}$  of eq. (42) correctly describes the equivalent stress  $\sigma_{Eq}$  only up to the inception of necking, after which the increasing stress triaxiality causes  $\sigma_{True}$  to considerably deviate from  $\sigma_{Eq}$ , the latter alone constituting the real target of the material characterization. The issue is that  $\sigma_{True}$  can be easily measured while  $\sigma_{Eq}$  cannot.

So, the ratio  $\sigma_{Eq} / \sigma_{True}$  for smooth tensile bars remains equal to 1 until the necking onset, and evolves by continuously decreasing below 1 as the plastic strain flows beyond necking, until fracture occurs. For the static straining of ductile metals with failure strains within 1.5, it has been shown that such a ratio has always evolved in the range 1 - 0.75 all over the post-necking strain range:

$$\begin{aligned} \sigma_{Eq}(t) &< \sigma_{True}(t) \\ 0.75 &< \frac{\sigma_{Eq}(t)}{\sigma_{True}(t)} < 1 \end{aligned} \quad (43)$$

In Mirone (2004a) the above ratio was found to be a material-independent function of the difference  $\varepsilon_{True} - \varepsilon_N$ , between the current true strain and the Considère strain (which, of course, is material-dependent), at which necking initiates. The MLR polynomial proposed in that paper approximates such a function within an error less than 5%, and then constitutes an engineering-approximate tool for the necking correction of static true curves, which also resulted suitable for correcting dynamic true curves from SHTB as in Mirone (2013) and Verleysen (2016).

A detailed identification of the different possible strain formulations is now necessary, before proceeding to discussing the experiments.

The Engineering strain of smooth tensile specimens is defined as the current elongation normalized onto the initial gage length of the specimen:

$$\varepsilon_{Eng} = \frac{L - L_0}{L_0} \quad (44)$$

As already discussed, eq. (39) only provides an approximation of (44), because it is based on the elongation of the entire specimen including shoulders and fillets, rather

than the elongation of the gage length alone; for longer specimens, eq. (39) approximates (44) better than it does for shorter ones.

An error-free evaluation of the engineering strain (44) can be achieved by image analysis of high speed camera frames providing the elongation of the desired segment of the specimen.

Given that the engineering strain from the classical Hopkinson bar procedure is based on eq. (39), in the next sections it is also called “nominal strain” and the corresponding time rate is identified as the “nominal strain rate”.

Well known considerations about large displacements and finite deformation allow to use a first simple logarithmic expression of the true strain directly obtained from the engineering strain, identified here as the “elongation-based true strain”:

$$\varepsilon_{True\_Elong} = Ln(1 + \varepsilon_{Eng}) \quad (45)$$

The expression (45) improves the accuracy of the strain evaluation with respect to (39) and (44), but it is only valid until necking inception; after necking eq. (45) quickly underestimates the real “effective true strain” or more simply “true strain”  $\varepsilon_{True}$ , which can only be addressed according to eq. (46);

$$\varepsilon_{True} = 2 \cdot Ln \frac{d_0}{d} \quad (46)$$

for calculating the effective true strain of round specimens, measurements of the current neck diameter  $d$  from high speed camera image analysis are then mandatory. Indeed, from a mathematical viewpoint  $\varepsilon_{True}$  is the section-averaged value of the current distribution of axial strain over the neck, while, at the scale of the single material point and of the single integration point in a FEM (Finite Elements Model), the equivalent plastic strain is identified as the “local strain”  $\varepsilon_{Loc}$  and it may slightly differ from  $\varepsilon_{True}$ .

However, for round smooth metallic specimens, the axisymmetric distributions of strain along the neck radius remain rather flat also under well developed necking conditions, so  $\varepsilon_{True} \approx \varepsilon_{Loc}$  and the true strain (easily measurable) is a very reasonable approximation (within 5% underestimation) of the local equivalent plastic strain at the centre point of the neck section (impossible to be measured).

In the next sections are presented the results of SHTB experiments on an aluminium alloy and on a mild steel, providing a fully experimental evidence of the concepts discussed above with regard to the “engineering” length-related and the “true” necking-related characterization issues. The experiments on the mild steel are also enhanced by high speed camera image acquisitions, providing quantitative estimations of how much the different formulations of stress-strain curves are approximated.

### 3.2.2 Specimen Shape Effect and Engineering vs. True Approach in SHTB Experiments

Tensile tests are ran on round cross section specimens machined from a smooth bar of Aluminium 2011 (identified as *AL*) and from a threaded bar of mild steel FE370 (named *FEN*), according to Figure 3.3 and Table 3.1 where the Nominal Engineering strain rate is the maximum values from eq. (38) at incipient failure.

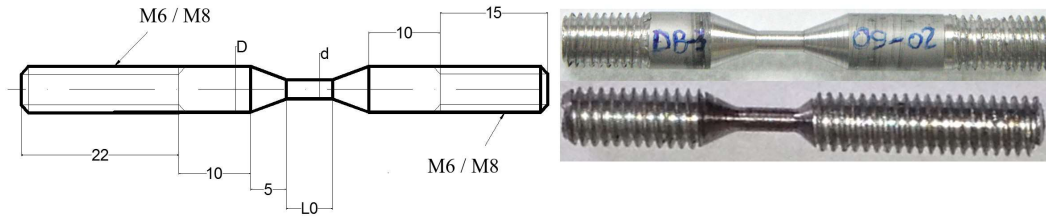


Figure 3.3 : Specimens shape for multi-length, conventional SHTB tests

Material	Nominal $L/d$ ratio	Test name	$d$ [mm]	$L_0$ [mm]	Input bar Preload [KN]	Nominal Eng SR [ $s^{-1}$ ]
Aluminium 2011	$L/d \approx 1$	AL-03-03-01	2.9	3.1	32	3600
		AL-03-03-02 bis	2.9	3.2	15	1500
		AL-03-03-03	3.1	3.1	15	1400
		AL-03-03-04	3.0	3.2	15	1400
		AL-03-03-04 bis	3.0	3.1	60	6500
		AL-03-03-05 bis	3.1	3.5	68	7000
		AL-03-03-05 ter	3.0	3.7	16	1300
		AL-03-03-06	3.0	3.2	44	5000
		AL-03-03-06 bis	2.8	3.0	40	4500
		AL-S20-01	2.5	2.5	12	2500
	AL-S20-06	2.4	3.0	12	2500	
	AL-03-03-Y-1	3.0	3.3	0	STATIC	
	AL-03-03-ST-1	3.0	3.0	0	STATIC	
	AL-S20-02	2.6	2.4	0	STATIC	
	AL-S20-05	2.5	2.8	0	STATIC	
	$L/d \approx 3$	AL-03-09-01	3.0	8.4	66	2500
		AL-03-09-02	3.0	7.9	66	3000
		AL-03-09-03	2.9	9.0	80	3000
		AL-03-09-04	3.0	8.7	42	1500
		AL-03-09-05	2.8	8.9	32	1200
AL-03-09-06		2.9	8.9	16	500	
AL-S20-09		2.5	6.6	12	1000	

		AL-S20-10	2.5	5.8	12	1100	
		AL-03-09-Y-3	3.0	9.2	0	STATIC	
		AL-03-09-Y-7	3.0	8.9	0	STATIC	
		AL-S20-07	2.5	6.2	0	STATIC	
		AL-S20-08	2.5	6.5	0	STATIC	
	<b>L/d ≈ 4</b>	AL-S20-11	2.5	9.7	12	700	
		AL-S20-12	2.5	9.7	12	700	
		AL-S20-13	2.4	9.5	0	STATIC	
		AL-S20-14	2.2	9.1	0	STATIC	
	<b>FE370</b>	<b>L/d ≈ 1</b>	FEN-D-S-11	2.9	3.0	15	750
			FEN-D-S-12	3.0	3.5	18	1100
		<b>L/d ≈ 2.5</b>	FEN-D-S-01	3.2	7.0	52	2800
			FEN-D-S-02	3.1	7.6	50	2400
			FEN-D-S-03	3.1	7.4	35	1600
FEN-D-S-04			3.1	7.5	38	1800	
FEN-D-S-05			2.6	7.4	20	700	
FEN-D-S-06			2.8	7.5	20	700	
FEN-D-S-07			2.9	6.7	67	3600	
FEN-D-S-08			2.9	6.7	71	3700	
FEN-S-S-01			3.1	7.9	0	STATIC	
FEN-S-S-02			3.1	7.6	0	STATIC	
FEN-S-S-03		3.1	8.1	0	STATIC		
FEN-S-S-04		3.0	8.2	0	STATIC		
<b>L/d ≈ 5</b>	FEN-D-S-09	3.0	14.7	34	350		
	FEN-D-S-10	3.1	15.0	28	450		

Table 3.1 Specimens data for SHTB tests

For quasistatic tests, a 100 kN motor driven testing machine was used, while the dynamic tests were ran on a direct-tension split Hopkinson tension bar (SHTB) consisting of two 16 mm diameter bars of Al 7075 alloy, 3 m long the output bar, 4.5 m the input bar.

A preload up to 100 kN can be imposed to the initial 1.5 m segment of the input bar, where a first couple of strain gauges is placed at opposite positions of its mid-length cross section, for bending-corrected load measurement. Two other couples of opposite strain gauges are placed at the mid-length sections of the remaining 3 metres segment of the input bar, and at the mid-length cross section of the output bar, respectively.

The preload is released by fracturing a fragile sacrificial element which maintains closed a two-jaws gripping mechanism. A rise of about 100  $\mu$ s is achieved. Signals



processing and acquisition is done by a 250 kHz, 8 bridges, Dewetron strain gauge station and by a National Instruments PCI 6133, 3 MHz digitizing / sampling board. Figure 3.4 shows a picture of the SHTB system.



Figure 3.4: SHTB setup

Tests at different strain rates have been carried out either by imposing different incident waves on identical specimens, and also by imposing the same incident wave to similar specimens of the same material, where only the gage length is varied. In this way, the interacting effects of the elongation rate and of the specimen shape are investigated.

This first series of standard tests on AL was run according to the classical SHTB theory because speed-camera equipment was not yet available so, for this metal, only the engineering stress, strain and strain rates are evaluated from strain gauge readings, according to eqs. (38, 39, 40).

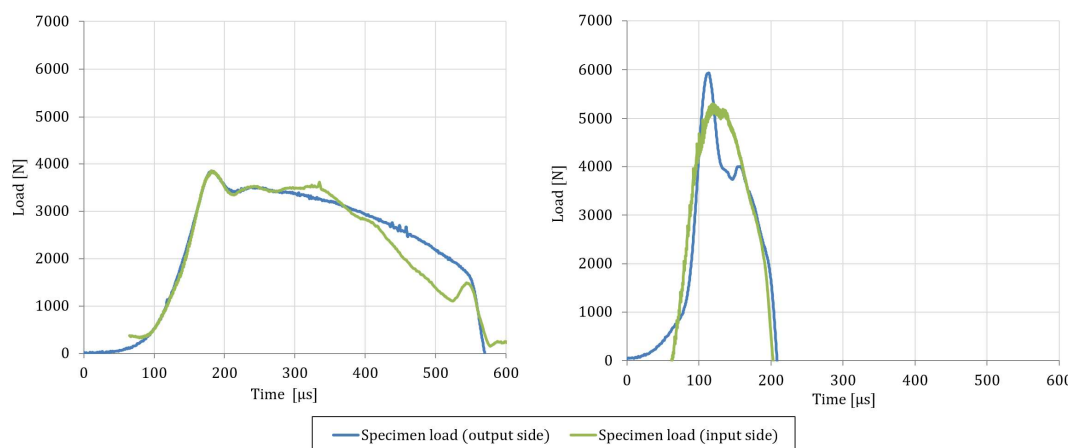


Figure 3.5: Equilibrium check for slower long specimens (left) and faster short specimens (right) dynamic tests

The transmitted wave compared to the difference between incident and reflected waves provided a preliminary equilibrium check as visible in *Figure 3.5* for the slower test (longer specimen) and the faster test (shorter specimen). A moderate oscillation of the input-side load does not spoil the overall acceptable equilibrium. The nominal engineering strain rates, corresponding to each combination of the input bar preload and the specimen gage length  $L_o$ , are reported in Table 3.1.

*Figure 3.6* shows the engineering stress-strain curves and the corresponding histories of the nominal engineering strain rate vs. strain, for all the tests of the Al material including cross-combinations of varied gage lengths and input bar preloads. Despite the short specimens with  $L/d = 1$  (*Figure 3.6 a* and *d*) have been tested at nominal engineering strain rates ranging from about 1200 to about 7000  $s^{-1}$ , they exhibit minor differences in the stress-strain response. In fact, 7 out of 8 dynamic curves (solid colour lines) are nearly overlapped each other and over the quasistatic curves (round black marks) up to large strains, while only moderate differences in the stress (about 20 MPa at incipient necking and about 25 MPa at incipient failure) remark the differences between static and dynamic curves. Also the specimens with  $L/d = 3$  (*Figure 3.6 b* and *e*) are tested at engineering strain rates spanning in a six fold range, from 500 to 3000  $s^{-1}$ . The test AL-3-09-04 was affected by electrical noise on the output bar strain gauges probably caused by a failing cable connection; however the noise did not hide nor distort the overall trend of the corresponding curve; the specimen of the slowest test AL-3-09-06 did not broke because a slightly longer incident wave was necessary. Despite these experimental issues, the dynamic engineering curves for  $L/d = 3$  (solid lines) are still very similar each other, while now they are remarkably different from the static ones (round black symbols); in fact, the engineering strains at failure from dynamic tests with  $L/d = 3$  are close to twice those from the quasistatic tests. *Figure 3.6 c* and *f* finally show the results of tests on Al specimens with different  $L/d$  ratios, subjected to identical incident waves, which, due to the different gauge lengths, generated different strain rates. Despite the strain rate variation now spanned in a threefold range from 800 to 2500  $s^{-1}$ , narrower than the six fold variation range of the previous two series of tests, now the resulting engineering strains at failure are much more spread than before, ranging in an almost three fold range, from about 0.2 (for longer specimens) to about 0.6 (for shorter ones). The relationship between the dynamic curves (solid colour lines) and the static ones (round, square and triangular symbols), recalls the moderate differences already discussed for each given geometry when commenting the previous figures.

Then *Figure 3.6* globally conveys the remarkable information that, for this Aluminium alloy, the  $L/d$  ratio affects the stress-strain response much more than the imposed strain rate, at least when the assessment is made in terms of the engineering curves.

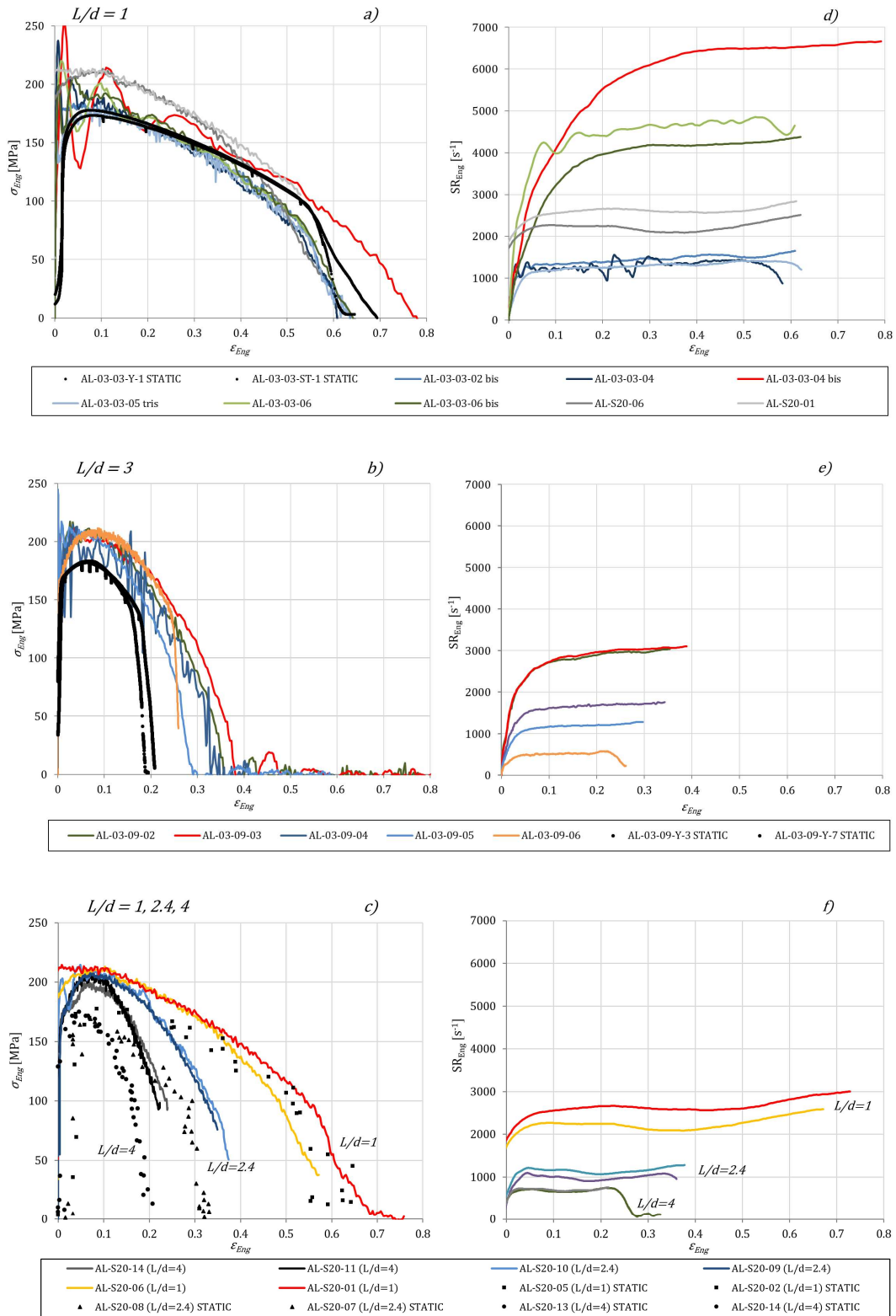


Figure 3.6: Engineering stress-strain and strain rate-time curves for AL 2011

The above data also allow to estimate the stress amplification promoted by the strain rate: all the dynamic curves are visibly higher than the quasistatic ones but only a moderate spread is found between the dynamic stress responses at very different strain rates.

This means that the dynamic amplification of the stress is independent from  $L/d$ , and that its dependence on the strain rate is significant from quasistatic rates up to  $500 \text{ s}^{-1}$  (about 10% increase of the ultimate stress), but becomes small enough that no appreciable differences are found between  $500$  and  $6500 \text{ s}^{-1}$ .

In the next chapter, another explanation is found for this apparent saturation of the strain rate effect, suggesting the possibility that, during the test, an external perturbation arises, capable of preventing the amplification of the dynamic stress to further evolve with the increasing strain rate.

Figure 3.7 shows two Al specimens with  $L/d = 1$  and  $3$  respectively, before and after tests. It is clearly visible that the length of the neck-affected zone is very similar in both cases, because it only depends on the nominal diameter, which is common to both specimens; but such necking-affected zone covers the entire gage length for shorter specimens, while it only covers less than 50 % of the total gage length for longer specimens.

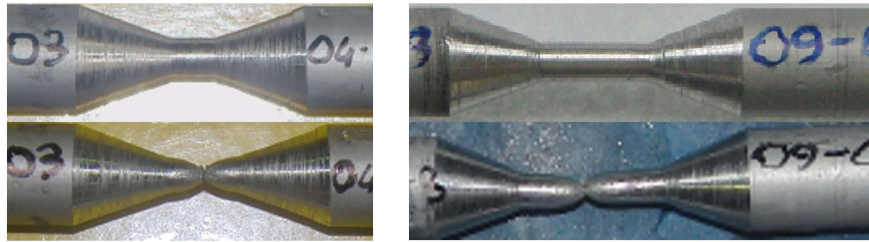


*Figure 3.7: Neck-affected zone in short and long specimens*

This explains why, after the necking onset, the engineering strain express a length-averaged property of the material combined to the specimen geometry, rather than a property of the material alone. In case of shorter specimens with  $L/d = 1$ , the geometry affects the engineering curves to a minimum extent. It is not possible to decrease  $L/d < 1$  because, then, the interaction of the specimen shoulders with very short gage lengths spoils the stress uniaxiality before of necking inception, making the response of such short specimens more similar to that notched bars than to that of smooth ones.

At the same time, the independence of the necking-affected length from the initial gage length confirms that, for whatever  $L/d$  greater than 1, the true stress-true strain data are independent of the specimen geometry, although them still include the effect of the stress triaxiality and non-uniformity generated by the necking itself.

Then, the second series of dynamic tests, on a FEN steel, have been enhanced by video acquisitions by the Phantom V711 high-speed camera and successive image analysis. Synchronization of frames from the video to strain gauges readings from the bars allows to obtain triplets of values of load, elongation and minimum cross section of the specimen at different instants during the dynamic tensile test. Manual post-triggering with backward acquisition of the Phantom camera is adopted for simplicity, so the synchronization of diameters and loads is made by coupling the first frame showing the failing specimen to the drop of the load in the transmitted wave. Then, further strain gauge readings and image measurements are coupled by running backward in the video and in the recorded strain waves, based on the known acquisition rates. So, the camera-assisted engineering curves and the true curves for the FEN steel have been obtained.

Figure 3.8 shows the engineering curves of two representative tests on FEN, corresponding to intermediate strain rates and specimens with  $L/d=1$  and 2.5 and selected for preliminarily checking the agreement of the strain calculation performed according to two different procedures.

The strains of the solid lines are calculated from the reflected wave of the input bar, while the strain of the dotted data is based on specimens elongations measured on pictures acquired by the fast camera.

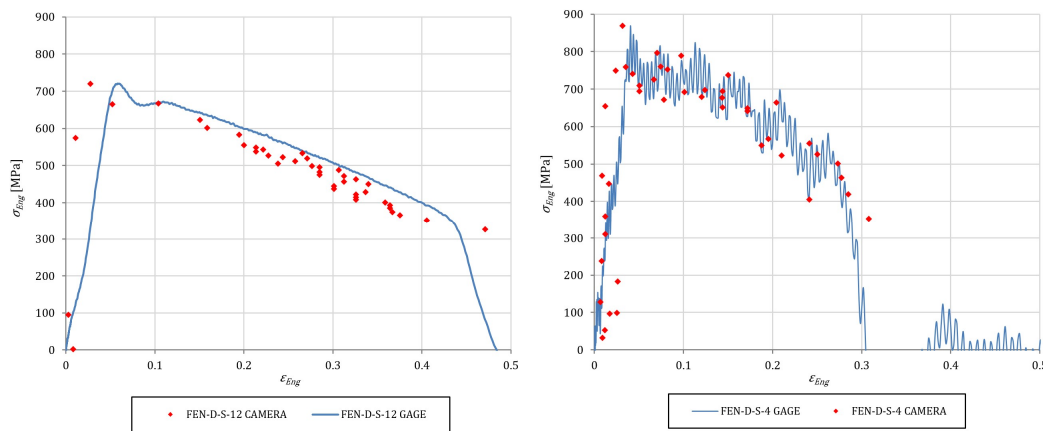


Figure 3.8: Check of engineering strains from reflected wave and from camera elongation readings

The test FEN-D-S-4 is affected by electrical noise disturbing the signal of the transmitted wave, but the overall trend of the curve is fully recognizable also without any filtering.

Before the stress peak, the strains measured by the strain gauges readings on the bars are slightly overestimated; this occurs because, before necking initiates, the stiffness of the specimen gage length is comparable to that of the specimen shoulders and then the overall strain is affected by the shoulders elongation, not included in the image-based strain. Instead, in the post-necking range, the overall

specimen stiffness decreases together with the load, the shoulders are not further elongated anymore and the gross elongation derived from the strain gauges becomes very close to the net elongation of the gauge length alone, so that the agreement between optical and strain gauges measurements improves.

However, both tests show an overall good agreement between the engineering strains obtained from the bar gauges and those from image analysis, so ensuring that both of them are reasonably accurate.

Figure 3.9 shows the engineering curves of three different shapes of FEN specimens with  $L/d$  ranging from 1 to 4, tested at very similar nominal strain rates, evolving between 500 and 1000  $s^{-1}$ ; despite the similar strain rates, the resulting stress-strain curves exhibit very different strains and ductilities.

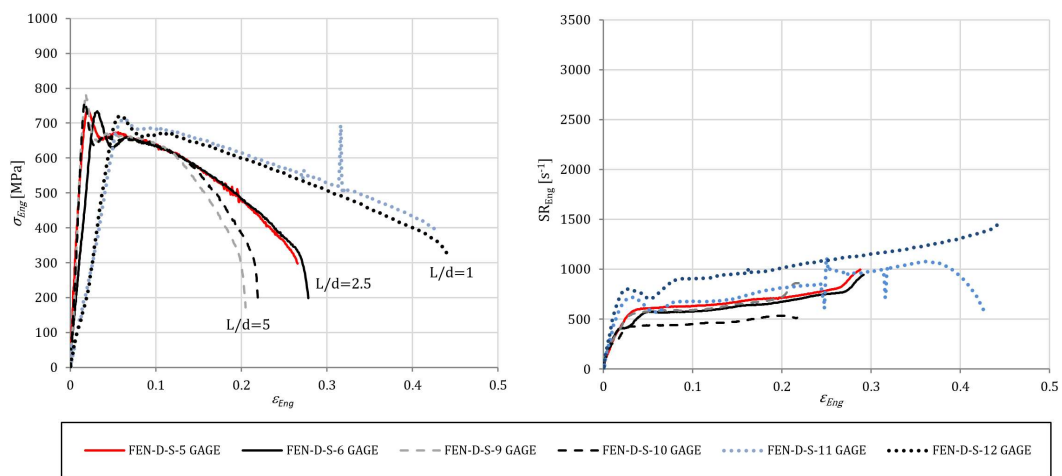


Figure 3.9: Engineering curves of FEN specimens with different  $L/d$  tested at similar strain rates

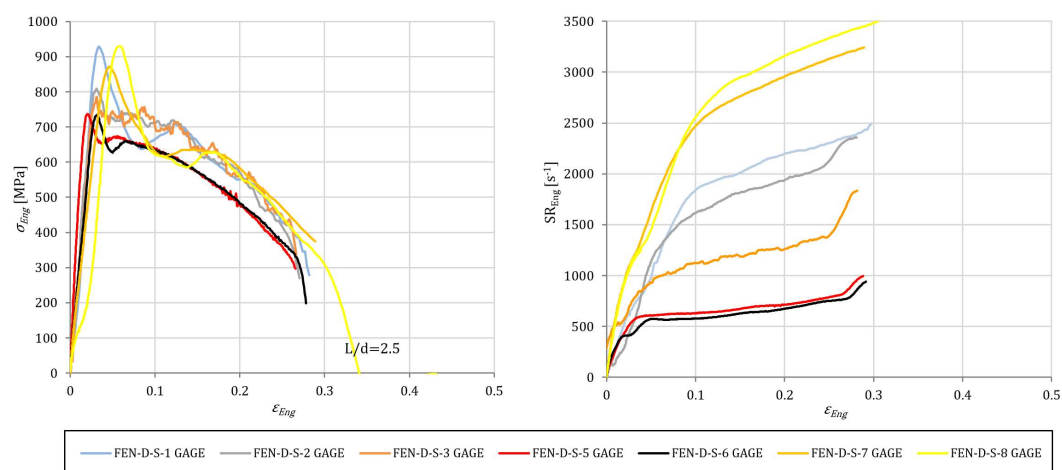


Figure 3.10: Engineering curves of FEN specimens with identical  $L/d = 2.5$ , tested at different strain rates

At the same time, identical FEN specimens with  $L/d = 2.5$ , tested at nominal strain rates varying from about 500 to more than 3000  $s^{-1}$ , produced almost identical engineering curves as visible in Figure 3.10.

The above evidence confirms that, also for the FEN steel, the specimen shape affects the dynamic engineering curves much more than the whole strain rate.

The  $L/d$  ratio also affected the location where necking and failure occurs for the FEN steel. In fact, the shorter specimens with  $L/d < 4$  exhibited necking and failure near their midsection as already seen in Figure 3.7 for the Al alloy, but the longer specimens (15 mm gage length and  $L/d = 5$ , tests FEN-D-S-09 and FEN-D-S-10) necked and failed at about  $\frac{1}{4}$  and  $\frac{3}{4}$  of the gage length on opposite sides, as shown in Figure 3.11.

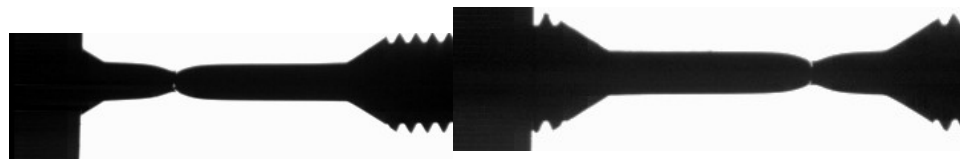


Figure 3.11: Necking and failure location of longer specimens

More accurate true stress-true strain data are now calculated below for the FEN steel at the semi-local scale of the necking cross section, based on the analysis of images from the high-speed camera.

This calculation will show whether or not the above distortions of the material response, promoted by the specimen shape and affecting the engineering curves, also affect the true curves.

The load is determined from strain gauge recordings while the diameter is optically measured by analysing selected frames from the fast camera recordings (Figure 3.12). Both data are synchronized each other by associating the first frame showing either partially or totally fractured specimen, to the value of the transmitted wave at the point of incipient falling of the strain gauge signal. Then, synchronized triplets of load - diameter - time are collected backward at fixed instants, according to the sample rates of the camera and of the strain gauge station.

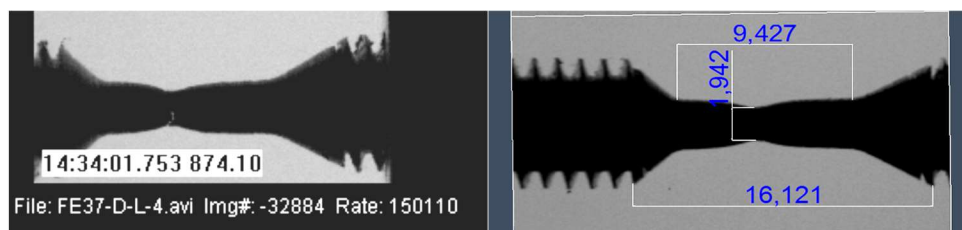


Figure 3.12: Frame extracted from the high-speed camera acquisition for diameter and elongation measurements

Then equations (41) and (42) are applied for calculating the true stress and the true strain at each selected instant of the test, and the knowledge of time intervals also allows to easily calculate the time rate of the true strain.

The true stress – true strain – true strain rate triplets obtained at selected time intervals during the static and dynamic tests are reported in Figure 3.13.

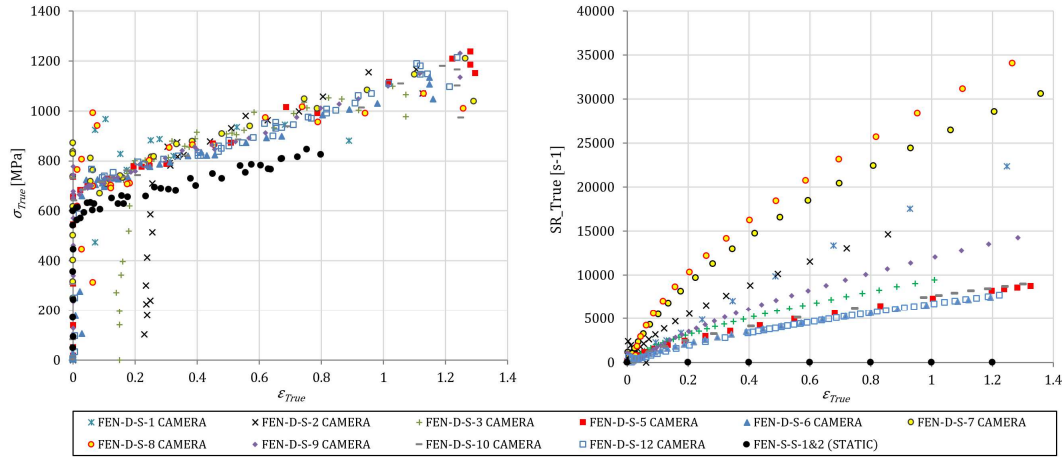


Figure 3.13: True curves and true strain rate data from FEN experiments

The true stress-true strain data from test FEN-D-S 4 are not reported in Figure 3.13 because the oscillations in the load already seen in Figure 3.8 would require too many images analysed for acquiring the same oscillations and preventing errors in the true stress. The true data from the test FEN-D-S-11 are not even calculated because failure was not achieved and then the synchronization between camera frames and load from the transmitted wave was missing.

Tests 2 and 3 evidenced that the corresponding specimens undergone a certain amount of work hardening already before being tested, probably because of excessive crossfeed during the machining of shoulders, which caused a slightly elastoplastic torsion. In fact, such two curves were parallel and slightly higher than the remaining curves but, once the former were translated along the true strain axis of about a 0.2 plastic pre-strain, perfectly matched the latter, and also their failure strains become similar to those from the other dynamic tests.

The first important information conveyed by the left side plots in Figure 3.13 is that all the true curves from the dynamic tests are almost perfectly overlapped and nearly identical each other (within a scattering amplitude smaller than that of the engineering curves in Figures 6-8), with no regard for the imposed strain rate nor for the L/d shape parameter of the smooth specimens.

However all the bundled dynamic true curves are remarkably higher than the quasistatic black-dotted true curves, of about 100 to 150 MPa. Also the dynamic failure strains seem to be nearly independent of the strain rate, although a substantial difference in ductility is observed between the dynamic and the quasistatic tests.



Furthermore, the comparison of the true curves in Figure 3.13 to the engineering curves in the left side of Figure 3.6 and Figure 3.8 confirms that, also at high strain rates, the engineering curves greatly underestimate both the true stresses and the true strains on the neck section, up to very different degrees depending on the specimen geometry.

The true stress-true strain curves in Figure 3.13, with their vertical segment representing the elastic range and their inclined linear segment nearly extending all over the plastic strain range, also show that the Considère strain, at which the necking initiates, is very small and corresponds to the very short fillet between the two above straight segments. The necking initiation strains from all static and dynamic tests are found to lie between the barely measurable values of 0.01 and 0.03.

The second relevant information delivered by Figure 3.13 through the right side plots, is that  $\dot{\epsilon}_{True}$  continuously increases during the test until, at incipient failure, becomes about one order of magnitude greater than the elongation-based engineering strain rate  $\dot{\epsilon}_{Eng}$ , previously plotted on the right side of Figure 3.9 and Figure 3.10.

$\dot{\epsilon}_{True}$  is obviously much more realistic than  $\dot{\epsilon}_{Eng}$ , so one more outcome of the above experiments is the confirmation that the engineering strain rate hugely underestimates the local deformation rate and may also radically change the considerations which can be inferred from experiments. For example, Figure 3.13 shows that the strain rate of the test FEN-D-S-10 is barely higher than that of the FEN-D-S-12 test, while, according to the engineering approach of Figure 3.9, the latter seems to be nearly twice the former. Such considerations confirm that the engineering approach may be rather misleading in the dynamic stress-strain characterization of materials, significantly more than it is already known to be for the quasistatic characterization.

A third useful information can be inferred by comparing both sides of Figure 3.13: the nearly identical dynamic true curves are generated by strain rate histories largely diverging each other after the very early plastic stages; at first sight, this might suggest that the strain rate effect is negligible for the FEN steel. But, at the same time, such dynamical true curves are quite higher than the static ones, which denies the possibility of negligible strain rate effect.

This apparently contradictory outcome means that the strain rate effect is significantly intense within the elastic and the very early plastic stages of each test, when the various strain rate histories are very close to a common trend. This is the reason why the initial segments of all the dynamic true curves are higher than the static ones and equal each other.

Then, as the strain rate histories begin to separate each other, the influence of the strain rate becomes negligible due to some reasons to be further investigated, and this allows the dynamic true curves to remain higher than the static curves and very close each other, despite the largely diverging strain rates.

Further details are investigated in the following about this outcome, allowing to highlight a new aspect of the interaction between stress, strain, strain rate and temperature.

### 3.3 Necking-Induced Freezing of the strain rate effect

#### 3.3.1 Dynamic Response of Titanium Alloy Produced by Electron Beam Melting

The dynamic behaviour of a sintered Electron Beam Ti6Al4V alloy, material already described in Paragraph 2.2.1.1, is investigated here by way of SHTB dynamic tension tests, part of a greater experimental campaign, which was discussed in Paragraph 2.2.1.2.

##### 3.3.1.1 Dynamic Tests Results

Adding to the static tensile tests (circles) already shown in Paragraph 2.2.1.3 the dynamic tensile tests results (triangles) it is possible to obtain the graph shown in Figure 3.14.

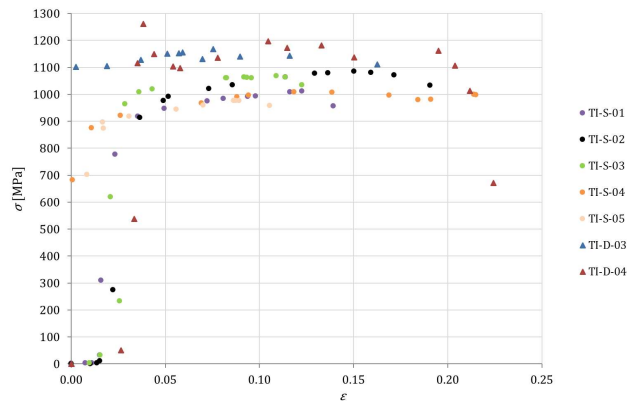


Figure 3.14 True Curves, Static Tensile vs Dynamic Tensile

In such figure, it is possible to see that there is a clear strain rate influence, as the dynamic tests are significantly higher than the static ones (maximum dynamic tension around 1200 MPa while maximum static tension around 1080 MPa). However, there is no influence on the deformation at fracture that is around 0.20 for both.

##### 3.3.1.2 Material Model Calibration and Validation

The yield stress and the  $\epsilon_{neck}$  of the EMB Ti6Al4V are calculated from the experimental data and shown in Table 3.2, while the elasticity modulus is assumed to be 110 GPa as widely suggested in the literature.

Yield Stress	$\epsilon_{neck}$
790 MPa	0.075

Table 3.2 EBM Ti6Al4V parameters

The static true curve from tension tests are approximated by the power law reported in eq. (47) and plotted in Figure 3.15.

$$\sigma = 1230 \varepsilon^{0.075} \quad (47)$$

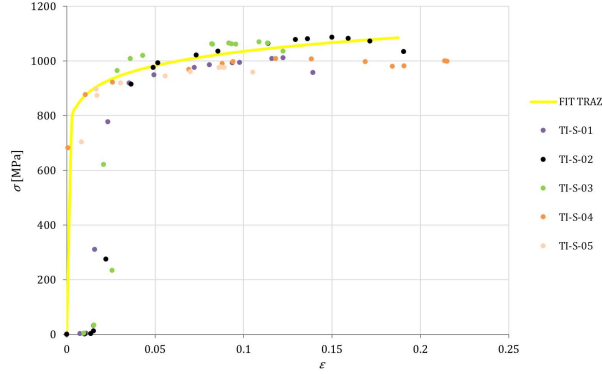


Figure 3.15 Static Tensile true curve calibration

It is possible to obtain the flow tension curve from the true tension curve by means of the MLR function (Mirone, 2004a). However for this Ti alloy, the deformation after necking is very small (from  $\varepsilon_{neck} = 0.075$  to  $\varepsilon_{failure} = 0.20$ ), thus the difference between the true curve and the equivalent curve is almost negligible as shown in Figure 3.16. The obtained material curve has been validated by means of a 2D axisymmetric simulation of the tensile test (Figure 3.17).

Figure 3.16 shows, together with the obtained true and equivalent curves, the true curve regarding the FEM simulation in which  $\sigma$  is calculated as the total axial force divided by the instant area and  $\varepsilon$  is calculated from the instant area reduction. The simulated true curve is almost identical to the desired best fit curve, although a considerable scattering affects the true stress-true strain data from experiments, as already discussed.

In Figure 3.18, the Load-Displacement results of the tensile test simulation are compared to the corrected experimental data showing a very good agreement.

The dynamic true experimental data have been fitted with the following law representing an amplification of the static fitting law:

$$\varepsilon_{true} \leq \varepsilon_{true\_neck} \quad \rightarrow \quad \sigma = (k_0 + csr * \dot{\varepsilon}_{true}) \varepsilon^{0.075} \quad (48)$$

$$\varepsilon_{true} > \varepsilon_{true\_neck} \quad \rightarrow \quad \sigma = (k_0 + csr * \dot{\varepsilon}_{true\_neck}) \varepsilon^{0.075} \quad (49)$$

With

$$k_0 = 1350$$

$$csr = 0.01$$

$$\dot{\varepsilon}_{true\_neck} = 1960 \text{ s}^{-1}$$

This law reflects the fact that the amplification due to the strain rate is related to the actual strain rate value before the onset of necking while afterwards it is related only to the strain rate value at necking although the strain rate continues to increase after that.

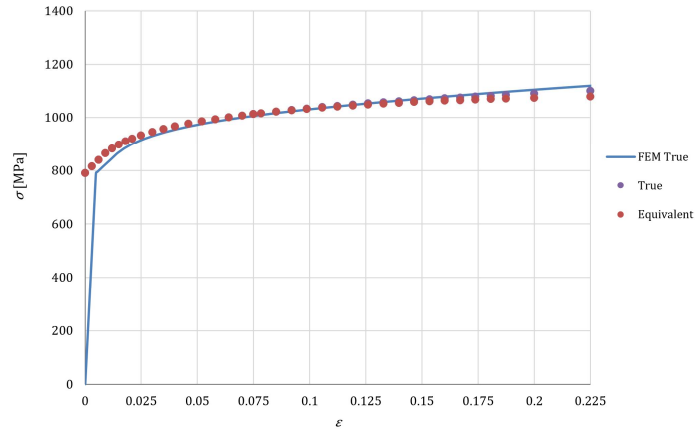


Figure 3.16 True curve vs Equivalent curve vs FEM true curve

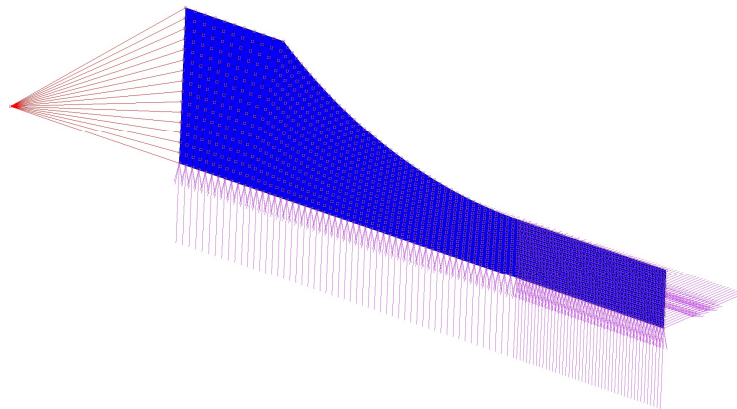


Figure 3.17 Tensile Test axisymmetric FE model

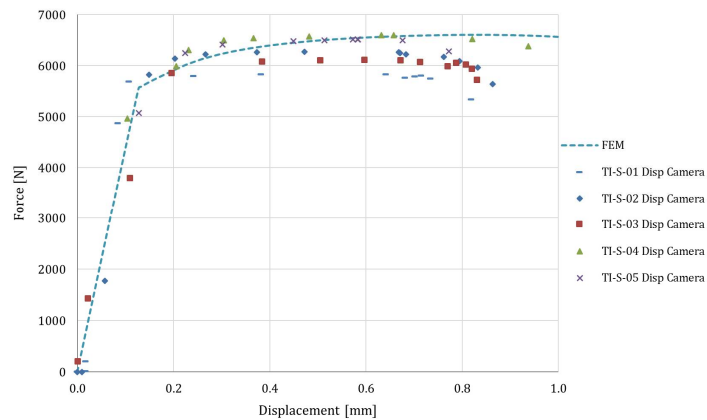


Figure 3.18 Static tensile tests – Exp vs FEM

In Figure 3.19 are shown the fitted dynamic true curve (solid line) together with the static true curve (dashed line) and the experimental dynamic data.

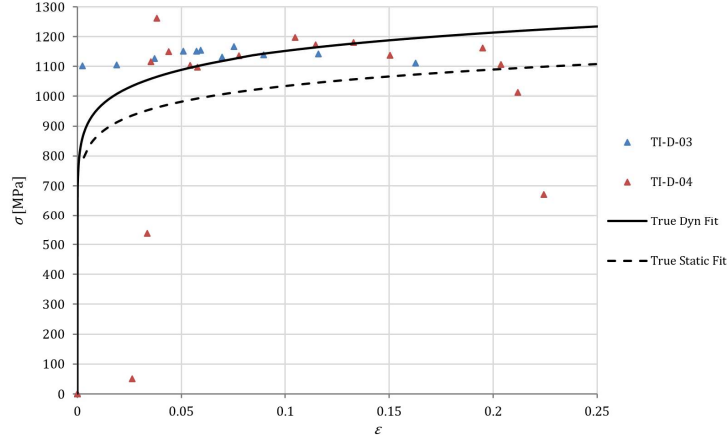


Figure 3.19 Dynamic true EXP vs Dynamic true fitting vs Static true fitting

Considering the strain rate  $\dot{\epsilon}_{true}$  corresponding to each point of the dynamic curve, it is possible to obtain the amplification ratio  $R_{true}$ , function of the strain rate, dividing the values of the true stress of the points of the dynamic curve by the values of the points of the static one with the same  $\bar{\epsilon}_{true}$

$$R_{true}(\dot{\epsilon}_{true}) = \frac{\sigma_{truedyn_{\bar{\epsilon}_{true}}}(\dot{\epsilon}_{true})}{\sigma_{truestat_{\bar{\epsilon}_{true}}}}$$

In Figure 3.20 it is shown the  $R_{true}$  together with the  $R$ , the ratio between the correspondent equivalent values, that it is chosen as the same of the  $R_{true}$  until the strain rate at necking and afterwards it continues to increase linearly.

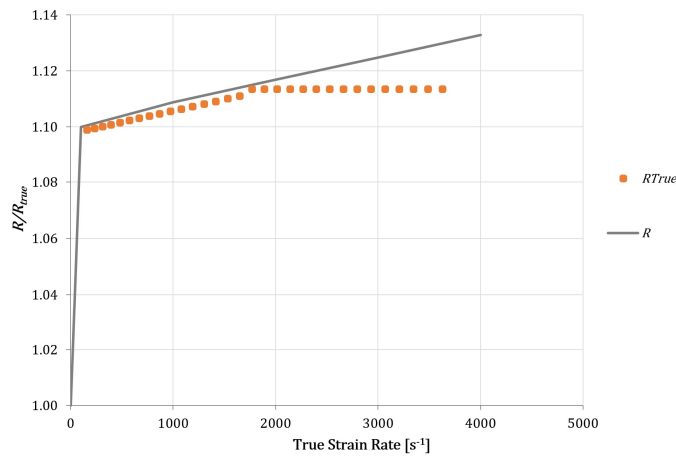


Figure 3.20  $R_{true}$  and  $R$  vs true strain rate

Implementing the obtained amplification law  $R$ , a dynamic transient simulation of the SHTB test has been made with a 2D axisymmetric FE model. In Figure 3.21 the FEM true curve is compared to the dynamic fitting true curve and to the experimental data showing a very good agreement. It is useful to underline that the simulation results are in accordance to the experimental data and to the fitted true dynamic curve also after the onset of necking despite the amplification law  $R$  implemented in the simulation was, after the strain rate at necking, greater than the  $R_{true}$  calculated directly from the fitted static and dynamic curves. This fact confirms that the behaviour of the material after the onset of necking is directly related to the strain rate history until the onset of necking and not to the actual strain rate. This point will be further investigated in the following.

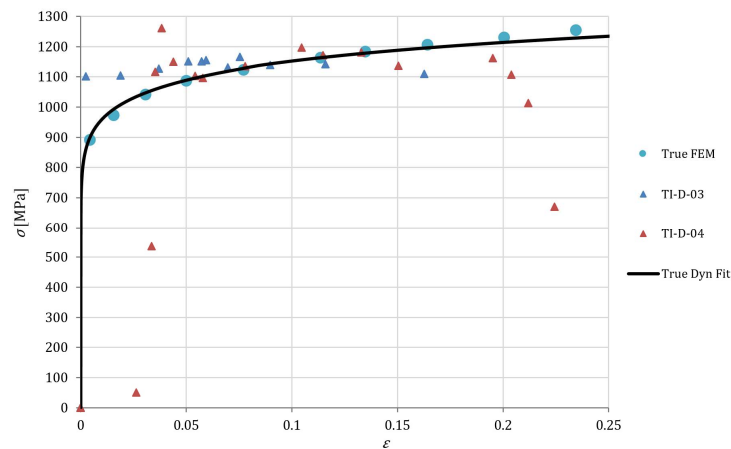


Figure 3.21 Dynamic true curves – EXP vs FIT EXP vs FEM

### 3.3.1.3 Comparison with Literature Data

Integrating what already shown in Paragraph 2.2.1.4, reported here to have a complete view, the static and dynamic true curves obtained in this thesis work from EBM Ti6Al4V specimens with axis orientation perpendicular to the melting plane (UNICT curves), are now compared to the following literature data:

- Static and dynamic curves from rolled Ti6Al4V by Galàn et al. (2013), Peirs et al. (2011) (UGHENT curves),
- Static curve from rolled Ti6Al4V by Allahverdizadeh et al. (2015) (POLIMI curves),
- Static curves from EBM Ti6Al4V specimens with axis orientation parallel and perpendicular to the melting plane, by Rizza (2015) (UNICT-PW curves).

Figure 3.22 shows the above comparison, reporting the static curves as dashed lines and the dynamic curves as solid lines. The true static curves marked with “\*” are obtained by transforming the engineering curves through the well-known relations

$\sigma = S(1+e_p)$  and  $\varepsilon = \ln(1+e_p)$  until the necking onset and completing them with a linear extension tangent to the curve, as a reasonably approximate prosecution of the true curve.

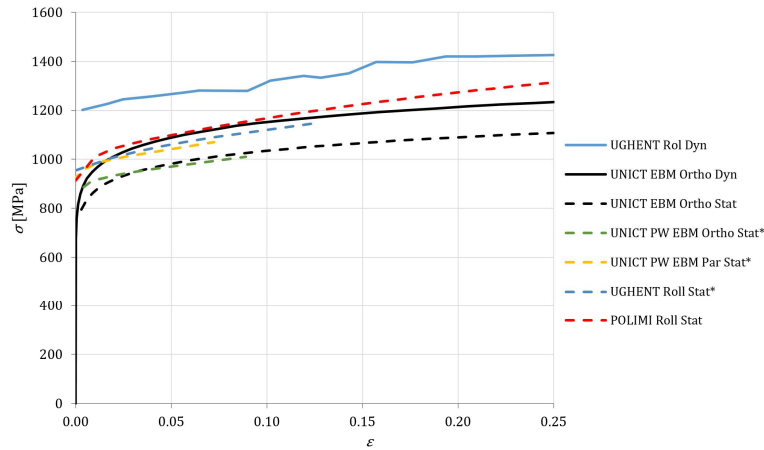


Figure 3.22 True curves – Comparison with literature data. \*Obtained from engineering curves, therefore after necking they are not reliable due to non-uniform strain

The orientation of the EBM specimens with respect to the melting plane of the machine has a great effect on the material behaviour.

When the axis of EBM specimens is parallel to the melting plane (UNICT-PW), the static response of the alloy is very similar that of the rolled alloy Ti-6Al-4V tested at the UGHENT and at the POLIMI. On the other hand, the specimens with axis perpendicular to the melting sections tested by Rizza, exhibit a static behaviour very similar to the initial response of the static specimen tested within this thesis work, unless that the former curves are derived from the engineering curves then only extend up to strains of about 0.1, while the latter ones extend up to failure at more than twice the above strain.

All this data clearly shows that the axis orientation perpendicular to the melting plane decreases the static stress response of about 10% with respect to the case when the axis is parallel to the melting plane.

Similarly, the dynamic true curve obtained in this thesis work is lower than the dynamic curve obtained at the UGHENT for the rolled Ti-6Al-4V; in this case, the difference is also greater than it is for the static curves.

### 3.3.2 FE370 Steel: Dynamic Stress Amplification and Modelling of the Strain Rate Effect

The results of the experimental campaign on the FE370 Steel (named FEN) already shown in Paragraph 3.2.2 are re-shown in Table 3.3 for better readability. However, in this case,  $\dot{\varepsilon}_{Eng}$  is intended as the nominal value provided by eq. (38) at the end of the rise time, when the incident waves exhibit a plateau and the curves  $\dot{\varepsilon}_{Eng}$  vs.  $\varepsilon_{Eng}$

exhibit a clear slope decrease. The reasons for adopting such reference will be clear in the following.

	Specimen	Diameter [mm]	Gage length [mm]	Bar preload [kN]	Nominal Eng. S.R. [s <sup>-1</sup> ]
<b>L/d ≈ 1</b>	FEN-D-S-11	2.9	3.0	15	700
	FEN-D-S-12	3.0	3.5	18	800
<b>L/d ≈ 2.5</b>	FEN-D-S-01	3.2	7.0	52	1800
	FEN-D-S-02	3.1	7.6	50	1500
	FEN-D-S-03	3.1	7.4	35	1000
	FEN-D-S-04	3.1	7.5	38	1200
	FEN-D-S-05	2.6	7.4	20	600
	FEN-D-S-06	2.8	7.5	20	600
	FEN-D-S-07	2.9	6.7	67	2400
	FEN-D-S-08	2.9	6.7	71	2500
	FEN-S-S-01	3.1	7.9	0	STATIC
	FEN-S-S-02	3.1	7.6	0	STATIC
	FEN-S-S-03	3.1	8.1	0	STATIC
	FEN-S-S-04	3.0	8.2	0	STATIC
	<b>L/d ≈ 5</b>	FEN-D-S-09	3.0	14.7	34
FEN-D-S-10		3.1	15.0	28	400

Table 3.3 FEN370 Test grid combining different Bar preloads, specimen lengths and nominal strain rates

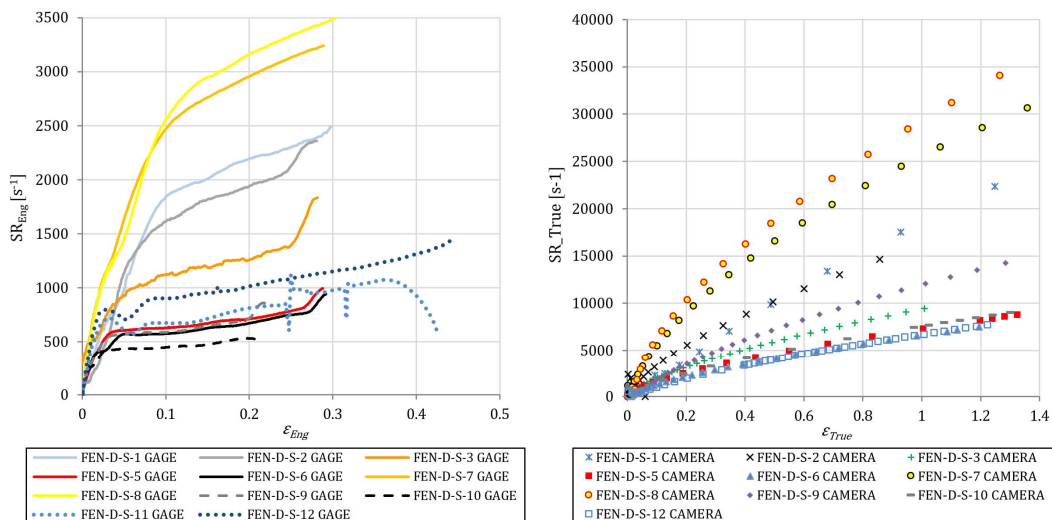


Figure 3.23 Engineering and true Strain rates vs. strains from experiments



The experimental curves of strain rate vs. strain, according to both the engineering and the true approaches, already discussed in Paragraph 3.2.2, are recalled in Figure 3.23.

The first experimental evidence provided by both sides of Figure 3.23 is that the curves of  $\dot{\epsilon}_{Eng}$  quickly increase up to 500 – 2000 s<sup>-1</sup> depending on the incident wave of each test and then change their trends by either further increasing with a much smaller slope (faster tests) or by becoming nearly constant (slower tests). Instead,  $\dot{\epsilon}_{True}$  monotonically increases up to maximum values at failure nearly 10 times greater than the engineering ones, without any remarkable change of the increasing trends.

For the two extreme cases, at failure,  $\dot{\epsilon}_{Eng}$  is 3'700 s<sup>-1</sup> for the “fast” test FEN-D-S-08 and 1'300 s<sup>-1</sup> for the “slow” test FEN-D-S-12, while the corresponding values of  $\dot{\epsilon}_{True}$  are close to 35'000 s<sup>-1</sup> and 8'000 s<sup>-1</sup>.

The slowest test of the lot was the 11<sup>th</sup> but failure was not reached and that test was not further considered because, with such a low-amplitude, a longer incident wave was necessary for ensuring the specimen failure.

The great difference between the nominal  $\dot{\epsilon}_{Eng}$  and the effective  $\dot{\epsilon}_{True}$  is clearly due to the necking, which generates much greater local strains than those detectable by the simple elongation of the specimen.

A secondary information conveyed by Figure 3.23, already highlighted, is that the engineering approach delivers wrong data beyond the necking onset, also for the strain rate, because the engineering measurements are strongly affected by the specimen length/cross section ratio. According to the strain-gauge based curves of  $\dot{\epsilon}_{Eng}$  (left side of Figure 3.23), the slowest test after the necking onset is the FEN-D-S-10 (specimen length 15 mm); instead, the camera-based curves of  $\dot{\epsilon}_{True}$  (right side of Figure 3.23) show that the slowest test is FEN-D-S-12, independently of its shorter specimen 3 mm long.

Figure 3.24 reports the true stress-true strain curves from static and dynamic experiments, already discussed in Paragraph 3.2.2.

Such Figure delivers the third experimental evidence: all the dynamic true curves,  $\sigma_{True}$  from SHTB tests, although being remarkably higher than the static true curve  $\sigma_{True-St}$ , are nearly identical and overlapped each other, despite the large differences between the corresponding  $\dot{\epsilon}_{True}$  histories.

All true curves are almost linear over the entire plastic strain range, as shown by the good matching with the best fit curves, with a barely detectable fillet running from the first yield up to a few percents of plastic strain.

Specimens FEN-D-S-02 and 03 were accidentally prestrained during the machining, then their true curves required a shifting along the strain axis of about 0.2 for perfectly matching the true curves of the other SHTB tests.

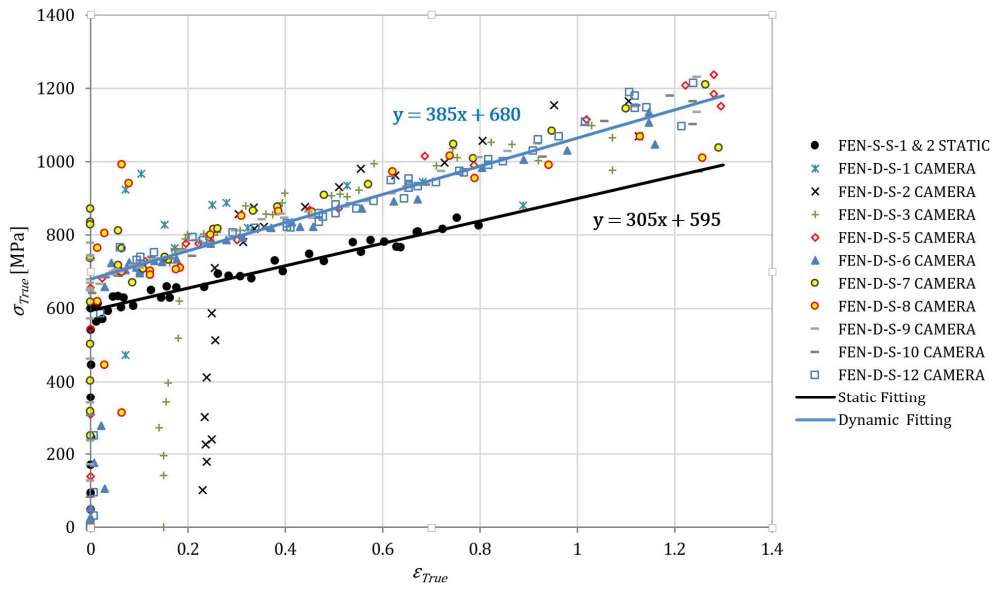


Figure 3.24 Static and dynamics true curves

The necking strain for the FEN steel lies between 0.02 and 0.03 for both static and dynamic tests; instead, the dynamic failure strains, very close each other independently of the strain rate history, are much greater than the static failure strain.

### 3.3.2.1 Dynamic Stress Amplification and Modelling of the Strain Rate Effect

From the stress-strain curves at different strain rates, it is possible to determine the dynamic hardening. According to the most known models in the literature, like that by Johnson and Cook (JC) in eq. (50) (Johnson & Cook, 1983), the dynamical hardening stress is the product of uncoupled terms each representing the static hardening, the dynamical amplification and the thermal softening, as in eqs. (51), (52) and (53), respectively.

$$\sigma_{Eq} = (A + B\varepsilon_{Eq}^n) \left( 1 + c \frac{\dot{\varepsilon}_{Eq}}{\dot{\varepsilon}_{Ref}} \right) \left[ 1 - \left( \frac{T - T_{Room}}{T_{Melt} - T_{Room}} \right)^m \right] \quad (50)$$

$$\sigma_{Eq\_St} = (A + B\varepsilon_{Eq}^n) \quad (51)$$

$$R(\dot{\varepsilon}_{Eq}) = \left( 1 + c \frac{\dot{\varepsilon}_{Eq}}{\dot{\varepsilon}_{Ref}} \right) \quad (52)$$

$$S(T) = \left[ 1 - \left( \frac{T - T_{Room}}{T_{Melt} - T_{Room}} \right)^m \right] \quad (53)$$

Then, according to the standard procedures for the calibration of such models, the dynamic amplification representing the strain rate effect can generally be obtained

as the ratio in eq. (54) between the dynamic flow stress (eventually deperated of the thermal softening) and the static flow stress. Every value of such ratio, calculated at selected strains during each test, must be coupled to the corresponding current value of the true strain rate.

$$R = \frac{\sigma_{Eq}/S(T)}{\sigma_{Eq,St}} \quad (54)$$

The envelope of couples  $(R, \dot{\epsilon}_{True})$  obtained from different dynamical tests, is then approximated by suitable mathematical functions for finally delivering  $R(\dot{\epsilon}_{True})$  for the material at hand.

Usually, for the calibration of dynamic material models, the hypothesis is made that  $R$  and  $\dot{\epsilon}_{True}$  are constant during each test or, at least, are so moderately variable that their mean value is representative of the entire evolution during the test, so that each tests delivers a single point in the plane  $R - \dot{\epsilon}_{True}$  and the points from different experiments can be then easily best-fitted.

Unfortunately, physics reality during SHTB tests evolves quite differently. In fact, the hypothesis of constant true strain rate only applies during an either small or negligible fraction of the test, extending from the end of the rise time of the reflected wave up to the necking initiation. Before and after such phase the effective strain rate  $\dot{\epsilon}_{True}$  is always increasing and, for materials with early necking like the FEN steel, such phase of temporary approximate constancy of  $\dot{\epsilon}_{True}$  is nearly completely missing.

An apparent constancy of the strain rate up to failure during SHTB experiments can only show up if the nominal and poorly accurate engineering strain rate  $\dot{\epsilon}_{Eng}$  is adopted instead of the much more meaningful and accurate  $\dot{\epsilon}_{True}$ .

Therefore, if the effective strain rate  $\dot{\epsilon}_{True}$  is considered, then also the dynamic amplification  $R$  (ratio of dynamic to static equivalent curves) can be hardly assumed to be constant during SHTB tests. In fact, before the necking inception,  $\sigma_{Eq} = \sigma_{True}$  and  $R$  is identical to the ratio  $R_{True}$  (of the dynamic to static true curves) which, as will be shown in the next sections, is highly variable. Beyond the necking onset,  $\sigma_{Eq}$  starts deviating from  $\sigma_{True}$  and cannot be determined without a suitable post necking correction valid for dynamic strain histories; then also  $R$  deviates from  $R_{True}$  and cannot be exactly determined, thus any hypothesis about its constancy cannot be based on any experimental evidence.

The post necking correction of  $\sigma_{True}$  for estimating  $\sigma_{Eq}$  is a consolidated practice for static tests where Bridgman-like corrections are known by decades and the MLR material-independent correction Mirone (2004a) proved to be simpler and more accurate.

The suitability of the MLR postnecking correction for dynamic SHTB true curves has been investigated in Mirone (2013) and Mirone et al. (2017) with encouraging

preliminary outcomes, but here we are momentarily supposing that no postnecking correction is yet available for the dynamic true curves.

Then,  $\sigma_{True}$  based on the optically-enhanced diameter measurements is the best possible experimental estimate of  $\sigma_{Eq}$  also in the dynamic postnecking range and, in turn,  $R_{True}$ , largely variable up to failure, is the best available fully-experimental estimate of  $R$  although its approximation is not yet known.

So the hypothesis  $R=R_{True}$  is provisionally adopted here also beyond the necking onset, for determining the experimental dynamic amplification of the FEN steel; in the next sections this point will be further discussed in detail.

The experimental “true” data discussed in the previous section are now processed and combined together for delivering the trends of the static flow curve  $\sigma_{Eq-st}(\epsilon_{True})$  and of the dynamic amplification  $R(\dot{\epsilon}_{True})$ .

The identical true curves from the SHTB experiments at different strain rates demonstrate that the thermal softening is either negligible or that it is acting with the same magnitude for all tests, independently of their strain rate.

Then the assumption  $S(T) \approx 1$  is made here and any thermal effect eventually common to all experiments is then implicitly included as a constant within the dynamic amplification.

The static true curve is firstly prolonged, by the linear best fit, up to the plastic strain of 1.3 for covering, by estimate, the plastic range where the static failure already occurred while the dynamic specimens are not yet failed.

Then, for each SHTB test, the ratio  $R \approx R_{True} = \sigma_{True} / \sigma_{True-st}$  is calculated at selected strains and is finally associated to the corresponding current value of  $\dot{\epsilon}_{True}$ . This procedure delivers trends of the strain rate effect largely differing from a test to another.

Figure 3.25 shows the dynamic amplification of the stress,  $R(\dot{\epsilon}_{True})$ , for the two extreme tests: the fastest FEN-D-S-08 and the slowest one FEN-D-S-12, where the strain rate reaches maximum values at failure of about 35000 and 9000  $s^{-1}$ , respectively.

Both the experimental trends have a short common initial phase where where  $\sigma_{True}$  is amplified of about 14% within strain rates below 1000  $s^{-1}$ , while at higher values of  $\dot{\epsilon}_{True}$  the two curves largely diverge each other, because the same values of the ratio  $\sigma_{True} / \sigma_{True-st}$  at each given strain are associated to very different values of  $\dot{\epsilon}_{True}$ .

For example, at incipient dynamic failure (plastic strain 1.3),  $\sigma_{True}$  is about 18% higher than  $\sigma_{True-st}$  for whatever dynamic test, but the condition  $R=1.18$  must be then associated to  $\dot{\epsilon}_{True}=35000 s^{-1}$  for the “fast” test FEN-D-S-08 and to  $\dot{\epsilon}_{True}=9000 s^{-1}$  for the “slow” test FEN-D-S-12.

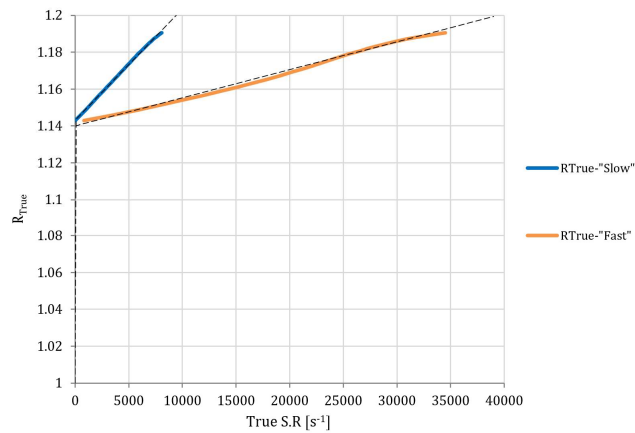


Figure 3.25 Dynamic amplification from the extreme experimental tests 08 (Fast) e 12(Slow)

The other tests, corresponding to intermediate strain rates, returned a series of  $R_{True}$  trends perfectly included within the boundaries of Figure 3.25, with the initial nearly-vertical segment of the trend still common to all tests and the successive segment still linear, with intermediate slopes between those of the extreme tests. Then, for simplifying our discussion, in the following sections of this paper we will refer to the extreme “fast” and “slow” tests alone.

The important information conveyed by Figure 3.25 is that the dynamic amplification  $R_{True}$ , directly derived from experimental measurements without any modeling hypothesis, is common to all tests only within the very early plastic stages, while it largely deviates from a test to another beyond such initial stage.

In other words, the dynamic amplification  $R_{True}$  is an intrinsic property of the material only at the beginning of each test while, beyond a certain threshold better investigated ahead, it quits being a material property and becomes a feature of the single straining history, different from a test to another.

It is worth noting that, until the necking onset,  $R_{True}$  is perfectly coincident to  $R$ , which is a characteristic material property independent of the history of strain and of stress triaxiality, because it is based on  $\sigma_{Eq}$  and  $\sigma_{Eq-St}$ : then, also  $R_{True}$  in the pre-necking strain range is a material property independent of the test.

In the next section, the experimental data so far analyzed are used for calibrating a series of material models which are then implemented in as many FEM analyses. The comparison of FEM results against experiments allows to understand which material models deliver realistic predictions and which are poorly accurate; the validated FEM results also allow to investigate on the evolution of relevant variables at the local scale within the specimen volume, which is clearly impossible to be done directly by experiments.

### 3.3.2.2 Hardening Models

The experimental data are used for calibrating two different material models. The first one is that by Johnson and Cook (JC), the second one is still based on the product of uncoupled functions  $\sigma_{Eq-St}(\epsilon_{True})$ ,  $R(\dot{\epsilon}_{True})$  and  $S(T) \approx 1$ , but the

mathematical form adopted for such functions is more general because comes from the best fit of the experimental trends and, then, completely differs from that of the JC model.

Furthermore, the single-parameter logarithmic function  $R(\dot{\epsilon}_{True})$  of the JC model is calibrated for describing the average response of all tests over their entire range of strain rates, as usual in the literature. Instead, the model based on the general multiparameter best fit functions is calibrated for describing three different dynamic responses all accurately copying the initial part of the experimental response, common to all tests, and then diverging each other according to three different trends better described ahead.

The first term of the characterization is the static hardening. Before the necking onset ( $\epsilon_{True} < 0.02$ ),  $\sigma_{Eq-St}$  is perfectly coincident to the experimental  $\sigma_{True-St}$ . After the necking onset  $\sigma_{Eq-S}$  must be obtained via a post-necking correction of  $\sigma_{True-St}$ . The MLR material-independent polynomial is adopted here for such correction, so that:

$$\sigma_{Eq-St}(\epsilon_{True}) = \sigma_{True}(\epsilon_{True}) \cdot MLR(\epsilon_{True} - \epsilon_N) \quad (55)$$

with  $\epsilon_N$  the true strain at the necking inception (Considère strain).

The left-side plot in Figure 3.26 shows the experimental true curve points together with their best fit curve (power law before the necking and linear function after the necking) and with the static flow curve  $\sigma_{Eq-St}$  obtained by eq. (55).

The remarkable difference between  $\sigma_{Eq-St}$  and  $\sigma_{True-St}$  suggests that, if the true curve is adopted as the constitutive curve without any post necking correction, then a large error up to 20% is expected at failure.

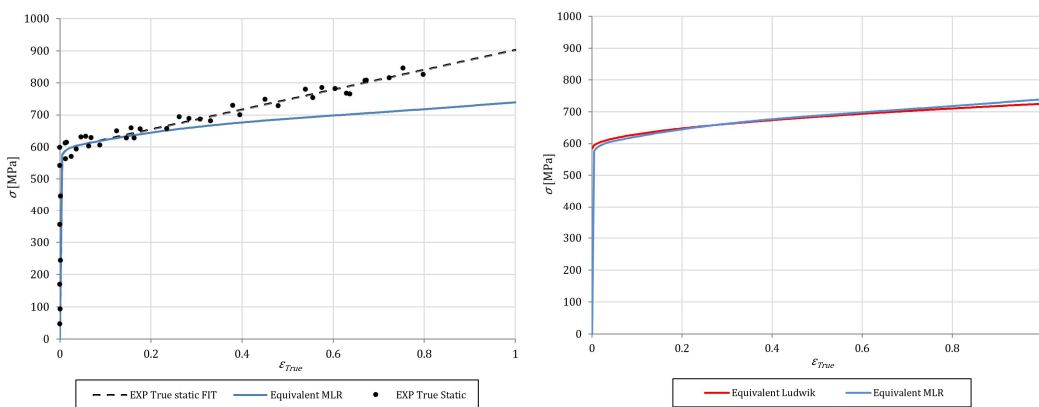


Figure 3.26 Static true stress and equivalent stress by MLR correction (left), Ludwik and MLR flow curves (right)

The plot on the right side of Figure 3.26 shows the above MLR-based  $\sigma_{Eq-St}$  curve together with a Ludwik-type curve calibrated for nicely approximating the same

trend ( $A = 585$ ,  $B = 140$ ,  $n = 0,5$ ). The Ludwik curve, identified for implementing the JC material model, only very slightly differs at failure from the target curve.

It is important to underline that the general suitability of the Ludwik law for nicely approximating a hardening function cannot prevent considerable errors if it is used for the best fit of just true stress-true strain data without any post-necking correction, as it is sometimes done in the literature. In the latter cases, iterative procedures based on FEM are necessary for refining the initial tentative calibrations of the Ludwik laws based on just uncorrected true curves.

The validation of the MLR-based static hardening is provided in Figure 3.27 where the true stress-true strain curve predicted by FEM is shown to closely follow its experimental counterpart.

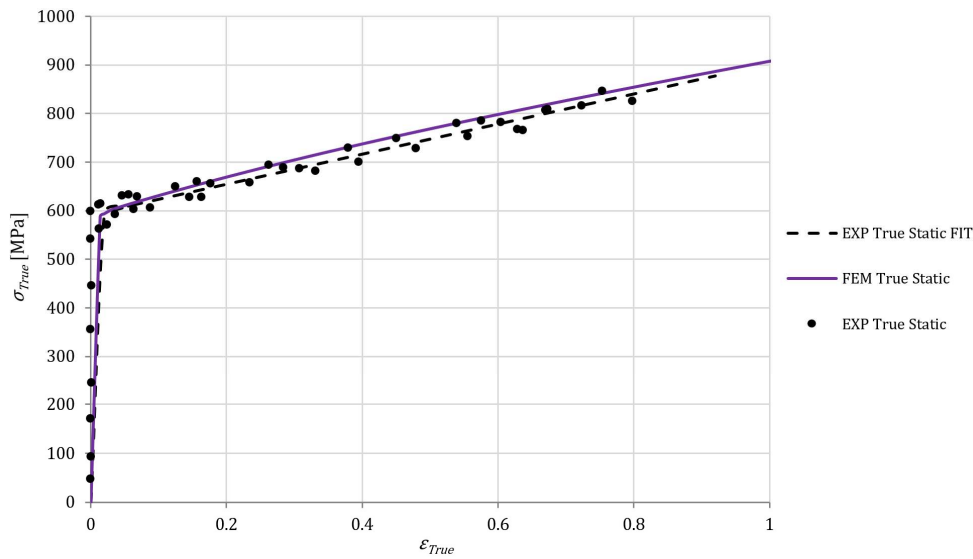


Figure 3.27 Validation of the static hardening: static true stress from experiments and from FEM

The FEM prediction of the true curve is obtained by introducing load and displacement readings, taken at different deformation stages on the nodes of the neck section, into equations  $\sigma_{true} = \frac{F}{A}$  and  $\epsilon_{true} = Ln \frac{A_0}{A}$ .

After the static hardening function  $\sigma_{Eq\_St}(\epsilon_{True})$  is identified and validated, the dynamic amplification can be derived from the results of SHTB experiments.

For any general uncoupled model of time-dependent plasticity, the function  $R(\dot{\epsilon}_{True})$  expressing the strain rate effect must be capable of describing all the dynamic amplifications really obtained by dynamics experiments with the given material.

While for the FEN steel this is possible at the early stages of each test, when the dynamic amplifications from all experiments are identical each other, it becomes obviously impossible at strain rates beyond  $500$  or  $1000 \text{ s}^{-1}$ , when each experiment

starts delivering its own trend of the ratio  $\sigma_{True}/\sigma_{True\_St}$ , largely diverging from that of other tests.

Then, different tentative functions are identified here for describing the strain rate effect: two of them are the piecewise linear functions of the extreme tests already seen in Figure 3.25,  $R_{True-Fast}$  and  $R_{True-Slow}$ .

The third is a Johnson-Cook logarithmic function approximating, within the limits of the single available calibration parameter ( $c=0.019$ ), both the initial ramp common to all the experiments and the successive set of experimental trends, largely diverging each other. This dynamic amplification is called  $JC_{mean-0.019}$ .

The fourth tentative function is identified according to the following considerations: the strain rates at which the experimental trends of  $R$  start differing each other (between 500 and 1000  $s^{-1}$ ) correspond to plastic strains of about 0.02 - 0.03 (see Figure 3.23), which nicely correspond to the strain range at which the necking initiates for all the static and dynamics experiments with the FEN steel.

As far as the experimental curves  $R$  from different tests with the same FEN steel are identical each other, they can represent a material property; instead, as they start diverging each other, they become a mixed property of the material and of the stress-strain history generated by each different test condition (incident wave and specimen length).

Before the necking onset, the true stress of smooth specimens is coincident to the equivalent stress and, then, the ratio  $R$  of dynamic to static true curves certainly expresses a material property. Instead, after the necking onset, the true stress always includes increasing amounts of hydrostatic stress generated by the evolution of the neck profile which, in turn, depends on test-related variables like the local accelerations, the specimen inertia and the imposed incident wave.

The above considerations suggest that the initial steep ramp common to all the experimental  $R$  curves really expresses the effective dynamic amplification of the FEN steel in the pre-necking phase. Instead, after the necking onset, the experimental results, with their very different slopes spanning over a good portion of the plane  $R-\dot{\epsilon}_{True}$ , cannot be representative of the dynamic amplification for the FEN steel.

Then, a fourth tentative function is made by the initial steep segment from the experiments up to 500  $s^{-1}$ , followed by a flat plateau which makes the simulated dynamic amplification to be frozen near the necking onset; such fourth function is called  $R_{True-Flat}$ .

The four tentative functions expressing the dynamic amplification of the FEN steel are plotted in Figure 3.28.



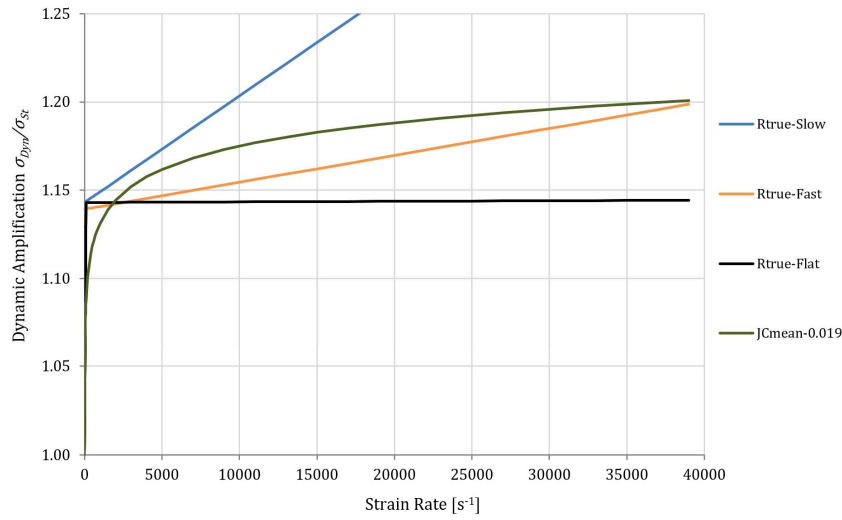


Figure 3.28: Tentative functions for modelling the strain rate effect

The dynamic amplifications  $R_{True-Fast}$ ,  $R_{True-Slow}$  and  $R_{True-Flat}$  in Figure 3.28 are joined to the MLR-based static hardening  $\sigma_{Eq\_St}$  from Figure 3.26 and to the position  $S(T) \approx 1$ , so delivering three generalized tentative functions of the dynamic hardening.

As already discussed before, the assumption  $S(T) \approx 1$  is recalled for taking into account that all the dynamic true curves from experiments at different strain rates are equal each other, while at the same time they are quite different from the static true curve. This means that the thermal softening is either negligible or it is identical for all the SHTB tests independently of their strain rate, so that the thermal softening is already implicitly included in the dynamic true curves and, in turn, into the dynamic amplification  $R$ .

Instead, the dynamic amplification  $JC_{mean-0.019}$  in Figure 3.28 is joined to the static hardening  $\sigma_{Eq\_St}$  from Figure 3.26 based on the Ludwik approximation and to the constant  $m=100$  in eq. (53) for turning off any further thermal effect exceeding that already included in the  $R$  functions, so delivering the fourth tentative dynamic hardening, fully complying to the Johnson-Cook approach.

The three generalized dynamic hardenings are implemented in the FEM simulations via Fortran user subroutines while the fourth JC dynamic hardening is implemented via the Johnson-Cook model available in the commercial FEM code MSC-Marc.

In the next section, the FEM simulations of the two “extreme” experiments are discussed, and the simulations results are compared to the experiments for understanding if/how the different tentative functions are adequate for describing the effective material response.

### 3.3.2.3 FEM Simulations and Experimental/Numerical Comparison

The implicit FEM simulations of the dynamic transients are based on the updated Lagrangian formulation with large displacements and finite deformation. Although

more time-consuming, the implicit analysis is more reliable than the explicit one when dealing with high plastic strains and largely non-proportional stress paths at the local scale, like those induced by the necking of ductile metals in tension (Ruggiero, 2005).

Four-noded full integration axisymmetric elements are used for modeling the elastoplastic specimen together with the purely elastic input and output bars; as better highlighted ahead, including the bars in the FEM model is an essential condition for getting very useful information from the analyses.

The mesh of the specimen is made of 24 elements along the radial direction for accurately getting the distributions of triaxial stresses on the neck section up to large postnecking strains, and of 300 elements along the specimen axis with an initial axial/radial aspect ratio of about 0.3, for ensuring that all elements remained reasonably stretched (aspect ratio lower than 3) up to strains beyond 1.1.

Instead, the bars just undergo small uniaxial elastic stresses, thus their discretization is based on six elements along the radius with an axial/radial aspect ratio close to three for limiting the total number of elements.

Four series of analyses are ran, each simulating the two extreme SHTB experiments, where the response of the FEN steel is modeled by the four functions of dynamic hardening defined in the previous section.

The incident waves of the “faster” and the “slower” tests are modeled according to the experimental strain gage acquisitions and are imposed, as time-dependent pressures, onto the nodes of the end section of the input bar, leaving such pressure waves free of propagating along the input bar and of being reflected/transmitted at the specimen-bars interfaces, as in the real experiments.

Figure 3.29 shows qualitatively the necked specimen between short segments of the input and output bars, on the left and the right side respectively.

The radial displacements and the axial stresses are read on the nodes of the neck section at selected time steps during each analysis, so that the current cross section and the current load introduced finally deliver the evolutions of  $\sigma_{True}$ ,  $\epsilon_{True}$  and  $\dot{\epsilon}_{True}$ .

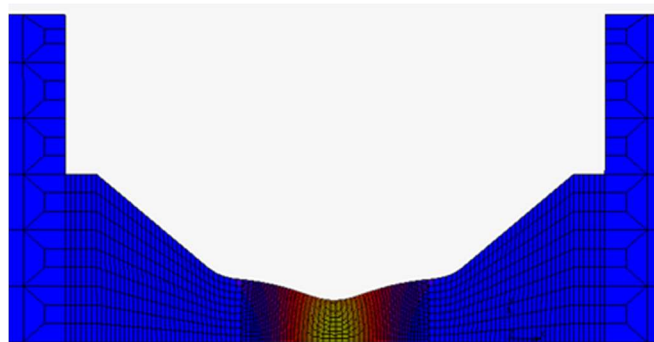


*Figure 3.29 Deformed FEM specimen with bar interfaces*

Also  $\sigma_{Eq-A}$ , the von Mises stress averaged onto the current neck section, can be obtained from FEM simulations at different deformation stages for eventually checking whether or not the ratio  $\sigma_{Eq-Av} / \sigma_{True}$  evolves according to the material-independent *MLR* polynomial, as it always occurs during static tension tests.

The accuracy of each tentative dynamic hardening is firstly checked by comparing the true curves from FEM to those from experiments.

The left-side plot in Figure 3.30 shows that all the dynamic FEM true curves are close to the experimental ones and also are barely discernible each other, independently of the adopted hardening function and of the incident wave, as also the experimental true curves were.

This outcome demonstrates that, also according to the plasticity equations integrated by FEM, the true stress only depends on the dynamic amplification at the very beginning of the strain histories, where the four tentative dynamic amplifications  $R$  are almost identical each other and make  $\sigma_{True}$  about 15% greater than  $\sigma_{True-St}$ .

After the necking onset, where the four tentative dynamic amplifications start diverging each other, also the  $\sigma_{True}$  predicted by FEM becomes poorly sensitive to the strain rate and then, in the post-necking range, such true stress cannot be used anymore as the indicator of how accurate the dynamic amplification is.

Also the function  $R_{True-Slow}$ , which after the necking inception grows much faster than any other tentative function  $R$ , delivers true curves overlapped to those from the other three  $R$  functions.

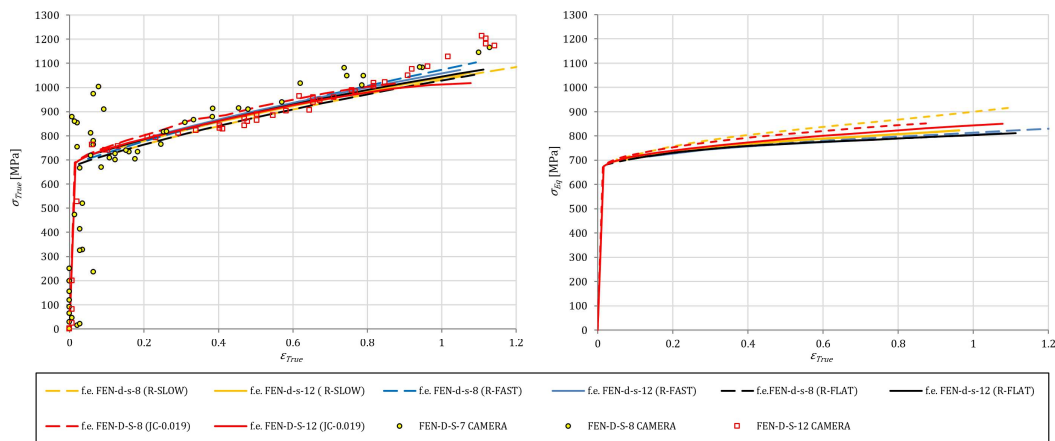


Figure 3.30 Comparison of Exp. vs. FEM true curves (left), Mises stress from FEM (right).

It is worth underlining that the low sensitivity of the true curves to the strain rate in the post necking range applies to the FEM results independently of the experimental evidences confirming them; so, such behavior seems to be intrinsic to the elastoplasticity framework.

The right-side plot of Figure 3.30 shows that, instead, the curves of equivalent stress from FEM diverge each other remarkably more than the true curves do, showing then a greater sensitivity to the strain rate.

This can be explained by considering that  $\sigma_{Eq}$  does not include any hydrostatic stress and then is fully dependent on the strain rate, as the constitutive equation imposes through the  $R$  function. Instead, the post-necking  $\sigma_{True}$  includes increasing amounts of hydrostatic stress which, by definition, is insensitive to the strain rate.

The above evidences about  $\sigma_{True}$  and  $\epsilon_{True}$  do not help yet for identifying which one of the four  $R$  functions is the most accurate. Then, the only other relationship directly derived from experiments and available for validation purposes is considered now: the curves  $\dot{\epsilon}_{True}$  vs.  $\epsilon_{True}$  determined from the FEM simulations are compared to those from experiments in Figure 3.31.

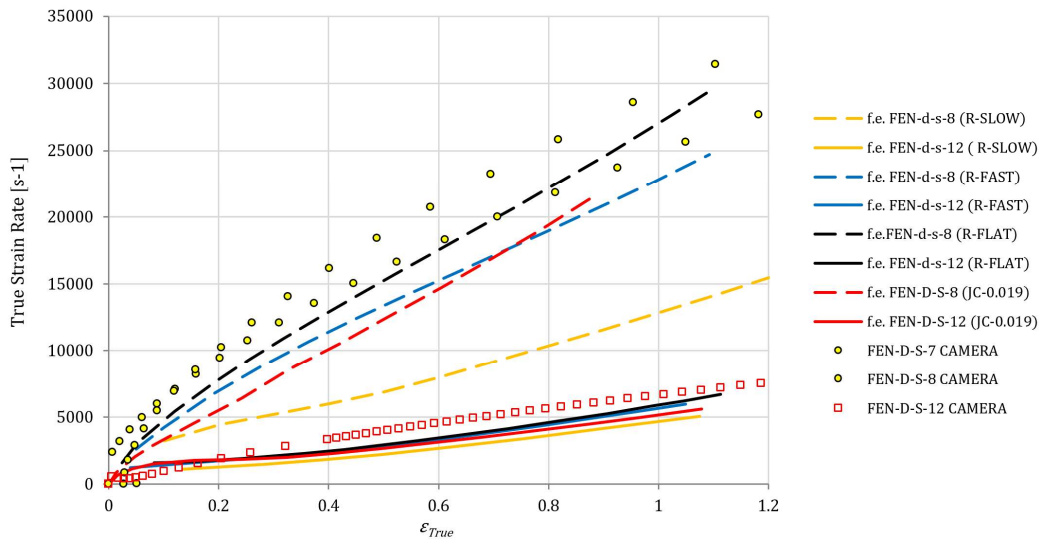


Figure 3.31 Comparison of Exp. vs. FEM true strain rates

The comparison of numerical to experimental true strain rates, reported in Figure 3.31, nicely shows that only the dynamic amplification  $R_{True-Flat}$  is capable of delivering FEM results in good agreement with the experiments, while the other three tentative functions  $R_{True-Fast}$ ,  $R_{True-Slow}$  and  $JC-0.019$  remarkably underestimate the true strain rate histories.

This demonstrates that the dynamic amplification of the hardening must be really frozen at the necking onset for returning a realistic material response, as implemented by the function  $R_{True-Flat}$  which models the only dynamic amplification capable of returning the real evolution of  $\dot{\epsilon}_{True}$ .

In other words, it is demonstrated that the strain rate effect during SHTB tests quits evolving at the necking onset, so the large increase of  $\dot{\epsilon}_{True}$  typically occurring in the post-necking phase does not affect at all the stresses which, then, only depend on the strain and on the temperature.

Furthermore, Figure 3.31 also shows that the steeper is the  $R$  function implemented beyond the necking onset, the greater is the underestimation of the effective strain rate delivered by FEM: in fact, the steepest dynamic amplification considered,  $R_{True-Slow}$ , delivers the greater underestimation error of the lot.

The function  $JC-0.019$  at late stages tends to improve its accuracy, because  $\dot{\epsilon}_{True}$  is largely increased and the Johnson-Cook dynamic amplification is almost fully saturated: this further supports the finding that the plateau-like horizontal trend for the dynamic amplification beyond the necking onset is the only one really compatible with the experimentally measured  $\dot{\epsilon}_{True}$ . A  $c$  coefficient much smaller than  $0.019$  could make the saturation of the  $JC$  model closer to the necking onset, but it would also bring much smaller amplification levels than the 15% observed by experiments and correctly modeled by the initial steep ramp of the piecewise linear  $R$  functions.

Figure 3.31 also evidences that  $\dot{\epsilon}_{True}$  is highly sensitive to the dynamic amplification also in the postnecking range, while Figure 3.30 shown that  $\sigma_{True}$  nearly turns off its dependence on the dynamic amplification as the necking takes place: then  $\dot{\epsilon}_{True}$  is the only right variable for validating FEM simulations of SHTB experiments, via numerical/experimental comparison.

It is essential to recall that the possibility of taking  $\dot{\epsilon}_{True}$  as an output variable from the FEM, useful for validation purposes, only derives from the strategy of modeling the input and output bars together with the specimen, and of loading the system by applying the incident wave as a boundary condition. In fact, in this way, the strain rate from FEM is the result of the wave reflections and transmissions depending on the interplay of the impedances and, for the specimen, the impedance is largely variable depending on the significant shape changes and material hardening typically occurring during a SHTB test.

Then, the achievement of the right  $\dot{\epsilon}_{True}$  from a FEM run including the elastic bars ensures that an adequate modeling of the evolving specimen impedance is ensured which, in turn, means that also the evolutions of the specimen shape and of its material hardening are correctly reproduced.

On the contrary, if only the specimen is modeled by FEM without input and output bars, then the displacements of both specimen ends obtained from the experiments must be assigned as boundary conditions instead of the incident wave on the input bar. Then,  $\dot{\epsilon}_{True}$  is not an output variable anymore and it becomes a fixed input, independent of whatever material behavior is implemented.

Now that the model of the dynamic response of the FEN steel is validated, together with the necking-induced freezing of the strain rate effect, the evolution of the ratio  $\sigma_{Eq-A} / \sigma_{True}$  can be calculated from FEM, for assessing whether or not it complies with the material-independent  $MLR$  polynomial which was proposed in Mirone (2004a) for the static necking.

Figure 3.32 shows that the above ratio, derived from the validated FEM results of both the “fast” and the “slow” tests simulated with the  $R_{True-Flat}$  function, nicely follows the  $MLR$  polynomial all over the strain range of interest, with an error within 4%.

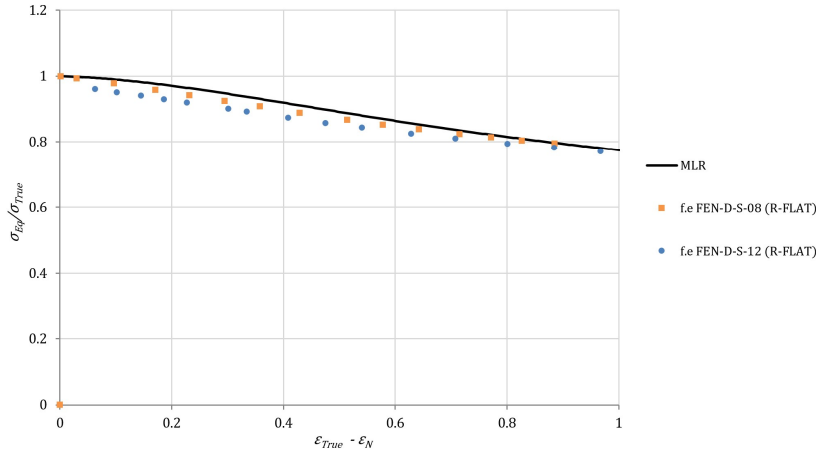


Figure 3.32 Evolving flow stress/true stress ratio during SHTB tests

The outcome in Figure 3.32 demonstrates that the  $MLR$  post necking correction can also be used for deriving the flow curves of dynamic tests, by simply correcting the true curves from SHTB experiments, according to eq. (55).

### 3.3.3 Testability Limits Due to the Freezing Effect

Generally, the reflected wave  $\varepsilon_R$  traveling along the input bar in SHTB tests can be assumed as trapezoidal and homothetic to the incident wave, with similar rise times  $t_R$ . Then, within the time  $t_R$ , both  $\varepsilon_R$  and the engineering strain rate  $\dot{\varepsilon}_{Eng}$ , connected each other by eq. (38), are linear functions of time; as a consequence, the engineering strain is quadratic, according to eq. (56):

$$\dot{\varepsilon}_{Eng}(t) = \alpha \cdot t; \quad \varepsilon_{Eng}(t) = \alpha \cdot \frac{t^2}{2} \quad (56)$$

where  $\alpha$  includes, as known, the sound speed in the bars, the reflection coefficient based on the current mechanical impedances at the specimen-bar interfaces, the length of the specimen and the slope of the incident wave within its rise time.

For ensuring that the stress-strain curve of the SHTB test at hand is amplified according to the desired target strain rate, it is essential that the plateau of the reflected wave is reached before the necking onset so that  $\varepsilon_{Eng}(t_R) \leq \varepsilon_N$ .

The condition that the necking just initiates at the end of the rise time / at the beginning of the plateau, allows to relate the minimum value of the slope necessary for meeting such condition, to the engineering strain at necking onset,  $\varepsilon_{Eng-N}$ :

$$\varepsilon_{Eng}(t_R) = \varepsilon_{Eng-N} = \alpha \cdot \frac{t_R^2}{2} \Rightarrow \alpha = 2 \cdot \frac{\varepsilon_{Eng-N}}{t_R^2} \quad (57)$$

A limit value of the target strain rate,  $\dot{\varepsilon}_{Eng-L}$ , can be then found by combining eqs. (56) and (57), which expresses the maximum strain rate up to which the dynamic amplification can really affect the experimental stress-strain curves, when dynamics tests of a material with its given  $\varepsilon_N$ , just slightly variable with the strain rate, are ran with SHTB equipment having a given rise time  $t_R$ :

$$\dot{\varepsilon}_{Eng-L} = \dot{\varepsilon}_{Eng}(t_R) = \alpha \cdot t_R = 2 \cdot \frac{\varepsilon_{Eng-N}}{t_R} \quad (58)$$

Before the necking onset,  $\dot{\varepsilon}_{True}$  is related to  $\dot{\varepsilon}_{Eng}$  so that their values start evolving very close to each other at the beginning of a SHTB test and then slightly start departing each other according to eq. (59).

$$\dot{\varepsilon}_{True} = \frac{\partial}{\partial t} \varepsilon_{True} = \frac{\partial}{\partial t} [\ln(1 + \varepsilon_{Eng})] = \frac{1}{1 + \varepsilon_{Eng}} \cdot \frac{\partial}{\partial t} [\varepsilon_{Eng}] = \frac{\dot{\varepsilon}_{Eng}}{1 + \varepsilon_{Eng}} \quad (59)$$

Therefore, the underlying hypothesis that the necking is not yet initiated allows to convert the engineering data into true data:

$$\dot{\varepsilon}_{True-} = \frac{\dot{\varepsilon}_{Eng-L}}{1 + \varepsilon_{Eng-N}} = 2 \cdot \frac{\varepsilon_{Eng-N}}{t_R \cdot (1 + \varepsilon_{Eng})} \quad (60)$$

If, on the same SHTB with the same material, the plateau of the incident wave is tailored for delivering a target strain rate greater than the above limit,  $\dot{\varepsilon}_{True} > \dot{\varepsilon}_{True-}$ , then the strain rate effect freezes before such target strain rate is reached and, in turn, the resulting stress-strain curve will not reflect a dynamic amplification really corresponding to the target strain rate effectively achieved during the test.

This is the case of the FEN steel discussed in the previous section, where the dynamic amplification of true curves from the slower test nearly corresponded to the target strain rate close to 700, while that from the faster test was frozen by the necking onset, much sooner the target strain rate was reached.

Then, for a given SHTB equipment with a fixed rise time, each material with its own necking strain can be dynamically tested only up to the limit strain rate of eq.

(60); greater strain rates can be easily imposed to the specimen, but they cannot affect in any way the resulting stress-strain curves.

The curves expressing such limit strain rates are plotted in Figure 3.33 for rise times extending up to 200  $\mu\text{s}$  and for five values of the necking strain, between 0.025 and 0.2. For a rise time of 100  $\mu\text{s}$ , the “testability envelopes” of materials with  $\epsilon_N = 0.025$  and  $\epsilon_N = 0.200$  are identified by the colour-filled rectangle including the vertexes marked by the round and the triangular symbols, respectively.

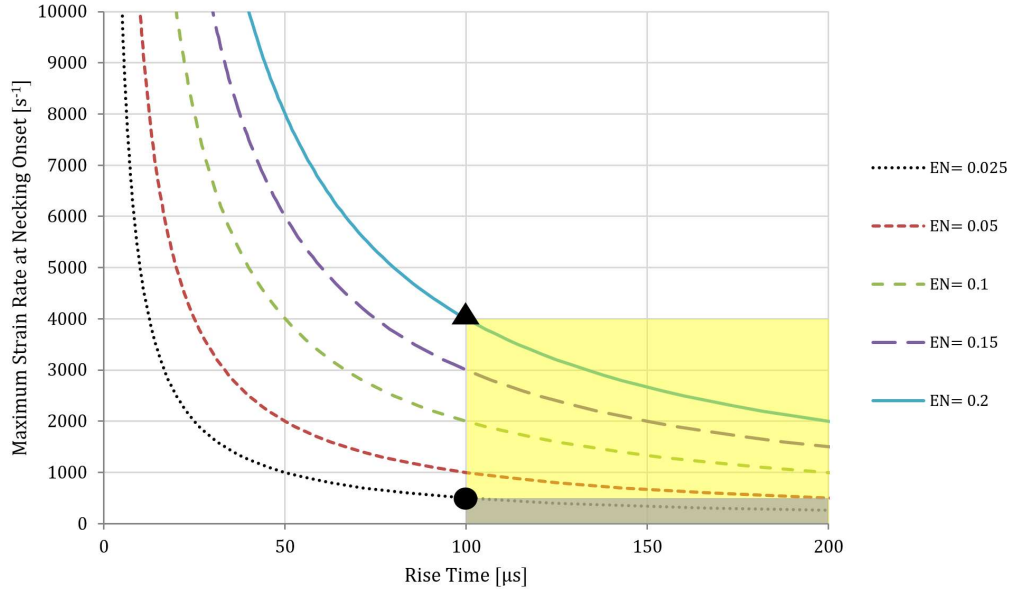


Figure 3.33 Limit strain rate as function of  $t_R$  and  $\epsilon_N$

Indeed, the early-necking FEN steel tested with  $t_R \approx 100 \mu\text{s}$  delivered dynamics true curves only amplified up to a strain rate just below  $700 \text{ s}^{-1}$  (the nominal value  $\dot{\epsilon}_{Eng} = 700 \text{ s}^{-1}$  was reached just after the necking onset, at a strain of about 0.04): this fully agrees with the round mark in Figure 3.33 indicating a limit strain rate of about  $500 \text{ s}^{-1}$ . Whatever strain rate greater than  $500 \text{ s}^{-1}$  can only be reached after the necking took place and, then, it can only generate the same stress-strain curves amplified up to the limit strain rate.

If a late-necking material was tested with the  $t_R \approx 100 \mu\text{s}$  currently available at the University of Catania, then up to  $4000 \text{ s}^{-1}$  could be reached before the necking onset and, then, the experimental stress-strain curves would be amplified up to such limit strain rate, also if much higher values of  $\dot{\epsilon}_{True}$  were reached beyond the necking onset.

Then, if we assume that direct-tension SHTB systems based on the release of a stored preload can exhibit rise times not smaller than  $30 \mu\text{s}$ , it follows that the dynamic stress amplification of late-necking materials can be derived up to about  $10000 \text{ s}^{-1}$  but, for very early-necking materials, such testability limit can be reduced of one order of magnitude, to about  $1000 \text{ s}^{-1}$ .



The freezing of the strain rate effect, induced by the necking, poses then remarkable limitations to the possibility of determining the dynamic properties of materials via SHTB experiments.

### 3.4 Dynamic Characterization and Modelling Summary

In this Chapter, the side effects of the dynamic stress-strain characterization made through the standard strain-gauge-based Hopkinson bar technique (“engineering” approach) were discussed, compared to the fast camera-assisted technique where the evolving specimen diameter of round specimens is optically measured during each test (“true” approach). Similar considerations were already available in the literature, but here an attempt is made to comprehensively assessing and quantifying all the detrimental aspects of the “engineering” approach compared to the “true” one, with reference to different metal alloys and different specimen geometries. The large underestimations of stresses and strains already known to affect the static testing are confirmed to occur also at high strain rates. The errors introduced by the engineering approach, evaluated for various combinations of geometry and elongation rates, are confirmed to be significant and to largely depend on the specimen shape parameter  $L/d$ . The engineering approach is also found to hugely underestimate the strain rate, to the extent that  $\dot{\epsilon}_{Eng}$  at failure is found to be ten times smaller than the  $\dot{\epsilon}_{True}$  really affecting the material at the local scale; also, the faster of two different true strain rate histories can appear to be the slower one if the engineering approach is adopted. Having ascertained such issues, the interaction between the strain rate effect and the necking occurring in SHTB experiments was investigated. Firstly, an experimental campaign on a sintered Electron Beam Ti6Al4V was shown with a proposed material model reflecting such phenomenon. Then, dynamic experiments were performed on round tensile specimens made of a FE370 mild steel, by speed camera-enhanced SHTB tests with different preloads and different specimen lengths, aimed at imposing different strain rate histories. At the necking onset, the real strain rate  $\dot{\epsilon}_{True}$  was confirmed to progressively diverge from the engineering one  $\dot{\epsilon}_{Eng}$ , so that, at failure, the effective strain rate was almost 10 times greater than the nominal one. Due to the very early necking of the FE370 steel, the strain rate histories of all the SHTB tests were not yet fully differentiated each other at the necking onset, while they started remarkably spreading at later deformation stages. At the same time, the dynamic true curves delivered by all tests were almost identical from the first yield up to failure, with no regard for the strain rate histories, which, instead, largely differed each other beyond the necking onset. Then the strain rate effect, expressed by the ratio of dynamics to static true curves, resulted to be a material property common to all tests only up to the necking onset, after which every test delivered its own curve of dynamic amplification. This suggested that, beyond the necking inception,

the effect of the strain rate on the experimental true curves was not visible anymore and impossible to be determined. Then, four tentative functions have been implemented by FEM for modelling the dynamic amplification of the FEN steel. The numerical / experimental comparisons demonstrated that modelling the freezing of the dynamic amplification at the necking onset is essential for obtaining reasonable FEM predictions of  $\dot{\epsilon}_{True}$ , while the prediction of  $\sigma_{True}$  are nearly insensitive to the dynamic amplification in the postnecking range, as also found by experiments. Indeed, whatever increase of the dynamic amplification modelled beyond the necking onset led to remarkable underestimations of the strain rate by FEM, while the corresponding true stress-true strain curves remained almost unaffected. This also demonstrated that the full SHTB system, including input and output bars, must be modelled by FEM for correctly simulating the specimen impedance, highly variable during a test, and for getting  $\dot{\epsilon}_{True}$  as the only FEM output variable suitable for validation purposes in the post necking range. The freezing of the dynamic amplification due to the necking inception also poses significant limitations to the maximum strain rates up to which the strain rate effect can be determined by SHTB experiments. In fact, the achievement of the desired strain rate before the necking onset is mandatory for ensuring that the experimental true curves incorporate a dynamic amplification really corresponding to such target strain rate. For early-necking materials, meeting the above condition requires very short rise times which can either introduce dispersion-related side effects or, in the worst cases, be beyond feasibility. Although it has been observed by experiments and confirmed by validated FEM analyses, it is not yet fully explained, on a physical basis, why such phenomena takes place, and it is possible that other implications arise from such behaviour together with the limitation to the dynamics testability of early-necking materials.



## 4 Conclusions

In this research, material characterization and modelling have been investigated regarding quasistatic and dynamic tests on metals. Considering the static behaviour of such materials, a new yield criteria has been proposed, based on the experimental evidence that many structural metals exhibit different hardening functions when the plastic deformation occurs under differently evolving Lode angles. Such yield function, initially based on a blend of the von Mises surface to a Tresca-like one, is  $X$  and, eventually,  $TF$  dependent. Experimental data by Allahverdizadeh et al. (2015) on Ti6Al4V were used for calibrating the model and for successfully validating it with various plastic straining histories, occurring under different stress paths and Lode angle ranges. The model proved to reduce the substantial error which the classical Mises plasticity introduces when the simulated tests involve variable Lode angles departing from uniaxiality. Although the elastoplastic response of the Ti6Al4V alloy was accurately modeled by the proposed yield function, other materials and further experiments, generating constant Lode angles and scanning the 0-30 degrees range in finer intervals, might be useful for checking the model generality and further develop it. Moreover, in this research, a new simple characterization procedure for metals is proposed. Based on the pure geometric and material-independent nature of the necking phenomenon, it is able to convert the engineering curves, coming from tensile tests, into the true curves for several specimens with cylindrical, square and rectangular cross sections with different width-to-thickness ratios considering the post-necking true strain as the governing variable. To obtain such procedure, several FEM simulations of the tensile tests were run with a set of nine arbitrary materials, encompassing very different combinations of early/medium/late necking strain and low/medium/high hardening slopes. The materials flow curves were obtained by arbitrary Ludwik functions in the pre-necking phase and by an MLR-corrected line tangent to such first part in the post-necking phase. Analysing the FEM results, it was possible to define material-independent functions of the post-necking strains, called MVB, able to convert the engineering curves into the true curves, for each considered specimen cross section and for virtually whatever material. The new procedure, validated for round, thick flat and thin flat specimens, is of significant interest for research and industrial applications since it has the benefits of the simple experimental procedures typical of the engineering approach while maintaining at the same time the accuracy degree typical of the true approach. Further experiments with different geometries and materials would be useful to generalize the procedure. Regarding the dynamic behaviour of metals, in this research all the detrimental aspects of the “standard strain-gauge-based engineering” approach compared to the “fast camera-

assisted true” one in the Hopkinson bar tensile tests are comprehensively assessed and quantified, with reference to different metal alloys and different specimen geometries. The errors introduced by the engineering approach, evaluated for various combinations of geometry and elongation rates, were confirmed to be significant and to largely depend on the specimen slenderness. The large underestimations of stresses and strains, already known to affect the static testing, were confirmed to also occur at high strain rates and, moreover, the engineering underestimation of the strain rate was found to be very misleading in the strain rate characterization ( $\dot{\epsilon}_{Eng}$  at failure is found to be to ten times smaller than the  $\dot{\epsilon}_{True}$  at the local scale and the faster of two strain rate histories can appear the slower one). Lastly, in this research, the necking-induced freezing of the strain rate effect was analysed, with reference to materials exhibiting both early and late necking initiation; the consequences of this phenomenon in the characterization process via Hopkinson bar tensile tests were also discussed. This feature, supported here by both experiments and finite elements analyses, is also compatible with experimental results from the literature and can provide an explanation to the saturating nature of many literature models, which might be just apparent. In fact, if this saturation of the strain rate effect at strain rates typical of SHTB testing was really occurring, there would be no reason for testing the material behaviour at higher strain rates via Taylor tests or Flyer plate tests. Further experiments combining specimens made of the same low necking strain material with high/low SHTB rise times and specimens made of the same high necking strain material with high/low SHTB rise times would be useful for further investigating such phenomenon.

# References

- Allahverdizadeh, N., (2014). Investigation of geometry transferability of Lemaitre's continuum damage mechanics model (Doctoral dissertation, Italy).
- Allahverdizadeh, N., Manes, A., Giglio, M., & Gilioli, A. (2014). Geometry Transferability of Lemaitre's Continuum Damage Mechanics Model in the Plane Stress Specimens. In *Key Engineering Materials* (Vol. 592, pp. 266-270). Trans Tech Publications.
- Allahverdizadeh, N., Gilioli, A., Manes, A., & Giglio, M. (2015). An experimental and numerical study for the damage characterization of a Ti-6AL-4V titanium alloy. *International Journal of Mechanical Sciences*, 93, 32-47.
- Anderson, D., Winkler, S., Bardelcik, A., & Worswick, M. J. (2014). Influence of stress triaxiality and strain rate on the failure behavior of a dual-phase DP780 steel. *Materials & Design*, 60, 198-207.
- Bai, Y., & Wierzbicki, T. (2008). A new model of metal plasticity and fracture with pressure and Lode dependence. *International journal of plasticity*, 24(6), 1071-1096.
- Bai, Y., & Wierzbicki, T. (2010). Application of extended Mohr-Coulomb criterion to ductile fracture. *International Journal of Fracture*, 161(1), 1-20.
- Bao, Y., & Wierzbicki, T. (2004). On fracture locus in the equivalent strain and stress triaxiality space. *International Journal of Mechanical Sciences*, 46(1), 81-98.
- Barsoum, I., & Faleskog, J. (2007). Rupture mechanisms in combined tension and shear—Experiments. *International Journal of Solids and Structures*, 44(6), 1768-1786.
- Barsoum, I., Faleskog, J., & Pingle, S. (2012). The effect of stress state on ductility in the moderate stress triaxiality regime of medium and high strength steels. *International Journal of Mechanical Sciences*, 65(1), 203-212.
- Besnard, G., Hild, F., Lagrange, J. M., Martinuzzi, P., & Roux, S. (2012). Analysis of necking in high speed experiments by stereocorrelation. *International journal of impact engineering*, 49, 179-191.
- Bigoni, D., & Piccolroaz, A. (2004). Yield criteria for quasibrittle and frictional materials. *International journal of solids and structures*, 41(11), 2855-2878.
- Bridgman, P. W. (1952). *Studies in large plastic flow and fracture* (Vol. 177). New York: McGraw-Hill.
- Brünig, M., Chyra, O., Albrecht, D., Driemeier, L., & Alves, M. (2008). A ductile damage criterion at various stress triaxialities. *International Journal of Plasticity*, 24(10), 1731-1755.
- Cabezas, E. E., & Celentano, D. J. (2004). Experimental and numerical analysis of the tensile test using sheet specimens. *Finite Elements in Analysis and Design*, 40(5), 555-575.
- Cadoni, E., Dotta, M., Forni, D., & Bianchi, S. (2011). Strain-rate effect on the tensile behaviour of high strength alloys. In *Applied Mechanics and Materials* (Vol. 82, pp. 124-129). Trans Tech Publications.
- Celentano, D. J., Cabezas, E. E., & Garcia, C. M. (2005). Analysis of the Bridgman procedure to characterize the mechanical behavior of materials in the tensile test: experiments and simulation. *Transactions of the ASME-E-Journal of Applied Mechanics*, 72(1), 149.
- Celentano, D. J., Cabezas, E. E., García, C. M., & Monsalve, A. E. (2004). Characterization of the mechanical behaviour of materials in the tensile test: experiments and simulation. *Modelling and Simulation in Materials Science and Engineering*, 12(4), S425.
- Chaboche, J. L. (1988). Continuum Damage Mechanics: Part I—General Concepts. *Journal of Applied Mechanics*, 55, 59.
- Chaboche, J. L. (1988). Continuum Damage Mechanics: Part II—Damage growth, crack initiation, and crack growth. *Journal of applied mechanics*, 55(1), 65-72.
- Cortese, L., Coppola, T., Campanelli, F., Campana, F., & Sasso, M. (2014). Prediction of ductile failure in materials for onshore and offshore pipeline applications. *International Journal of Damage Mechanics*, 23(1), 104-123.
- Cortese, L., Coppola, T., Campanelli, F., & Broggiato, G. B. (2016). A J2-J3 approach in plastic and damage description of ductile materials. *International Journal of Damage Mechanics*, 25(2), 228-250.
- Cowper, G. R., & Symonds, P. S. (1957). Strain-hardening and strain-rate effects in the impact loading of cantilever beams (No. TR-C11-28). Brown Univ Providence Ri.
- De Almeida, O., Lagattu, F., & Brillaud, J. (2008). Analysis by a 3D DIC technique of volumetric deformation gradients: Application to polypropylene/EPR/talc composites. *Composites Part A: Applied Science and Manufacturing*, 39(8), 1210-1217.
- Dorogoy, A., Rittel, D., & Godinger, A. (2016). A shear-tension specimen for large strain testing. *Experimental Mechanics*, 56(3), 437-449.

- Erice, B., & Gálvez, F. (2014). A coupled elastoplastic-damage constitutive model with Lode angle dependent failure criterion. *International Journal of Solids and Structures*, 51(1), 93-110.
- Erice, B., Gálvez, F., Cendón, D., & Sánchez-Gálvez, V. (2010). Mechanical behavior of fv535 steel against ballistic impact at high temperatures. In *Proceedings of 25th International Symposium on Ballistics*, Beijing, China (pp. 1087-1096).
- Erice, B., Gálvez, F., Cendón, D. A., & Sánchez-Gálvez, V. (2012). Flow and fracture behaviour of FV535 steel at different triaxialities, strain rates and temperatures. *Engineering Fracture Mechanics*, 79, 1-17.
- Faleskog, J., & Barsoum, I. (2013). Tension–torsion fracture experiments—Part I: Experiments and a procedure to evaluate the equivalent plastic strain. *International Journal of Solids and Structures*, 50(25), 4241-4257.
- Gao, X., Zhang, T., Hayden, M., & Roe, C. (2009). Effects of the stress state on plasticity and ductile failure of an aluminum 5083 alloy. *International Journal of Plasticity*, 25(12), 2366-2382.
- Gao, X., Zhang, T., Zhou, J., Graham, S. M., Hayden, M., & Roe, C. (2011). On stress-state dependent plasticity modeling: significance of the hydrostatic stress, the third invariant of stress deviator and the non-associated flow rule. *International Journal of Plasticity*, 27(2), 217-231.
- García-Garino, C., Gabaldón, F., & Goicolea, J. M. (2006). Finite element simulation of the simple tension test in metals. *Finite Elements in Analysis and Design*, 42(13), 1187-1197.
- Ghajar, R., Mirone, G., & Keshavarz, A. (2013). Sensitivity Analysis on triaxiality factor and Lode angle in ductile fracture. *Journal of Mechanics*, 29(1), 177-184.
- Graham, S. M., Zhang, T., Gao, X., & Hayden, M. (2012). Development of a combined tension–torsion experiment for calibration of ductile fracture models under conditions of low triaxiality. *International Journal of Mechanical Sciences*, 54(1), 172-181.
- Grytten, F., Daiyan, H., Polanco-Loria, M., & Dumoulin, S. (2009). Use of digital image correlation to measure large-strain tensile properties of ductile thermoplastics. *Polymer Testing*, 28(6), 653-660.
- Guan, Z. (2014). Quantitative analysis on the onset of necking in rate-dependent tension. *Materials & Design*, 56, 209-218.
- Gurson, A. L. (1977). Continuum theory of ductile rupture by void nucleation and growth: Part I—Yield criteria and flow rules for porous ductile media. *Journal of engineering materials and technology*, 99(1), 2-15.
- Johnson, G. R., & Cook, W. H. (1983). A constitutive model and data for metals subjected to large strains, high strain rates and high temperatures. In *Proceedings of the 7th International Symposium on Ballistics* (Vol. 21, No. 1, pp. 541-547).
- Joun, M., Eom, J. G., & Lee, M. C. (2008). A new method for acquiring true stress–strain curves over a large range of strains using a tensile test and finite element method. *Mechanics of Materials*, 40(7), 586-593.
- Kim, J. H., Serpantié, A., Barlat, F., Pierron, F., & Lee, M. G. (2013). Characterization of the post-necking strain hardening behavior using the virtual fields method. *International Journal of Solids and Structures*, 50(24), 3829-3842.
- La Rosa, G., Risitano, A., & Mirone, G. (2003). Postnecking elastoplastic characterization: Degree of approximation in the Bridgman method and properties of the flow-stress/true-stress ratio. *Metallurgical and Materials Transactions A*, 3(34), 615-624.
- Le Roy, G., Embury, J. D., Edwards, G., & Ashby, M. F. (1981). A model of ductile fracture based on the nucleation and growth of voids. *Acta Metallurgica*, 29(8), 1509-1522.
- Lehmann, T. (1985). On a generalized constitutive law in thermo-plasticity taking into account different yield mechanisms. *Acta mechanica*, 57(1-2), 1-23.
- Lemaitre, J. (1985). A continuous damage mechanics model for ductile fracture. *Transactions of the ASME. Journal of Engineering Materials and Technology*, 107(1), 83-89.
- Ling, Y. (1996). Uniaxial true stress-strain after necking. *AMP Journal of Technology*, 5, 37-48.
- Mackenzie, A. C., Hancock, J. W., & Brown, D. K. (1977). On the influence of state of stress on ductile failure initiation in high strength steels. *Engineering fracture mechanics*, 9(1), 167IN13169-168IN14188.
- Mae, H., Teng, X., Bai, Y., & Wierzbicki, T. (2007). Calibration of ductile fracture properties of a cast aluminum alloy. *Materials Science and Engineering: A*, 459(1), 156-166.
- Mashayekhi, M., & Ziaei-Rad, S. (2006). Identification and validation of a ductile damage model for A533 steel. *Journal of materials processing technology*, 177(1), 291-295.
- McClintock, F. A. (1968, June). A criterion for ductile fracture by the growth of holes. *ASME*.
- Mirone, G. (2004a). A new model for the elastoplastic characterization and the stress–strain determination on the necking section of a tensile specimen. *International Journal of Solids and Structures*, 41(13), 3545-3564.
- Mirone, G. (2004b). Approximate model of the necking behaviour and application to the void growth prediction. *International Journal of Damage Mechanics*, 13(3), 241-261.
- Mirone, G. (2013). The dynamic effect of necking in Hopkinson bar tension tests. *Mechanics of materials*, 58, 84-96.
- Mirone, G. (2014). Effetto Dei Parametri Di Triassialità e Deviatoricità sulla Risposta Dei Materiali Duttili. *AIAS 2014*
- Mirone, G., & Corallo, D. (2010a). A local viewpoint for evaluating the influence of stress triaxiality and Lode angle on ductile failure and hardening. *International Journal of Plasticity*, 26(3), 348-371.

- Mirone G., & Corallo D. (2010b). Analisi del necking di lamiere sottili. XXXIX Convegno nazionale Associazione Italiana per l'Analisi delle Sollecitazioni (AIAS)
- Mirone, G., Corallo, D., & Barbagallo, R. (2016a). Interaction of strain rate and necking on the stress-strain response of uniaxial tension tests by Hopkinson bar. *Procedia Structural Integrity*, 2, 974-985.
- Mirone, G., Barbagallo, R., Corallo, D., & Di Bella, S. (2016b). Static and dynamic response of titanium alloy produced by electron beam melting. *Procedia Structural Integrity*, 2, 2355-2366.
- Mirone, G., Barbagallo, R., & Corallo, D. (2016c). A new yield criteria including the effect of lode angle and stress triaxiality. *Procedia Structural Integrity*, 2, 3684-3696.
- Mirone, G., Corallo, D., & Barbagallo, R. (2017). Experimental issues in tensile Hopkinson bar testing and a model of dynamic hardening. *International Journal of Impact Engineering*, 103, 180-194.
- Nadai, A. (1963). *Theory of flow and fracture solids - Volume 2*. McGraw Hill, New York
- Nilsson, K. (2004). Effects of elastic unloading on multiple necking in tensile bars. *International journal of impact engineering*, 30(10), 1353-1367.
- Noble, J. P., Goldthorpe, B. D., Church, P., & Harding, J. (1999). The use of the Hopkinson bar to validate constitutive relations at high rates of strain. *Journal of the Mechanics and Physics of Solids*, 47(5), 1187-1206.
- Osovski, S., Rittel, D., Rodríguez-Martínez, J. A., & Zaera, R. (2013). Dynamic tensile necking: influence of specimen geometry and boundary conditions. *Mechanics of Materials*, 62, 1-13.
- Papasidero, J., Doquet, V., & Mohr, D. (2014). Determination of the effect of stress state on the onset of ductile fracture through tension-torsion experiments. *Experimental Mechanics*, 54(2), 137-151.
- Paul, B. (1968). Generalized pyramidal fracture and yield criteria. *International Journal of Solids and Structures*, 4(2), 175-196.
- Peirs, J., Verleysen, P., Van Paepegem, W., & Degrieck, J. (2011). Determining the stress-strain behaviour at large strains from high strain rate tensile and shear experiments. *International Journal of Impact Engineering*, 38(5), 406-415.
- Penasa, M., Piccolroaz, A., Argani, L., & Bigoni, D. (2014). Integration algorithms of elastoplasticity for ceramic powder compaction. *Journal of the European Ceramic Society*, 34(11), 2775-2788.
- Peroni, L., Scapin, M., & Fichera, C. (2015). An advanced identification procedure for material model parameters based on image analysis. 10th European LS-DYNA Conference 2015, Würzburg, Germany (2015)
- Piccolroaz, A., & Bigoni, D. (2009). Yield criteria for quasibrittle and frictional materials: a generalization to surfaces with corners. *International Journal of Solids and Structures*, 46(20), 3587-3596.
- Rice, J. R., & Tracey, D. M. (1969). On the ductile enlargement of voids in triaxial stress fields\*. *Journal of the Mechanics and Physics of Solids*, 17(3), 201-217.
- Rizza, F. (2015). *Analisi numerica di una protesi di bacino custom made*. Master Degree Thesis, Università di Catania
- Rodríguez-Martínez, J. A., Rittel, D., Zaera, R., & Osovski, S. (2013). Finite element analysis of AISI 304 steel sheets subjected to dynamic tension: the effects of martensitic transformation and plastic strain development on flow localization. *International journal of impact engineering*, 54, 206-216.
- Rodríguez-Millán, M., Vaz-Romero, Á., & Arias, Á. (2015). Failure behavior of 2024-T3 aluminum under tension-torsion conditions. *Journal of Mechanical Science and Technology*, 29(11), 4657-4663.
- Rotbaum, Y., Osovski, S., & Rittel, D. (2015). Why does necking ignore notches in dynamic tension?. *Journal of the Mechanics and Physics of Solids*, 78, 173-185.
- Rotbaum, Y., & Rittel, D. (2014). Is there an optimal gauge length for dynamic tensile specimens?. *Experimental Mechanics*, 54(7), 1205-1214.
- Roth, C. C., & Mohr, D. (2014). Effect of strain rate on ductile fracture initiation in advanced high strength steel sheets: experiments and modeling. *International Journal of Plasticity*, 56, 19-44.
- Ruggiero, A. (2005). *Dinamica dell'impatto: interpretazione, modellazione e simulazione numerica del comportamento meccanico dei metalli*, Tesi di Dottorato in Ingegneria Civile e Meccanica, Università degli Studi di Cassino.
- Rusinek, A., Zaera, R., Klepaczko, J. R., & Cheriguene, R. (2005). Analysis of inertia and scale effects on dynamic neck formation during tension of sheet steel. *Acta Materialia*, 53(20), 5387-5400.
- Sato, K., Yu, Q., Hiramoto, J., Urabe, T., & Yoshitake, A. (2015). A method to investigate strain rate effects on necking and fracture behaviors of advanced high-strength steels using digital imaging strain analysis. *International Journal of Impact Engineering*, 75, 11-26.
- Tarigopula, V., Hopperstad, O. S., Langseth, M., Clausen, A. H., & Hild, F. (2008). A study of localisation in dual-phase high-strength steels under dynamic loading using digital image correlation and FE analysis. *International Journal of Solids and Structures*, 45(2), 601-619.
- Tvergaard, V., & Needleman, A. (1984). Analysis of the cup-cone fracture in a round tensile bar. *Acta metallurgica*, 32(1), 157-169.
- Vaz-Romero, A., Rotbaum, Y., Rodríguez-Martínez, J. A., & Rittel, D. (2016). Necking evolution in dynamically stretched bars: New experimental and computational insights. *Journal of the Mechanics and Physics of Solids*, 91, 216-239.



- Verleysen, P., & Degrieck, J. (2004). Experimental investigation of the deformation of Hopkinson bar specimens. *International journal of impact engineering*, 30(3), 239-253.
- Verleysen, P., Oelbrandt, W., Naghdy, S., & Kestens, L. (2015). Static and dynamic tensile behaviour of aluminium processed by high pressure torsion. In *EPJ Web of Conferences* (Vol. 94, p. 02012). EDP Sciences.
- Verleysen, P., Verheghe, B., Verstraete, T., & Degrieck, J. (2009). Numerical study of the influence of the specimen geometry on split Hopkinson bar tensile test results. *Latin American Journal of Solids and Structures*, 6(3), 285-298.
- Wierzbicki, T., Bao, Y., Lee, Y. W., & Bai, Y. (2005). Calibration and evaluation of seven fracture models. *International Journal of Mechanical Sciences*, 47(4), 719-743.
- Xue, L. (2009). Stress based fracture envelope for damage plastic solids. *Engineering Fracture Mechanics*, 76(3), 419-438.
- Xue, L., & Wierzbicki, T. (2009). Ductile fracture characterization of aluminum alloy 2024-T351 using damage plasticity theory. *International Journal of Applied Mechanics*, 1(02), 267-304.
- Xue, Z., Faleskog, J., & Hutchinson, J. W. (2013). Tension–torsion fracture experiments–Part II: Simulations with the extended Gurson model and a ductile fracture criterion based on plastic strain. *International Journal of Solids and Structures*, 50(25), 4258-4269.
- Xue, Z., Pontin, M. G., Zok, F. W., & Hutchinson, J. W. (2010). Calibration procedures for a computational model of ductile fracture. *Engineering Fracture Mechanics*, 77(3), 492-509.
- Xue, Z., Vaziri, A., & Hutchinson, J. W. (2008). Material aspects of dynamic neck retardation. *Journal of the Mechanics and Physics of Solids*, 56(1), 93-113.
- Yan, S. L., Yang, H., Li, H. W., & Ren, G. Y. (2014). Experimental study of macro–micro dynamic behaviors of 5A0X aluminum alloys in high velocity deformation. *Materials Science and Engineering: A*, 598, 197-206.
- Yang, L. M., & Shim, V. P. W. (2005). An analysis of stress uniformity in split Hopkinson bar test specimens. *International Journal of Impact Engineering*, 31(2), 129-150.
- Zaera, R., Rodríguez-Martínez, J. A., Vadillo, G., & Fernández-Sáez, J. (2014). Dynamic necking in materials with strain induced martensitic transformation. *Journal of the Mechanics and Physics of Solids*, 64, 316-337.
- Zerilli, F. J., & Armstrong, R. W. (1987). Dislocation-mechanics-based constitutive relations for material dynamics calculations. *Journal of Applied Physics*, 61(5), 1816-1825.
- Zhang, Z. L., Hauge, M., Ødegård, J., & Thaulow, C. (1999). Determining material true stress–strain curve from tensile specimens with rectangular cross-section. *International Journal of Solids and Structures*, 36(23), 3497-3516.
- Zhang, Z. L., Ødegård, J., Søvik, O. P., & Thaulow, C. (2001). A study on determining true stress–strain curve for anisotropic materials with rectangular tensile bars. *International Journal of Solids and Structures*, 38(26), 4489-4505.